KUOPION YLIOPISTON JULKAISUJA C. LUONNONTIETEET JA YMPÄRISTÖTIETEET 173
KUOPIO UNIVERSITY PUBLICATIONS C. NATURAL AND ENVIRONMENTAL SCIENCES 173

MIKA TARVAINEN

Estimation Methods for Nonstationary Biosignals

Doctoral dissertation

To be presented by permission of the Faculty of Natural and Environmental Sciences
of the University of Kuopio for public examination in Microteknia Auditorium,
Microteknia building, University of Kuopio,
on Friday 11th June 2004, at 12 noon

Department of Applied Physics
University of Kuopio

KUOPION YLIOPISTO
KUOPIO 2004

Distributor:

Kuopio University Library
P.O. Box 1627
FIN-70211 KUOPIO
FINLAND
Tel. +358 17 163 430
Fax +358 17 163 410
http://www.uku.fi/kirjasto/julkaisutoiminta/julkmyyn.html

Series Editors:

Professor Lauri Kärenlampi, Ph.D.
Department of Ecology and Environmental Science

Professor Jari Kaipio, Ph.D.
Department of Applied Physics

Author's address:

Department of Applied Physics
University of Kuopio
P.O. Box 1627
FIN-70211 KUOPIO
FINLAND
Tel. +358 17 162 369
Fax +358 17 162 373
E-mail: Mika.Tarvainen@uku.fi

Supervisor:

Research Director, Docent Pasi Karjalainen, Ph.D.
Department of Applied Physics
University of Kuopio

Reviewers:

Professor Jouko Lampinen, Dr.Tech.
Laboratory of Computational Engineering
Helsinki University of Technology
Helsinki
Finland

Senior Scientist Veikko Jousmäki, Ph.D.
Low Temperature Laboratory
Helsinki University of Technology
Helsinki
Finland

Opponent:

Research Professor Ilkka Korhonen, Ph.D.
Human Interaction Technologies
VTT Information Technology
Tampere
Finland

ISBN 951-781-311-2
ISBN 951-27-0006-9 (PDF)
ISSN 1235-0486

Kopijyvä
Kuopio 2004
Finland

Tarvainen, Mika. Estimation Methods for Nonstationary Biosignals. Kuopio University Publications C. Natural and Environmental Sciences 173. 2004. 138 p.
ISBN 951-781-311-2
ISBN 951-27-0006-9 (PDF)
ISSN 1235-0486

ABSTRACT

The notion biosignal can be used for any signal measurable from the human body. In this thesis, four different biosignals are considered. These are the galvanic skin response (GSR) which measures changes in skin resistance, the electrical activity of the brain known as the electroencephalogram (EEG), the variability of the heart beat interval (heart rate variability, HRV) which can be extracted from the electrocardiographic (ECG) recording, and the variability of the blood pressure values.

In the EEG recording, the potentials measured from the scalp represent a superposition of the volume conductor fields produced by active neural sources. GSR, on the other hand, measures changes in skin resistance induced by sweat gland secretion which is controlled by the sympathetic branch of the autonomic nervous system. Heart rate and blood pressure are also controlled by the autonomic nervous system, but with both the sympathetic and parasympathetic branches being effective.

In this thesis, three novel methods for the analysis of biosignals are proposed. The first proposed method is a principal component analysis (PCA) based method for analyzing the patterning of successive GSR measurements. As a specific application the method is applied to GSR measurements of 20 healthy control subjects and 13 psychotic patients. For most of the control subjects a clear pattern in successive GSRs was found whereas within psychotic patients the lack of time-locking of GSRs seemed characteristic. With application to clustering a significant discrimination of the subjects is achieved.

A major issue in biosignal analysis is the stationarity of the considered signal. If the signal is nonstationary, which is often the case for biosignals, it has to be catered for in the analysis methods. In the second proposed method, the properties of nonstationary EEG are analyzed by means of time-varying time series modeling. For the time-varying parameter estimation problem a Kalman filter algorithm along with a fixed-interval smoothing procedure is applied. This, so-called Kalman smoother approach, is applied to the estimation of event-related synchronization (ERS) dynamics of occipital alpha rhythm. With the proposed method detailed time-frequency dynamics can be extracted even from single ERS samples.

The third proposed method is an advanced, simple to use detrending method with an application to HRV analysis. The proposed method is suitable for removing slowly varying trend components from measured biosignal. The effect of the proposed detrending method on general time- and frequency-domain analysis of HRV is considered.

AMS (MOS) Classification: 62F15, 62H25, 62L12, 62M10, 62M15, 93E10
National Library of Medicine Classification: QT 36, WG 106, WL 150, WG 140
INSPEC Thesaurus: medical signal processing; estimation theory; time series; principal component analysis; autoregressive moving average processes; modelling; Kalman filters; parameter estimation; electric resistance; skin; electroencephalography; electrocardiography; blood pressure measurement

To Tanja

Acknowledgements

This study was carried out in the Department of Applied Physics at the University of Kuopio during the years 1999–2004. The study was supported by the National Technology Agency of Finland (TEKES) and the Graduate School "Functional Research in Medicine".

I want to express my gratitude to my supervisor Docent Pasi Karjalainen, Ph.D., for his guidance and encouragement and for giving me the opportunity to work in the Department of Applied Physics. I also want to give him recognition for being a great teacher whose lectures I have had the privilege to attend.

I want to thank the official reviewers Professor Jouko Lampinen, Dr.Tech., and Veikko Jousmäki, Ph.D., for their constructive criticism and suggestions for the thesis. I also want to thank all my teachers, especially Professor Jari Kaipio, Ph.D., Docent Jouko Tervo, Ph.D., and Docent Marko Vauhkonen, Ph.D.

I want to thank the whole staff of the Department of Applied Physics. It has been a privilege to work with you. Especially I want to thank all my co-workers in the Biomedical Signal Analysis research group. Many thanks for Stefanos Georgiadis, M.Sc., Mikko Kervinen, M.Sc., Juha-Pekka Niskanen, and Perttu Rantaaho, M.Sc., for all the scientific and non-scientific discussions.

I also want to thank Jaana Hiltunen, Phil.Lic., Anu Holm, M.Sc., and Minna Valkonen-Korhonen, MD, Ph.D., for their collaboration and the Departments of Psychiatry and Clinical Neurophysiology at Kuopio University Hospital for providing the measurements.

I want to thank my parents Taito and Helvi, my sister Sanna and her other half Samppa, and my brother Tommy and his wife Maarit and their lovely daughter Neea for their support and countless moments of joy. I also want to thank Erkki and Puuma for their support and all my friends, especially Jani, Lassi, Harri, Mika, Jarkko, and Mika for all kind off memories since elementary school.

Finally, I want to thank my dear wife Tanja for her endless love and support.

Kuopio, 18th May 2004

Mika Tarvainen

Abbreviations

AIC	Akaike's information criterion
AR	Autoregressive
ARMA	Autoregressive moving average
BEI	Baroreflex effectiveness index
BP	Blood pressure
BPV	Blood pressure variability
BRS	Baroreceptor reflex sensitivity, baroreflex sensitivity
CWT	Continuous wavelet transform
DBP	Diastolic blood pressure
DFT	Discrete Fourier transform
ECG	Electrocardiogram, electrocardiographic
EEG	Electroencephalogram, electroencephalographic
ERD	Event-related desynchronization
ERS	Event-related synchronization
FFT	Fast Fourier transform
FPE	Final prediction error
GSR	Galvanic skin response
HF	High frequency (HR or BP fluctuations within 0.15–0.4 Hz)
HR	Heart rate
HRV	Heart rate variability
ISI	Interstimulus interval
LF	Low frequency (HR or BP fluctuations within 0.04–0.15 Hz)
LMS	Least mean square
LS	Least squares
MA	Moving average
MAP	Maximum a posteriori
MBP	Mean blood pressure
MDL	Minimum description length
MS	Mean square
NN	Normal-to-normal heart beat interval
NN50	Number of successive NN (or RR) intervals that differ more than 50 ms
PC	Principal component
PCA	Principal component analysis
PCR	Principal component regression
pNN50	The percentage of successive NN (or RR) intervals that differ more than 50 ms
PSD	Power spectral density
RLS	Recursive least squares
RMSSD	Root mean square of successive RR interval differences
RR	Heart beat interval, RR interval
RSA	Respiratory sinus arrhythmia
SA	Sinoatrial
SBP	Systolic blood pressure

SDNN	Standard deviation of NN (or RR) intervals
SDSD	Standard deviation of successive RR interval differences
STFT	Short-time Fourier transform
TFR	Time-frequency representation
TINN	Triangular interpolation of NN (or RR) interval histogram
UC	Uniform cost
VLF	Very low frequency (HR or BP fluctuations within 0–0.04 Hz)
WSS	Wide sense stationary
WT	Wavelet transform
YW	Yule-Walker

Notations

$(\cdot)^T$	Transpose
$(\cdot)^*$	Complex conjugate
$\lvert\cdot\rvert$	Absolute value
$\lVert\cdot\rVert$	Euclidean norm
α_j, $\alpha^{(j)}$	Root of AR polynomial ($j = 1, 2, \ldots, p$)
β_k, $\beta^{(k)}$	Root of MA polynomial ($k = 1, 2, \ldots, q$)
γ_x	Autocovariance sequence of x
γ_{xy}	Cross-covariance sequence of x and y
ϵ	Residual, prediction error
η_x	Expected value of x
$\eta_{x\|y}$	Expected value of x given y
θ	Parameter vector
$\hat{\theta}$	Parameter estimate
$\tilde{\theta}$	Parameter estimation error
κ	Regularization parameter
λ	Forgetting factor of RLS algorithm
λ_k	Eigenvalue ($k = 1, 2, \ldots$)
μ	Step size of LMS algorithm
σ_x^2	Variance of x
τ	Time delay
$\mathfrak{a}$	Scale factor of wavelet transform
a_j, $a^{(j)}$	AR model coefficient ($j = 0, 1, \ldots, p$)
b_k, $b^{(k)}$	MA model coefficient ($k = 0, 1, \ldots, q$)
$B(\hat{\theta})$	Bayes cost
$C(\theta, \hat{\theta})$	Cost function
C_x	Covariance matrix of x
C_{xy}	Cross-covariance matrix of x and y
Coh_{xy}	Coherence of x and y
$\det C$	Determinant of matrix C

D_d	Difference matrix of order d
e	Observation error
$E\{x\}$	Expected value of x
$E\{x\|y\}$	Expected value of x given y
f	Frequency
f_s	Sampling frequency
H	Observation matrix
i	Imaginary unit
$\mathrm{Im}\{\cdot\}$	Imaginary part of a complex valued function
K	Kalman gain matrix
p	AR model order (integer)
$p(x)$	Probability density function of x
$p(x,y)$	Joint probability density of x and y
$p(x\|y)$	Conditional probability density of x given y
P_x	Power spectrum of x
P_{xy}	Cross spectrum of x and y
q	MA model order (integer)
r_x	Autocorrelation sequence of x
r_{xy}	Cross-correlation sequence of x and y
$\mathcal{R}(H)$	Range of H
R_x	Correlation matrix of x
R_{xy}	Cross-correlation matrix of x and y
$\mathrm{Re}\{\cdot\}$	Real part of a complex valued function
$\mathrm{Res}\{\cdot\}$	Residue
ΔT	Discrete sampling interval
v_k	Eigenvector ($k = 1, 2, \ldots$)
$\mathrm{var}\{x\}$	Variance of x
w	Window function
w	State noise
x	Observation
$x(t)$	Continuous time observation ($t \in \mathbb{R}$)
x_t	Discrete time observation ($t \in \mathbb{Z}$)
$X(f)$	Fourier transform of x
$X(z)$	z-transform of x

Contents

Chapter I

Introduction

The notion biosignal can be used for any signal measurable from human body. The measurable quantity can be electrical or, for example, change in pressure or volume. Probably the most familiar electrical measures are the *electrocardiogram* (ECG) which is a recording of the electrical activity of the heart and the *electroencephalogram* (EEG) which measures the electrical activity of the brain. Another not so well known biosignal that was traditionally used in lie detectors is the *galvanic skin response* (GSR) which measures the changes in skin resistance induced by changes in sweat gland secretion. These electrical biosignals, especially ECG and GSR, can be easily recorded from body surface with adequate bioamplifier. In addition to above biosignals, there are other kinds of biosignals that require a totally different recording method. One such biosignal is *blood pressure* (BP) which can be measured continuously, e.g., from the fingertip by using the volume-clamp method, originally proposed in [139, 140].

In addition to above continuous biosignals, there are biosignals the values of which are known only at some discrete times. One such event series is, for example, the series of successive heart beat intervals. The variation within these intervals has been studied widely and the term *heart rate variability* (HRV) is generally adopted. The HRV time series is extracted from the ECG recording by calculating the time differences between successive QRS complexes. Similar to HRV time series are the time series constructed from successive BP values. That is, after each heart beat systolic, diastolic, and mean BP values can be extracted. The fluctuation of these values is, in general, termed *blood pressure variability* (BPV).

In the EEG recording, the potentials measured from the scalp represent a superposition of the volume conductor fields produced by active neural sources. The main sources for the potentials are the pyramidal cells of the cortex. GSR, on the other hand, measures changes in skin resistance induced by sweat gland secretion. The secretion is controlled by the sympathetic branch of the autonomic nervous system and, thus, GSR has been used for capturing the sympathetic tone. Heart rate and blood pressure are also controlled by the autonomic nervous system, but with both the sympathetic and parasympathetic branches being effective.

In the analysis of biosignals, three different approaches can be distinguished: analysis of transient events related to some physical stimulus, analysis of spon-

taneous activity of the measured signal, and correlation analysis of two or more biosignals of different origin. In the event-related analysis, the aim is to analyze those parts of the signal that are related to the stimulus. The response to the stimulus can be assumed to be either constant or variable for repeated stimulation. In the former case, an average of the responses is usually taken, whereas in the latter case, e.g., the trend within the responses is analyzed. In the analysis of the spontaneous activity of the measured signal, on the other hand, the whole measurement is typically analyzed. The characteristics of the signal are typically parameterized by calculating different statistics. In the biosignal analysis, it is common to characterize the measurement in the frequency-domain by calculating the spectrum of the signal. The fundamental aim of biosignal analysis is typically to obtain information on the physiological or psychological state of the subject or to improve the understanding of the functioning of the subject organ. By means of correlation analysis of several biosignals it is sometimes possible to obtain such valuable information that could not be obtained directly from the separate signals.

One important issue in the analysis of biosignals is stationarity. A stationary signal is such that its statistical properties do not change over time. Stationarity is often a desired property since many of the analysis methods, especially the frequency-domain methods where the spectrum of the signal is calculated, require a stationary signal. Unfortunately, biosignals are rarely stationary in the long run. Sometimes the measured signal can, however, be assumed to be piecewise stationary. In such cases, the signal can be divided into stationary segments and each segment can be analyzed separately using traditional methods [10]. When the signal is notably nonstationary such a segmentation can not be accomplished, but time-varying analysis methods need to be utilized. For example, the time-varying spectrum of the signal can be obtained with *time-frequency representation* (TFR) methods such as the traditional *short-time Fourier transform* (STFT). Another nowadays popular TFR method is the *wavelet transform* (WT).

Both the STFT and WT, however, suffer from a trade-off between time and frequency resolutions. An alternative approach for calculating TFR is to use time-varying parametric spectrum estimation methods [60, 88]. A common approach is to use an *autoregressive* (AR) or *autoregressive moving average* (ARMA) model with time-varying parameters for the signal. The frequency resolution of parametric methods is superior to nonparametric TFRs [110], but not infinite. The main task in parametric methods is the estimation of the time-varying model parameters. For this, adaptive algorithms such as *Kalman filter*, originally proposed in [78], have been adopted. Along with a smoother algorithm, the tracking lag of adaptive filters can be avoided and an improved tracking of signal characteristics can be obtained. In this thesis, such algorithms are applied to estimation of nonstationary EEG signals.

In some cases, the measured signal contains a slow linear or more complex trend component and is, thus, characterized by nonstationary mean. The effect of the nonstationary mean on the analysis can be eliminated by removing the trend somehow. One should, however, always make sure that the trend component to be removed does not contain any valuable information, but is of irrelevant origin.

A simple method for removing trend components is to fit a first or higher order polynomial to the data [149, 101, 115], but also more advanced methods have been proposed [198].

The aims and contents of the thesis

The aim of this thesis is to propose novel methods for the analysis of both event-related and spontaneous biosignals. The first proposed method is a *principal component analysis* (PCA) based method for analyzing the patterning of successive GSR measurements. The second proposed method is an advanced detrending method with application to HRV analysis. This method is based on *smoothness priors regularization* theory. The third proposed method is concerned with the estimation of nonstationary EEG with a Kalman smoother algorithm.

The methods proposed in this thesis have been partly published in [174, 175, 176, 177, 172, 173]. The aim of this thesis is not only to summarize the results of these publications but also to give a more detailed presentation of the methods and their theoretical background. A common factor in the proposed methods is that they can all be presented in estimation theoretical framework. The aim of this thesis is to present the estimation theoretical background of each proposed method in a unified formalism.

In this thesis, two different data sets are mainly used. The recordings of the first data set, that has been mainly used in Chapter 5 for GSR analysis, was carried out by the Departments of Psychiatry and Clinical Neurophysiology at Kuopio University Hospital, Finland. The recordings were conducted on 20 healthy control subjects and 13 first-episode patients with acute psychosis admitted for hospital evaluation in supervision of a trained psychiatrist Minna Valkonen-Korhonen, MD. Several paradigms were conducted for each subject and EEG, ECG, and GSR were continuously recorded during the paradigms. The second data set, that has been used in Chapter 6 for event-related EEG analysis, was carried out in the Department of Clinical Neurophysiology, Kuopio University Hospital, Finland. These recordings were conducted on 6 healthy subjects and the experimental procedure was to close and open the eyes repeatedly at given intervals. All subjects in both data sets provided written informed consent and the studies were approved by the local ethical committee. In addition to the previous data sets, single measurements carried out in the Brain@Work Laboratory, Department of Occupational Medicine, Finnish Institute of Occupational Health, Helsinki, Finland and in the Department of Applied Physics, University of Kuopio, Finland are used in Chapter 7. The author has no credit for the measurements.

All the data analysis, text, and figures of this thesis, unless otherwise stated, are made by the author himself. In addition, the author is one of the key programmers of the Biosignal analysis software [1] and is mainly responsible, e.g., for the GSR, quantitative EEG, HRV, BPV, and *baroreflex sensitivity* (BRS) analysis tools.

The thesis is organized as follows. After the Introduction in Chapter 1, the theoretical framework for the proposed methods is given in Chapters 2–4 and each proposed method is presented in a separate chapter in Chapters 5–7.

In Chapter 2, the estimation theoretical background required in the rest of the thesis is presented. The required elements of probability theory are summarized and the concepts of *least squares estimation*, *regularization*, and *Bayesian estimation* are introduced. The end of Chapter 2 focuses on *mean square estimation* depicting the derivation of Kalman filter and smoothing algorithms. In Chapter 3, the results of estimation theory are applied to estimation of stationary time series models. The most common time series models, i.e. AR, MA, and ARMA models, are given and estimation of AR model parameters is considered. In addition, Chapter 3 contains the basics of spectrum estimation of stationary time series. In Chapter 4, the assumption of stationarity is dropped and the time series models are assumed to be time-varying. The most common adaptive algorithms for estimating the time-varying model parameters are presented and time-varying spectrum estimation is considered.

In Chapter 5, the PCA based method for analyzing the patterning of successive GSR measurements is presented. As a specific application the proposed method is applied to GSR measurements of 20 healthy control subjects and 13 psychotic patients. For most of the control subjects, there was a clear pattern in successive GSRs, whereas within psychotic patients the lack of time-locking of GSRs seemed to be characteristic.

In Chapter 6, the Kalman smoother approach for estimation of nonstationary EEG is presented. The estimation accuracy of the Kalman smoother is first evaluated with simulations and then compared to other popular TFRs. As a specific application the Kalman smoother approach is applied to estimation of *event-related synchronization/desynchronization* (ERS/ERD) dynamics of occipital alpha rhythm.

In Chapter 7, a review of methods used in the analysis of cardiovascular variability signals is given. The importance of preprocessing of these signals is emphasized and the proposed detrending method is described in detail. The effect of detrending on some general time-domain measures as well as spectrum estimates of HRV is studied.

The discussions of the proposed methods are placed separately after each chapter, respectively. The overall discussion and conclusions of the thesis are given at the end of the thesis in Chapter 8.

Chapter II

Estimation theory

Estimation theory is a fundamental tool required in time series analysis and system theory. For an extensive discussion on estimation theory see, e.g., [169]. In this chapter, only the necessary estimation theoretical background for the time series analysis and spectrum estimation methods presented in Chapters 3 and 4 will be given. A restriction on linear and discrete-time problems is made. In some places, references on extending the results to nonlinear case are given. The main references for this chapter are [6, 82, 88, 113, 118, 133, 169, 170].

2.1 Introduction

The problem in estimation theory is to determine the parameters describing the underlying system from noisy observations. In this thesis, x is used to denote the observations and θ the parameters. A basic approach to solve the estimation problem is to first define a model of some specific structure describing the dependency of the observations on the model parameters and then compute the parameters in some optimal way. Such a model is here referred to as *observation model*. The decision on model structure is usually based on some prior knowledge of the underlying system. Typically, the errors in the observations are considered additive and the observation model used is of the form

$$x = h(\theta) + e \tag{2.1}$$

where e is the additive error term and h is a function describing the underlying system. In some contexts e is referred to noise and the above model *additive noise model*.

In this thesis, the focus is on linear and discrete-time problems and a vector $x = (x_1, x_2, \ldots, x_N)^T \in \mathbb{R}^N$ is used to denote the discrete observations and $\theta = (\theta_1, \theta_2, \ldots, \theta_p)^T \in \mathbb{R}^p$ the parameters. The superscript $(\cdot)^T$ denotes transpose. The observations x can be considered to be sampled from a continuous signal $x(t)$ at discrete times $(t_1, t_2, \ldots, t_N)$. The sampling interval ΔT is usually assumed to be constant, i.e. $\Delta T = t_{j+1} - t_j = c$ for all j, and the sampling rate is given by $f_s = 1/\Delta T$. Then, the linear observation model is simply

$$x = H\theta + e \tag{2.2}$$

where H is a $p \times N$ matrix that does not contain parameters to be estimated. Throughout the thesis, H is often called *observation matrix*. The columns ψ_j $(j = 1, 2, \ldots, p)$ of H are called basis vectors. For an estimate of θ a notation $\hat{\theta}$ is used and the difference between the true and estimated parameters (i.e. the estimation error) is denoted $\tilde{\theta} = \theta - \hat{\theta}$. Furthermore, the estimation error of the observations, i.e. the residual, is given by $\epsilon = x - H\hat{\theta} = x - \hat{x}$.

2.2 Summary of probability theory

In this section, a short review of notations and definitions used in this thesis is given. The fundamental definitions of probability theory will not be discussed here. These definitions can be found, e.g., in [133].

One important concept of probability theory is that of random variables. A *random variable* x_j is a rule for assigning a value $x_j(\zeta)$ to every outcome ζ of an experiment, i.e. a function defined for all outcomes of the experiment. A *random vector* $x = (x_1, \ldots, x_N)^T$ is a vector whose components x_j are random variables. A *random process* $x(t)$, on the other hand, is a function of both time t and the outcome ζ, i.e. $x(t) = x(t, \zeta)$. For a fixed outcome ζ random process is a single function of time and for a fixed t it is a random variable x_t.

Let $x = (x_1, x_2, \ldots, x_N)^T \in \mathbb{R}^N$ and $y = (y_1, y_2, \ldots, y_M)^T \in \mathbb{R}^M$ be random vectors whose probability density functions are $p_x(x)$ and $p_y(y)$, respectively. Subscripts x and y of the density functions refer to the random variables and, according to a common practice, the same letters are used for the arguments of the density functions. Therefore, without a risk of confusion the subscripts can be omitted and the density functions denoted simply as $p(x)$ and $p(y)$. The joint probability density of x and y is denoted as $p(x, y)$.

The expected value or the mean η_x of a random vector x is defined as

$$\begin{aligned} \eta_x &= E\{x\} = \int_{\mathbb{R}^N} x\, p(x)\, dx && (2.3) \\ &= \int_{-\infty}^{\infty} \cdots \int_{-\infty}^{\infty} (x_1, \ldots, x_N)^T p(x_1, \ldots, x_N)\, dx_1 \cdots\, dx_N && (2.4) \\ &= (\eta_{x_1}, \ldots, \eta_{x_N})^T && (2.5) \end{aligned}$$

where the integral is taken over each random variable x_j. The mean η_x is also called the first moment of x. Higher moments are obtained correspondingly by integrating $x^n p(x)$. Of particular interest is the variance which is the second centered moment of x defined as

$$\sigma_x^2 = \mathrm{var}\{x\} = \int_{\mathbb{R}^N} (x - \eta_x)^2 p(x)\, dx. \tag{2.6}$$

Clearly, this is the expected value of the random vector $(x - \eta_x)^2$ which can also be written as

$$\sigma_x^2 = E\{(x - \eta_x)^2\} = E\{x^2\} - E\{x\}^2. \tag{2.7}$$

The correlation matrix of a random vector x is defined as

$$R_x = E\{xx^T\} = \begin{pmatrix} E\{x_1x_1\} & \cdots & E\{x_1x_N\} \\ \vdots & \ddots & \vdots \\ E\{x_Nx_1\} & \cdots & E\{x_Nx_N\} \end{pmatrix} \tag{2.8}$$

and the cross-correlation matrix of random vectors x and y as

$$R_{xy} = E\{xy^T\}. \tag{2.9}$$

Furthermore, the covariance matrix of a random vector x is defined as

$$C_x = E\{(x-\eta_x)(x-\eta_x)^T\} = E\{xx^T\} - \eta_x\eta_x^T \tag{2.10}$$

that is the correlation matrix of the centered random vector $(x-\eta_x)$. The cross-covariance matrix of x and y is

$$C_{xy} = E\{(x-\eta_x)(y-\eta_y)^T\} = E\{xy^T\} - \eta_x\eta_y^T. \tag{2.11}$$

The conditional probability density of x given y is defined as

$$p(x|y) = \frac{p(x,y)}{p(y)} \tag{2.12}$$

for $p(y) \neq 0$, otherwise $p(x|y) = 0$. Likewise, the conditional density of y given x is

$$p(y|x) = \frac{p(y,x)}{p(x)}. \tag{2.13}$$

Combining of equations (2.12) and (2.13) yields

$$p(x|y)p(y) = p(y|x)p(x) \tag{2.14}$$

which is the so-called *Bayes' theorem*. Another useful result that can be easily derived is that for the joint conditional density of x and y given z

$$p(x,y|z) = p(x|y,z)p(y|z). \tag{2.15}$$

The conditional mean of x given y is given by

$$\eta_{x|y} = E\{x|y\} = \int_{\mathbb{R}^N} x\, p(x|y)\, dx. \tag{2.16}$$

The components x_j of a random vector are said to be jointly Gaussian if their joint probability density is of the form

$$p(x) = \frac{1}{\sqrt{(2\pi)^N \det C_x}} \exp\left(-\frac{1}{2}(x-\eta_x)^T C_x^{-1}(x-\eta_x)\right) \tag{2.17}$$

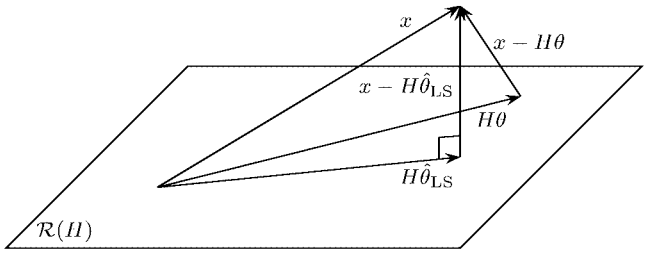

Figure 2.1: Projection of the observation x.

where $\det C_x$ is the determinant of C_x. A jointly Gaussian random vector x with mean η_x and covariance C_x is denoted as

$$x \sim \mathcal{N}(\eta_x, C_x). \tag{2.18}$$

If $y = Lx$, where L is an affine transformation, then y is also jointly Gaussian with probability density

$$p(y) = \frac{1}{\sqrt{(2\pi)^N \det(LC_xL^T)}} \exp\left(-\frac{1}{2}(y - L\eta_x)^T(LC_xL^T)^{-1}(y - L\eta_x)\right) \tag{2.19}$$

that is $y \sim \mathcal{N}(L\eta_x, LC_xL^T)$.

2.3 Least squares estimation

In this section, the *least squares* (LS) solution for the linear observation model

$$x = H\theta + e \tag{2.20}$$

where parameters θ and error term e are unknown, will be presented. In the nonlinear case, the LS solution is obtained using some iterative method such as *Gauss-Newton* or *steepest descent*. These methods are not, however, in the scope of this thesis, but an interested reader is referred to [95]. In the LS estimation, neither the parameters θ nor the observation error e is interpreted as random, but the LS estimation can be considered as a deterministic fit. The LS solution is defined as the vector θ that minimizes the squared error norm, i.e. the minimizer of the function

$$l(\theta) = \| x - H\theta \|^2 \tag{2.21}$$

where $\| \cdot \|$ is the Euclidean norm. The columns of matrix H span a p dimensional subspace $\mathcal{R}(H)$ which is often called as the *range* of H. It can be shown, that the function (2.21) is minimized by selecting θ so that the residual vector $x - H\theta$ is orthogonal to the subspace $\mathcal{R}(H)$ (see Fig. 2.1). Then, we can write

$$H^T(x - H\hat{\theta}_{\mathrm{LS}}) = 0 \tag{2.22}$$

which can also be written in the form

$$H^T H\hat{\theta}_{\mathrm{LS}} = H^T x. \tag{2.23}$$

The system of equations in (2.23) is often called the *normal equations* and the formal LS solution for the parameters θ is given as

$$\hat{\theta}_{\mathrm{LS}} = (H^T H)^{-1} H^T x. \tag{2.24}$$

This is a unique solution of the function (2.21) if the matrix $H^T H$ is positive definite. The LS estimate for the observations is, furthermore, obtained as

$$\hat{x}_{\mathrm{LS}} = H\hat{\theta}_{\mathrm{LS}}. \tag{2.25}$$

Note, that the residual $\epsilon = x - \hat{x}_{\mathrm{LS}}$ is orthogonal to $\mathcal{R}(H)$ and $\hat{x}_{\mathrm{LS}}$ is simply the orthogonal projection of x onto $\mathcal{R}(H)$.

2.4 Principal component analysis

Principal component analysis is a multivariate statistical procedure, where the random observations are transformed into a smaller set of uncorrelated variables called *principal components* (PCs). Even though, the observations are considered as random variables no assumptions about the probability densities are made in PCA. PCA was first introduced in [138, 64] and is equivalent to the *Karhunen-Loeve transform* [80, 103]. When the calculated PCs are used in any form in regression analysis the term *principal component regression* (PCR) is used instead of PCA [73]. Some typical applications of PCA include data reduction, feature extraction, and visualization of multidimensional data.

The starting point of PCA is the derivation of the PCs themselves. Consider that we have made M observations of a random vector $x \in \mathbb{R}^N$. Vectors x will span a vector space which will be at most of $\min\{N, M\}$ dimensions. The aim in PCA is to find $K < \min\{N, M\}$ PCs for each observation that will cover most of the variance in the observations. The first PC θ_1 for observation x is obtained as a linear combination of the elements of x

$$\theta_1 = \sum_{j=1}^{N} v_{j1} x_j = v_1^T x \tag{2.26}$$

where $v_1 = (v_{11}, v_{21}, \ldots, v_{N1})^T \in \mathbb{R}^N$ is a vector of scalar weights. The task is to find the vector v_1 so that the variance of θ_1, i.e. the variance of $v_1^T x$, is maximized. Clearly, to achieve the maximum variance for finite v_1 some constraints must be set. The most convenient constraint is $\| v_1 \| = 1$. The variance of the first PC is

$$\begin{aligned}
\mathrm{var}\{\theta_1\} &= E\{(v_1^T x - E\{v_1^T x\})^2\} && (2.27)\\
&= E\{(v_1^T (x - E\{x\}))^2\} && (2.28)\\
&= v_1^T E\{(x - \eta_x)(x - \eta_x)^T\} v_1 && (2.29)\\
&= v_1^T C_x v_1 \doteq \lambda_1. && (2.30)
\end{aligned}$$

Thus, the variance of the first PC is equal to the largest eigenvalue of the covariance matrix C_x and v_1 is the corresponding eigenvector. Next, a vector v_2 that maximizes the variance of $v_2^T x$ with constraint that $v_2^T x$ is uncorrelated with $v_1^T x$ is looked for. Furthermore, the third PC is obtained by finding vector v_3 that maximizes the variance of $v_3^T x$ with constraint that $v_3^T x$ is uncorrelated with $v_1^T x$ and $v_2^T x$ and so on. It turns out that, the k'th PC ($k = 1, 2, \ldots, K$) is obtained by selecting v_k to be the eigenvector of C_x corresponding to k'th largest eigenvalue λ_k [73].

2.4.1 Calculation of principal components

Next, the derivation of PCs for an ensemble of observations and the connection to LS estimation is presented. Let $X = (x_1, \ldots, x_M) \in \mathbb{R}^{N \times M}$ be a $N \times M$ matrix with the M observations in its columns and $H = (v_1, v_2, \ldots, v_K)$ a matrix with eigenvectors in its columns, and $\theta_{PC} = (\theta_1, \theta_2, \ldots, \theta_K)^T$ a $K \times M$ matrix with k'th PCs in the k'th row. So, the m'th element of θ_k is the k'th PC for the m'th observation. Then, according to equation (2.26), we can write

$$\theta_{PC} = H^T X. \tag{2.31}$$

Since the columns of H are eigenvectors of a symmetric matrix they are orthogonal. In addition, a constraint $\| v_k \| = 1$ was set and, therefore, the columns of H are in fact orthonormal. This means that $H^T H = I$, where I denotes identity matrix, and we can write

$$(H^T H)\theta_{PC} = H^T X. \tag{2.32}$$

This is of the same form as the least squares normal equations in (2.23). Therefore, it can be concluded that, if we select the basis vectors of the observation matrix to be the eigenvectors of the data covariance matrix the LS solution ends up to PCR. The estimates for the components are obtained as

$$\hat{\theta}_{PC} = (H^T H)^{-1} H^T X = H^T X \tag{2.33}$$

and the principal component transformation of the observations as

$$\hat{X}_{PC} = H\hat{\theta}_{PC} = HH^T X. \tag{2.34}$$

An important property of this transformation is the fact that it is the best orthogonal fit in the mean square error sense. Meaning that, prediction error $E\{\|X - \hat{X}\|^2\}$ is minimized with respect to using any other set of same amount of orthogonal basis vectors.

In the previous, the covariance matrix was used to extract the eigenvectors. In this case, the eigenvectors reflect variance and covariance structure of observations, while the mean of observations $E\{x\}$ is neglected. In some cases, it is not, however, desirable to remove the mean from the observations. In this case, the mean can be included in the observation matrix explicitly. Another approach is to use the correlation matrix instead of covariance to extract the eigenvectors [128]. Then the eigenvectors will also reflect the mean. This approach is analogous to the one using covariance matrix with the exception that quadratic mean $E\{\theta_k^2\}$ of PCs is maximized instead of variance.

2.5 Regularization theory

In this section, the basic ideas of regularization theory are introduced. The aim is to derive the smoothness priors regularization method, which will be used in Chapter 7 for preprocessing of heart rate variability time series. The term regularization arises from the area of *ill-posed problems* [57]. For such problems a unique solution does not exist or the solution is unstable. In the latter case, small errors in the observations can cause large error in the solution. Methods that are used to stabilize the problem such that the solution becomes unique or less sensitive to observation errors are called regularization methods. Probably the most popular such method is the *Tikhonov regularization* [181]. In the standard Tikhonov regularization, the functional to be minimized is of the form

$$l(\theta) = \| x - H\theta \|^2 + \kappa^2 \| \theta \|^2 \tag{2.35}$$

where $\kappa > 0$ is a regularization parameter that controls the significance of the second term in the functional. Clearly, the objective is not just to find the minimizer of the residual norm (first term) but to allow small deviation from it in order to find a solution with smaller norm.

In the more general form of Tikhonov regularization, the functional to be minimized is

$$l(\theta) = \| L_1(x - H\theta) \|^2 + \kappa^2 \| L_2(\theta - \theta^*) \|^2 \tag{2.36}$$

where L_1 is a weight matrix, L_2 is a regularization matrix, and θ^* is a prior guess for the solution. The regularization matrix L_2 is typically set to be either identity matrix or a discrete approximation D_d of d'th-order derivative. Methods using difference approximations in regularization can, in general, be called smoothness priors methods [88]. The difference approximations are banded matrices with full row ranks. For example, the second-order difference matrix D_2 is of the form

$$D_2 = \begin{pmatrix} 1 & -2 & 1 & 0 & \cdots & 0 \\ 0 & 1 & -2 & 1 & \ddots & \vdots \\ \vdots & \ddots & \ddots & \ddots & \ddots & 0 \\ 0 & \cdots & 0 & 1 & -2 & 1 \end{pmatrix} \in \mathbb{R}^{(N-2)\times N}. \tag{2.37}$$

2.5.1 Smoothness priors regularization

Next, a particular type of smoothness priors regularization is considered. Consider that there are no particular prior assumptions about the parameters θ or the parameters may not even have any physical meaning. On the other hand, there are some assumptions about the observations themself. In that case, the prediction $H\theta$ have to be regularized instead of θ. Let L_1 be the identity matrix, L_2 the d'th-order difference matrix D_d, and $\theta^* = 0$. Then functional (2.36) yields

$$l(\theta) = \| x - H\theta \|^2 + \kappa^2 \| D_d(H\theta) \|^2 . \tag{2.38}$$

By doing some rearrangements this can be written in the form

$$l(\theta) = \left\| \begin{pmatrix} x \\ 0 \end{pmatrix} - \begin{pmatrix} H \\ \kappa D_d H \end{pmatrix} \theta \right\|^2. \tag{2.39}$$

By making notations

$$x' = \begin{pmatrix} x \\ 0 \end{pmatrix}, \qquad H' = \begin{pmatrix} H \\ \kappa D_d H \end{pmatrix} \tag{2.40}$$

functional (2.39) returns to the form of the regular least squares functional (2.21) and, therefore, the solution can be written as

$$\hat{\theta}_\kappa = (H'^T H')^{-1} H'^T x' = (H^T H + \kappa^2 H^T D_d^T D_d H)^{-1} H^T x. \tag{2.41}$$

The selection of the observation matrix H can be implemented according to some known properties of the data x. For example, when the data is assumed to be smooth, a generic set of Gaussian basis functions or sigmoids can be used. If the only assumption is the smoothness the trivial choice of identity matrix for H, i.e. $H = I \in \mathbb{R}^{N \times N}$, can be used since the smoothing is enforced by the difference matrix D_d, anyway. In this case, the problem returns to the smoothing problem proposed in [198], where the observation x is assumed to consist of a smooth function $f = H\theta \in \mathbb{R}^N$ and observation noise, i.e. $x = f + e$. Clearly, for $\kappa = 0$ the trivial solution $f = x$ is obtained and for $\kappa^2 > 0$ the trivial solution is drawn toward the null space of the regularization matrix D_d. The null space of the second order difference matrix, for example, contains all first order curves and, thus, the solution will be smooth. The regularization parameter κ which controls the smoothness of the solution is also referred to as smoothing parameter. An evident application of this approach is the estimation of the trend of a nonstationary mean observation.

2.6 Bayesian estimation

So far, the parameters θ have been assumed to be unknown deterministic constants. In Bayesian estimation, the parameters are assumed to be random having a joint probability density $p(x, \theta)$ with the observations. The aim in Bayesian estimation is to solve the *posterior density* $p(\theta|x)$ of the parameters given the observations [113]. According to the Bayes' theorem (2.14) the posterior density is

$$p(\theta|x) = \frac{p(x|\theta)p(\theta)}{p(x)} \propto p(x|\theta)p(\theta) \tag{2.42}$$

where $p(x|\theta)$ is the conditional density of observations x given the parameters θ. In Bayesian estimation $p(x|\theta)$ is called the *likelihood density*. The densities $p(\theta)$ and $p(x)$ are the marginal densities of the parameters θ and observations x, respectively. In Bayesian estimation the marginal density $p(\theta)$ is replaced with a density that describes the knowledge and/or assumptions of the parameters prior

to any measurements. This replacement is not differentiated here and, thus, the marginal density $p(\theta)$ is also referred to as *prior density*. The marginal density of observations, given by $p(x) = \int p(\theta, x)\, d\theta = \int p(\theta)p(x|\theta)\, d\theta$, on the other hand, is only a scale factor when x is given.

The posterior density (2.42) is a complete solution for the estimation problem given the observations and the prior. It assigns a value for each point θ describing the probability of the solution for the given observations and prior. In practice, point estimates such as the mean are extracted from the posterior density and are given as solutions. The selection of the point estimates, in Bayesian estimation, is done by defining a cost function $C(\theta, \hat{\theta})$ that sets a unique typically real-valued cost for each combination of the true parameter values θ and the estimated values $\hat{\theta}$. The expected value of the cost function

$$B(\hat{\theta}) = E\Big\{C(\theta, \hat{\theta}(x))\Big\} = \int_{\mathbb{R}^N} \int_{\mathbb{R}^P} C(\theta, \hat{\theta}(x))p(\theta, x)\, d\theta\, dx \tag{2.43}$$

is called the *Bayes cost*. According to the Bayes estimation criterion [113] the optimal estimator $\hat{\theta}_B$ for the given cost function is the one that minimizes the Bayes cost, i.e.

$$B(\hat{\theta}_B) \leq B(\hat{\theta}) \tag{2.44}$$

for all $\hat{\theta}$. Different estimators can be derived depending on the choice of the cost function.

2.7 Mean square estimation

In the *mean square* (MS) estimation, the cost function is the squared norm of the estimation error $\tilde{\theta} = \theta - \hat{\theta}$, i.e.

$$C_{\mathrm{MS}}(\theta, \hat{\theta}) = \|\theta - \hat{\theta}\|^2 = (\theta - \hat{\theta})^T(\theta - \hat{\theta}). \tag{2.45}$$

The MS estimate is, thus, searched by minimizing the Bayes cost with the given cost function. By substituting (2.45) into (2.43) the Bayes cost can be written in the form

$$\begin{aligned} B(\hat{\theta}) &= \int_{\mathbb{R}^N} \int_{\mathbb{R}^P} \|\theta - \hat{\theta}\|^2 p(\theta, x)\, d\theta\, dx & (2.46)\\ &= \int_{\mathbb{R}^N} \Bigg(\underbrace{\int_{\mathbb{R}^P} \|\theta - \hat{\theta}\|^2 p(\theta|x)\, d\theta}_{B(\hat{\theta}|x)} \Bigg) p(x)\, dx. & (2.47) \end{aligned}$$

Because $p(x)$ is nonnegative, $B(\hat{\theta})$ is minimized by minimizing the inner integral in (2.47). This is done by taking the partial derivative of $B(\hat{\theta}|x)$ with respect to $\hat{\theta}$ and setting it to zero. This yields

$$\begin{aligned} \frac{\partial B(\hat{\theta}|x)}{\partial \hat{\theta}} &= \int_{\mathbb{R}^P} \frac{\partial}{\partial \hat{\theta}} (\theta^T\theta - 2\theta^T\hat{\theta}_{\mathrm{MS}} + \hat{\theta}_{\mathrm{MS}}^T\hat{\theta}_{\mathrm{MS}}) p(\theta|x)\, d\theta & (2.48)\\ &= \int_{\mathbb{R}^P} (2\hat{\theta}_{\mathrm{MS}} - 2\theta) p(\theta|x)\, d\theta = 0. & (2.49) \end{aligned}$$

Since $\hat{\theta}_{\mathrm{MS}}$ does not depend on θ, it can be taken outside the integral and the previous equation can be rearranged to yield

$$\hat{\theta}_{\mathrm{MS}} \int_{\mathbb{R}^p} p(\theta|x)\, d\theta = \int_{\mathbb{R}^p} \theta p(\theta|x)\, d\theta. \tag{2.50}$$

Since the integral over the conditional density is naturally equal to unity, it is concluded that

$$\hat{\theta}_{\mathrm{MS}} = \int_{\mathbb{R}^p} \theta p(\theta|x)\, d\theta = E\{\theta|x\} \tag{2.51}$$

i.e. the MS estimator is equal to the conditional mean of parameters θ given the observations x. Based on this, the estimator is sometimes also called as the *conditional mean estimator*. Furthermore, it could be easily shown that the expected value of the estimation error $\tilde{\theta} = \theta - \hat{\theta}_{\mathrm{MS}}$ is zero [113] and, therefore, the MS estimate is unbiased. Because $\tilde{\theta}$ is zero mean, the estimation error variance is of the form

$$\mathrm{var}\Big\{\tilde{\theta}\Big\} = E\Big\{\tilde{\theta}^T\tilde{\theta}\Big\} = E\Big\{(\theta - \hat{\theta})^T(\theta - \hat{\theta})\Big\} \tag{2.52}$$

and, thus, the conditional mean minimizes the variance of the estimation error. Therefore, $\hat{\theta}_{\mathrm{MS}}$ is also called *minimum error variance estimator* or just *minimum variance estimator* [113].

2.8 Maximum a posteriori estimation

Another possible cost function is the *uniform cost* (UC) function given by

$$C_{\mathrm{UC}}(\theta, \hat{\theta}) = \begin{cases} 0 & \text{if } |\tilde{\theta}_k| < \varepsilon,\ \forall k \\ 1 & \text{otherwise} \end{cases} \tag{2.53}$$

where ε is a small constant. This cost function gives zero penalty if all components of the estimation error $\tilde{\theta}$ are small and unit penalty if any of the components is larger than ε. By substituting this cost function into (2.43) it turns out that the optimum estimator for this cost function is the one that maximizes the posterior density $p(\hat{\theta}|x)$ [113], that is

$$p(\hat{\theta}_{\mathrm{UC}}|x) \geq p(\hat{\theta}|x), \quad \forall\hat{\theta}. \tag{2.54}$$

In other words, $\hat{\theta}_{\mathrm{UC}}$ is the mode[1] of the conditional density $p(\theta|x)$. Due to these results, the estimator $\hat{\theta}_{\mathrm{UC}}$ is called the *conditional mode estimator* or more commonly the *maximum a posteriori* (MAP) estimator $\hat{\theta}_{\mathrm{MAP}}$.

A useful equivalence can be easily observed. That is, if the posterior density $p(\theta|x)$ is symmetric and unimodal then the mode and the mean of the density function are the same. This means that the MS and MAP estimates are the same, i.e. $\hat{\theta}_{\mathrm{MS}} = \hat{\theta}_{\mathrm{MAP}}$. This equivalence will be utilized in Section 2.9 in the derivation of the Kalman filter equations.

[1] The mode is the value of θ that maximizes the density function $p(\theta)$.

2.9 Dynamic linear mean square estimation

So far in this chapter, the parameters θ have been considered time-invariant. Next, the system under consideration is assumed to be dynamic and the parameters θ time-varying. The time-varying parameters can be estimated in recursive manner with Kalman filter that was originally introduced in [78]. In Kalman filtering, the estimates of the parameters at certain time instant are calculated by updating the previous estimates each time a new data point is available. The derivation of the Kalman filter equations, presented in this section, is based on the one given in [113]. Another popular approach is to use the so-called *innovations* in the derivation [60].

The formulation of the Kalman filter equations is based on *state-space formalism*, which is one of the fundamental models of system theory [88]. Let x_t be a random process and $\theta_t \in \mathbb{R}^p$ a vector valued random process. The evolution of the state θ_t is described with the linear equation

$$\theta_{t+1} = F_t\theta_t + G_t w_t \tag{2.55}$$

where F_t and G_t are known matrices and w_t is a zero-mean random process with covariance $C_{w_t} = \mathrm{cov}\{w_{t_1}, w_{t_2}\} = \sigma_w^2(t_1)$ for $t_1 = t_2$ and 0 otherwise. The subscript t denotes the discrete time instant. The observation x_t depends on the state θ_t according to the linear observation model

$$x_t = H_t\theta_t + e_t \tag{2.56}$$

where H_t is a known observation matrix and e_t is a zero-mean random process with covariance $C_{e_t} = \mathrm{cov}\{e_{t_1}, e_{t_2}\} = \sigma_e^2(t_1)$ for $t_1 = t_2$ and 0 otherwise. Noise processes w_t and e_t are assumed to be uncorrelated so that $\mathrm{cov}\{w_j, e_k\} = 0$ for all j and k.

There are two approaches for obtaining the linear mean square estimate. The first one is to specify a linear conditional mean and find the best linear form. The second approach, which is adopted here, is to assume noise processes w_t and e_t to be Gaussian. As shown in [113], the conditional mean for Gaussian variables is linear and, therefore, the two approaches are identical. This leads to the well known fact that the Kalman filter is the optimal estimator if the Gaussian assumptions are valid and no matter what the distributions are it is still an optimal linear estimator.

The aim is then to find the MS estimate for each state θ_t given the observations $X_t = (x_1, x_2, \ldots, x_t) \in \mathbb{R}^t$. As shown in Section 2.7, this is equal to the conditional mean

$$\hat{\theta}_t = E\{\theta_t | X_t\}\,. \tag{2.57}$$

Because of the Gaussian assumptions, the MAP estimate is equal with the MS estimate. Since the derivations are simpler for the MAP estimate, it is used here. The posterior density to be maximized can be written as

$$p(\theta_t|X_t) = \frac{p(\theta_t, X_t)}{p(X_t)} = \frac{p(\theta_t, X_{t-1}, x_t)}{p(X_{t-1}, x_t)}. \tag{2.58}$$

The numerator of this can be written as

$$p(\theta_t, X_{t-1}, x_t) = p(x_t|\theta_t, X_{t-1})p(\theta_t, X_{t-1}) \quad (2.59)$$
$$= p(x_t|\theta_t, X_{t-1})p(\theta_t|X_{t-1})p(X_{t-1}) \quad (2.60)$$

where $p(x_t|\theta_t, X_{t-1}) = p(x_t|\theta_t)$ since if θ_t is given, the only random variable in the observation model (2.56) is e_t, which does not depend on either θ_t or X_{t-1}. By substituting (2.60) along with the above observation the posterior density (2.58) can be written as

$$p(\theta_t|X_t) = \frac{p(x_t|\theta_t)p(\theta_t|X_{t-1})p(X_{t-1})}{p(X_{t-1}, x_t)}. \quad (2.61)$$

The denominator can also be written as $p(X_{t-1}, x_t) = p(x_t|X_{t-1})p(X_{t-1})$ and, thus, the posterior density becomes

$$p(\theta_t|X_t) = \frac{p(x_t|\theta_t)p(\theta_t|X_{t-1})}{p(x_t|X_{t-1})} \quad (2.62)$$

which is now of the desired form. The posterior density can then be determined by evaluating each of the densities on the right hand side of (2.62). Note that the denominator density $p(x_t|X_{t-1})$ does not contain θ_t, but is only a scale factor and, thus,

$$p(\theta_t|X_t) \propto p(x_t|\theta_t)p(\theta_t|X_{t-1}). \quad (2.63)$$

Since both of the densities on the right hand side of (2.63) are Gaussian, only the means and covariances need to be derived in order to evaluate the densities. The mean and covariance for the density $p(x_t|\theta_t)$ are

$$\eta_{x_t|\theta_t} = E\{x_t|\theta_t\} = E\{H_t\theta_t + e_t|\theta_t\} = H_t\theta_t \quad (2.64)$$
$$C_{x_t|\theta_t} = E\Big\{(H_t\theta_t + e_t - \eta_{x_t|\theta_t})(H_t\theta_t + e_t - \eta_{x_t|\theta_t})^T|\theta_t\Big\} = C_{e_t} \quad (2.65)$$

and so $p(x_t|\theta_t)$ is of the form

$$p(x_t|\theta_t) \propto \exp\left(-\frac{1}{2}(x_t - H_t\theta_t)^T C_{e_t}^{-1}(x_t - H_t\theta_t)\right) \quad (2.66)$$

where the scale factor of the normal distribution (2.17) have been omitted. Similarly, the mean and covariance for the density $p(\theta_t|X_{t-1})$ are

$$\eta_{\theta_t|X_{t-1}} = E\{F_{t-1}\theta_{t-1} + G_{t-1}w_{t-1}|X_{t-1}\} \quad (2.67)$$
$$= F_{t-1}\hat{\theta}_{t-1} \doteq \hat{\theta}_{t|t-1} \quad (2.68)$$
$$C_{\theta_t|X_{t-1}} = E\Big\{(\theta_t - \eta_{\theta_t|X_{t-1}})(\theta_t - \eta_{\theta_t|X_{t-1}})^T|X_{t-1}\Big\} \quad (2.69)$$
$$= E\Big\{\tilde{\theta}_{t|t-1}\tilde{\theta}_{t|t-1}^T|X_{t-1}\Big\} = C_{\tilde{\theta}_{t|t-1}} \quad (2.70)$$

where $\hat{\theta}_{t|t-1}$ is the estimate for state θ_t given observations X_{t-1} and $C_{\tilde{\theta}_{t|t-1}}$ is to be determined. The density $p(\theta_t|X_{t-1})$ is, thus, of the form

$$p(\theta_t|X_{t-1}) \propto \exp\left(-\frac{1}{2}(\theta_t - \hat{\theta}_{t|t-1})^T C^{-1}_{\tilde{\theta}_{t|t-1}}(\theta_t - \hat{\theta}_{t|t-1})\right). \tag{2.71}$$

Next, in order to find the MAP estimate, the value of θ_t that maximizes the posterior density (2.63) need to be evaluated. Here, the usual approach of maximizing the logarithm of $p(\theta_t|X_t)$ instead of $p(\theta_t|X_t)$ itself is taken. The logarithm of (2.63) given (2.66) and (2.71) is

$$\ln p(\theta_t|X_t) \propto (x_t - H_t\theta_t)^T C^{-1}_{e_t}(x_t - H_t\theta_t) + (\theta_t - \hat{\theta}_{t|t-1})^T C^{-1}_{\tilde{\theta}_{t|t-1}}(\theta_t - \hat{\theta}_{t|t-1}). \tag{2.72}$$

The MAP estimate $\hat{\theta}_t$ is then obtained by taking the partial derivative of the previous expression with respect to θ_t and setting it to zero. This yields

$$H_t^T C^{-1}_{e_t}(x_t - H_t\hat{\theta}_t) - C^{-1}_{\tilde{\theta}_{t|t-1}}(\hat{\theta}_t - \hat{\theta}_{t|t-1}) = 0. \tag{2.73}$$

Solving this for $\hat{\theta}_t$ gives

$$\hat{\theta}_t = (H_t^T C^{-1}_{e_t} H_t + C^{-1}_{\tilde{\theta}_{t|t-1}})^{-1}(C^{-1}_{\tilde{\theta}_{t|t-1}}\hat{\theta}_{t|t-1} + H_t^T C^{-1}_{e_t} x_t). \tag{2.74}$$

To put this into a more convenient form, the following matrix inversion lemma is used. If C_1 and C_2 are symmetric and positive definite then

$$(A^T C_1^{-1} A + C_2^{-1})^{-1} = C_2 - C_2 A^T (AC_2 A^T + C_1)^{-1} AC_2. \tag{2.75}$$

By using this lemma and after some simple but lengthy calculations equation (2.74) can be written as [113]

$$\hat{\theta}_t = \hat{\theta}_{t|t-1} + K_t(x_t - H_t\hat{\theta}_{t|t-1}) \tag{2.76}$$

where the so-called *Kalman gain* matrix K_t is

$$K_t = C_{\tilde{\theta}_{t|t-1}} H_t^T (H_t C_{\tilde{\theta}_{t|t-1}} H_t^T + C_{e_t})^{-1}. \tag{2.77}$$

Equation (2.76) is now of the desired recursive form. It is seen that the estimate $\hat{\theta}_t$ is obtained by correcting the prediction $\hat{\theta}_{t|t-1}$ given by (2.68) with the one step prediction error $x_t - H_t\hat{\theta}_{t|t-1}$ of the observation x_t weighted by the Kalman gain matrix K_t.

Before the algorithm is complete, the computation of the error covariance $C_{\tilde{\theta}_{t|t-1}}$ needs to be determined. The prediction error can be written as

$$\tilde{\theta}_{t|t-1} = \theta_t - \hat{\theta}_{t|t-1} = F_{t-1}\theta_{t-1} + G_{t-1}w_{t-1} - F_{t-1}\hat{\theta}_{t-1} \tag{2.78}$$

$$= F_{t-1}\tilde{\theta}_{t-1} + G_{t-1}w_{t-1} \tag{2.79}$$

and, therefore, $C_{\tilde{\theta}_{t|t-1}}$ can be written as

$$C_{\tilde{\theta}_{t|t-1}} = E\Big\{(F_{t-1}\tilde{\theta}_{t-1} + G_{t-1}w_{t-1})(F_{t-1}\tilde{\theta}_{t-1} + G_{t-1}w_{t-1})^T\Big\} \quad (2.80)$$

$$= F_{t-1}C_{\tilde{\theta}_{t-1}}F_{t-1}^T + G_{t-1}C_{w_{t-1}}G_{t-1}^T \quad (2.81)$$

since $\tilde{\theta}_{t-1}$ and w_{t-1} are uncorrelated. Furthermore, the estimation error can be written as

$$\tilde{\theta}_t = \theta_t - \hat{\theta}_t = \theta_t - \hat{\theta}_{t|t-1} - K_t(x_t - H_t\hat{\theta}_{t|t-1}). \quad (2.82)$$

By inserting $x_t = H_t\theta_t + e_t$ this becomes

$$\tilde{\theta}_t = \tilde{\theta}_{t|t-1} - K_t(H_t\tilde{\theta}_{t|t-1} + e_t) = (I - K_tH_t)\tilde{\theta}_{t|t-1} - K_te_t. \quad (2.83)$$

The error covariance is then of the form

$$C_{\tilde{\theta}_t} = (I - K_tH_t)C_{\tilde{\theta}_{t|t-1}}(I - K_tH_t)^T + K_tC_{e_t}K_t^T \quad (2.84)$$

which can be reduced to yield

$$C_{\tilde{\theta}_t} = (I - K_tH_t)C_{\tilde{\theta}_{t|t-1}}. \quad (2.85)$$

The derivation of the Kalman filter algorithm is now complete. The algorithm consisting of equations (2.68), (2.76), (2.77), (2.81), and (2.85) can be summarized as

$$\hat{\theta}_{t|t-1} = F_{t-1}\hat{\theta}_{t-1} \quad (2.86)$$

$$C_{\tilde{\theta}_{t|t-1}} = F_{t-1}C_{\tilde{\theta}_{t-1}}F_{t-1}^T + G_{t-1}C_{w_{t-1}}G_{t-1}^T \quad (2.87)$$

$$K_t = C_{\tilde{\theta}_{t|t-1}}H_t^T(H_tC_{\tilde{\theta}_{t|t-1}}H_t^T + C_{e_t})^{-1} \quad (2.88)$$

$$\hat{\theta}_t = \hat{\theta}_{t|t-1} + K_t(x_t - H_t\hat{\theta}_{t|t-1}) \quad (2.89)$$

$$C_{\tilde{\theta}_t} = (I - K_tH_t)C_{\tilde{\theta}_{t|t-1}}. \quad (2.90)$$

To initialize the algorithm, the prior knowledge of $\hat{\theta}_0 = E\{\theta_0\}$ and $C_{\tilde{\theta}_0} = C_{\theta_0}$ of the state is required.

2.10 Smoothing

In the Kalman filter algorithm, the state estimate is updated immediately after a new observation is available. Such a real time processing is not, however, always necessary. Instead, if a small lag in the processing is allowed or if the data is processed off-line, also the future observations can be used in the state estimation. In this case, it is reasonable to expect the estimates to be more accurate. Such an estimator, which uses observations $x_1, \ldots, x_{t+L}$ to estimate the state θ_t at time instant t, is called a *smoother*.

Historically, three different kinds of smoothers have been proposed, namely *fixed-point*, *fixed-lag*, and *fixed-interval smoothers* [6]. The fixed-point smoothing

is useful, for example, when the initial state of a process is to be estimated while the process progresses and new data is obtained. The fixed-point smoothing problem is to find estimates $\hat{\theta}_{j|L}$ for fixed j and all L. The fixed-lag smoothing, on the other hand, is suitable for online processing of the data when a small delay of L data points is allowed in the estimation of the state. In fixed-lag smoothing estimates $\hat{\theta}_{t-L|t}$ for each t and fixed L are to be obtained. Here, only the third smoothing approach, i.e. the fixed-interval smoothing, is considered. The fixed-interval smoothing is suitable for off-line processing of finite data sets. In addition to these three historical smoothers various computationally more efficient smoothing algorithms such as the one in [38] have been proposed.

The fixed-interval smoothing problem is to find estimates $\hat{\theta}_{t|N}$ for each state θ_t $(t = 1, \ldots, N)$ given all the observations $X_N = (x_1, \ldots, x_N)$. The MS estimate for this is equal to the conditional mean

$$\hat{\theta}_{t|N} = E\{\theta_t | X_N\}\,. \tag{2.91}$$

Different approaches for the derivation of the fixed-interval smoothing equations have been presented. One quite straightforward approach is to use an optimal forward-backward filter formulation [43]. Another approach, which will be adopted here, is to derive the smoothing equations in Bayesian point of view similar to the derivation of the Kalman filter presented in the previous section. This approach was presented in [153] and is sometimes referred to *Rauch-Tung-Striebel* form of smoothing equations.

Similar to the derivation of the Kalman filter, Gaussian variables are assumed and, therefore, the MS estimate can be replaced with MAP estimate. Thus, $\hat{\theta}_{t|N}$ is the value of θ_t that maximizes the posterior density $p(\theta_t|X_N)$. Similarly, $\hat{\theta}_{t|N}$ and $\hat{\theta}_{t+1|N}$ are the values of θ_t and θ_{t+1} that maximize the density $p(\theta_t, \theta_{t+1}|X_N)$. This joint posterior density can be written as

$$p(\theta_t, \theta_{t+1}|X_N) = \frac{p(\theta_t, \theta_{t+1}, X_N)}{p(X_N)} \tag{2.92}$$

$$= \frac{p(\theta_t, \theta_{t+1}, x_{t+1}, \ldots, x_N|X_t)p(X_t)}{p(x_{t+1}, \ldots, x_N|X_t)p(X_t)}. \tag{2.93}$$

Reducing the terms $p(X_t)$ and noting that the denominator is just a scale factor this yields

$$p(\theta_t, \theta_{t+1}|X_N) \propto p(\theta_t, \theta_{t+1}, x_{t+1}, \ldots, x_N|X_t). \tag{2.94}$$

Applying the result given in (2.15) this can be written as

$$p(\theta_t, \theta_{t+1}|X_N) \propto p(\theta_{t+1}, x_{t+1}, \ldots, x_N|\theta_t, X_t)p(\theta_t|X_t) \tag{2.95}$$

where $p(\theta_{t+1}, x_{t+1}, \ldots, x_N)$ does not depend on X_t when θ_t is given. Thus, applying (2.15) again yields

$$p(\theta_t, \theta_{t+1}|X_N) \propto p(x_{t+1}, \ldots, x_N|\theta_{t+1}, \theta_t)p(\theta_{t+1}|\theta_t)p(\theta_t|X_t) \tag{2.96}$$

$$\propto p(x_{t+1}, \ldots, x_N|\theta_{t+1})p(\theta_{t+1}|\theta_t)p(\theta_t|X_t) \tag{2.97}$$

which is now of desired form.

Next, it is assumed that the filtered estimate $\hat{\theta}_t$ is already determined and the maximum of the posterior density is searched for. For this the means and covariances of the densities on the right hand side of (2.97) need to be evaluated. It is, however, noted that the first term $p(x_{t+1}, \ldots, x_N|\theta_{t+1})$ does not contain θ_t and can, therefore, be neglected [153]. The mean and covariance for the second term $p(\theta_{t+1}|\theta_t)$ are given as

$$\begin{aligned} \eta_{\theta_{t+1}|\theta_t} &= F_t\theta_t & (2.98)\\ C_{\theta_{t+1}|\theta_t} &= E\{(F_t\theta_t + G_t w_t - \eta_{\theta_{t+1}|\theta_t})(F_t\theta_t + G_t w_t - \eta_{\theta_{t+1}|\theta_t})^T|\theta_t\} & (2.99)\\ &= G_t C_{w_t} G_t^T. & (2.100) \end{aligned}$$

The mean and covariance for the third term $p(\theta_t|X_t)$ are simply given by substituting $t-1$ to t in equations (2.68) and (2.70). This yields

$$\eta_{\theta_t|X_t} = \hat{\theta}_t, \quad C_{\theta_t|X_t} = C_{\tilde{\theta}_t}. \tag{2.101}$$

Now, the posterior density (2.97) is sufficiently determined and the logarithm of it is of the form

$$\begin{aligned} \ln p(\theta_t, \theta_{t+1}|X_N) \quad \propto \quad & B + (\theta_{t+1} - F_t\theta_t)^T (G_t C_{w_t} G_t^T)^{-1} (\theta_{t+1} - F_t\theta_t) \\ & + (\theta_t - \hat{\theta}_t)^T C_{\tilde{\theta}_t}^{-1} (\theta_t - \hat{\theta}_t) \end{aligned} \tag{2.102}$$

where B represents the terms arising from the first density in (2.97) that does not depend on θ_t. Deriving this with respect to θ_t and setting the result to zero yields

$$-F_t^T (G_t C_{w_t} G_t^T)^{-1} (\hat{\theta}_{t+1|N} - F_t\hat{\theta}_{t|N}) + C_{\tilde{\theta}_t}^{-1} (\hat{\theta}_{t|N} - \hat{\theta}_t) = 0. \tag{2.103}$$

Using the matrix inversion lemma (2.75) once again and after some lengthy calculations this can be written in the desired form

$$\hat{\theta}_{t|N} = \hat{\theta}_t + A_t(\hat{\theta}_{t+1|N} - \hat{\theta}_{t+1|t}) \tag{2.104}$$

where

$$A_t = C_{\tilde{\theta}_t} F_t^T C_{\tilde{\theta}_{t+1|t}}^{-1}. \tag{2.105}$$

This is the solution of the fixed-interval smoothing problem. Note, that the smoothed estimates are obtained by running the stored filter estimates $\hat{\theta}_t$ and $\hat{\theta}_{t+1|t}$ backwards in time by taking $t = N-1, N-2, \ldots, 1$. Also the error covariances $C_{\tilde{\theta}_t}$ and $C_{\tilde{\theta}_{t+1|t}}$ need to be stored. For the initialization, the filtered estimate $\hat{\theta}_N$ is used, i.e. $\hat{\theta}_{N|N} = \hat{\theta}_N$.

For the error covariance, similar recursive equation can be derived by examining the estimation error $\tilde{\theta}_{t|N}$ of the smoothed estimate. This results in the recursion [153]

$$C_{\tilde{\theta}_{t|N}} = C_{\tilde{\theta}_t} + A_t(C_{\tilde{\theta}_{t+1|N}} - C_{\tilde{\theta}_{t+1|t}})A_t^T \tag{2.106}$$

which completes the solution of the fixed-interval smoothing problem.

Chapter III

Stationary time series models

This chapter is concerned with stationary time series models. The most popular parameter models, that is AR, MA, and ARMA models, which are commonly used in time series analysis are presented. The estimation of AR model parameters is a linear estimation problem and few popular procedures for solving AR parameters are presented in Section 3.3. Here, only the transversal structure of the AR equations will be considered. Another common structure, i.e. the lattice structure, for these equations is presented, e.g., in [110]. The estimation of MA or ARMA parameters, on the other hand, is a nonlinear problem and is not considered in this chapter. The end of the chapter is focused on spectrum estimation of stationary time series with a division into classical Fourier transform based and parametric spectrum estimation methods. The main references for this chapter are [84, 110, 118, 133, 134, 151].

3.1 Stochastic processes and stationarity

As given in Section 2.2, a random or *stochastic process* $x(t)$ maps the outcomes ζ_j of an experiment to a set of time dependent functions $x(t, \zeta_j)$. The collection of all possible functions is called *ensemble* and a particular function is called a *realization* of the process. In other words, a random process is a family of random variables x_t, where t belongs to some given index set [151]. If t represents time and the given index set is the real axis, i.e. $t \in \mathbb{R}$, then $x_t = x(t)$ is a continuous-time process. If the index set is a set of integers, for example $t = 1, 2, \ldots$, then the process is said to be a discrete-time process, a *time series*. Here, only discrete-time processes x_t of finite length ($t = 1, 2, \ldots, N$) and with real valued variables are considered.

The mean of a discrete-time random process x_t is defined as

$$E\{x_t\} = \int_{-\infty}^{\infty} x\, p(x_t)\, dx = \eta_{x_t} \tag{3.1}$$

for all t. The autocorrelation $r_x(t_1, t_2)$ of process x_t is the expected value of the

product $x_{t_1}x_{t_2}$, i.e.

$$r_x(t_1,t_2) = E\{x_{t_1}x_{t_2}\} = \int_{-\infty}^{\infty}\int_{-\infty}^{\infty} x_1 x_2 p(x_{t_1}, x_{t_2})\, dx_1\, dx_2 \tag{3.2}$$

which is a function of the two time indices t_1 and t_2. The autocovariance $\gamma_x(t_1,t_2)$ of x_t is the covariance of random variables x_{t_1} and x_{t_2}

$$\begin{aligned}\gamma_x(t_1,t_2) &= E\{(x_{t_1} - \eta_{x_{t_1}})(x_{t_2} - \eta_{x_{t_2}})\} &(3.3)\\ &= r_x(t_1,t_2) - \eta_{x_{t_1}}\eta_{x_{t_2}}. &(3.4)\end{aligned}$$

The cross-covariance of random processes x_t and y_t is defined as

$$\gamma_{xy}(t_1,t_2) = r_{xy}(t_1,t_2) - \eta_{x_{t_1}}\eta_{y_{t_2}}. \tag{3.5}$$

If $\gamma_{xy}(t_1,t_2) = 0$ for all t_1 and t_2 the processes x_t and y_t are said to be uncorrelated. Similarly, if $r_{xy}(t_1,t_2) = 0$ for all t_1 and t_2 they are said to be orthogonal.

The stochastic process is said to be stationary if its statistical properties do not change over time. The complete stationarity presumes that the joint probability distribution of $(x_{t_1},\ldots,x_{t_n})$ is identical to that of $(x_{t_1+\tau},\ldots,x_{t_n+\tau})$ for all admissible $t_1,\ldots,t_n$ and all τ. An important subclass of stochastic processes consists of *wide-sense stationary* (WSS) processes. For WSS process x_t the mean is constant, i.e.

$$E\{x_t\} \equiv \eta \tag{3.6}$$

for all t, and the autocorrelation $r_x(t_1,t_2)$ depends only on the lag $\tau = t_2 - t_1$

$$r_x(t_1,t_2) = r_x(\tau). \tag{3.7}$$

For each τ, the autocorrelation sequence $r_x(\tau)$ measures the correlation between process values separated by interval τ. Clearly, $r_x(0) \geq r_x(\tau)$ for any τ and the correlation tends to weaken when τ increases, but it can have humps even for large τ (e.g. for cyclic processes). Another useful property of the autocorrelation sequence is that $r_x(\tau) = r_x(-\tau)$. In addition, the autocorrelation matrix

$$R_x = \begin{pmatrix} r_x(0) & r_x(1) & \ldots & r_x(L) \\ r_x(1) & r_x(0) & \ldots & r_x(L-1) \\ \vdots & \vdots & \ddots & \vdots \\ r_x(L) & r_x(L-1) & \ldots & r_x(0) \end{pmatrix} \tag{3.8}$$

formed from autocorrelation sequence components up to lag L is by definition positive semidefinite, that is, for arbitrary vector $a = (a_1,\ldots,a_{L+1})^T$

$$a^T R_x a = \sum_{j=1}^{L+1}\sum_{k=1}^{L+1} a_j a_k r_x(k-j) \geq 0. \tag{3.9}$$

This can be proved by examining the expectation of $|\sum_{j=1}^{L+1} a_j x_j|^2$ [133].

An important problem in the theory of stochastic processes is the estimation of the various statistics. Especially, since in many practical situations only a single realization of the process is observed. In such cases, the estimation of the ensemble averages is impossible. However, if the process is *ergodic*, which is in general true for stationary processes, the ensemble averages can be replaced with the appropriate time averages. That is, for an ergodic process

$$\frac{1}{N}\sum_{t=1}^{N} x_t \xrightarrow[N\to\infty]{} E\{x_t\}\,. \tag{3.10}$$

Thus, the mean of an ergodic process can be approximated with the time average

$$\eta = \frac{1}{N}\sum_{t=1}^{N} x_t. \tag{3.11}$$

Correspondingly, the autocorrelation sequence $r_x(\tau)$ can be estimated by averaging all the possible products $x_t x_{t+\tau}$. This yields

$$r_x(\tau) = \frac{1}{N-|\tau|}\sum_{t=1}^{N-|\tau|} x_t x_{t+|\tau|}. \tag{3.12}$$

This is an unbiased estimate of the autocorrelation but it can lead to autocorrelation matrix which is not positive semidefinite [110]. Therefore, the biased estimate

$$r_x(\tau) = \frac{1}{N}\sum_{t=1}^{N-|\tau|} x_t x_{t+|\tau|} \tag{3.13}$$

which always leads to positive semidefinite autocorrelation matrix, is usually used instead. Clearly, both of these estimates for the autocorrelation have the same property, namely the bigger the lag τ is the less terms are included in the average. Therefore, the accuracy of the autocorrelation estimate is decreased for bigger lags.

Additional information about the process of interest can be achieved by presenting the process in frequency-domain using the *power spectrum* or *power spectral density* (PSD) representation of the process. The power spectral density P_x of process x_t is defined as the Fourier transform of the autocorrelation sequence

$$P_x(\omega) = \sum_{\tau=-\infty}^{\infty} r_x(\tau) e^{-i\omega\tau} \tag{3.14}$$

where $i = \sqrt{-1}$ is the imaginary unit and $\omega \in [-\pi, \pi]$ is the angular frequency $\omega = 2\pi f$. The calculation of the Fourier transform and methods for estimating (3.14) are discussed in Section 3.5.

3.2 Autoregressive and moving average parameter models

Basically, the term model refers to any hypothesis that can describe the generation of the observed process or signal. The observed time series, denoted by x_t, is now assumed to be a WSS process with zero mean. The most common parameter models used in time series analysis are the AR, MA, and ARMA models. The most popular one of these parameter models is surely the AR model.

The time series x_t is said to be an AR process of order p, i.e. an AR(p) process, if it satisfies the difference equation

$$x_t = -\sum_{j=1}^{p} a_j x_{t-j} + e_t \tag{3.15}$$

where $a_1, a_2, \ldots, a_p$ are the parameters of the AR model and e_t is a white noise process. A white noise process e_t is a random process with zero mean, for which the correlation sequence is

$$r_e(\tau) = \begin{cases} 0, & \tau \neq 0 \\ \sigma_e^2, & \tau = 0 \end{cases} . \tag{3.16}$$

In other words, the components of a white noise process are uncorrelated with variance σ_e^2. The correlation sequence can also be presented using the Dirac delta function as $r_e(\tau) = \sigma_e^2 \delta(\tau)$. By substituting (3.16) into (3.14) it is observed that the spectrum of a white noise process is flat, i.e. $P_e(\omega) = \sigma_e^2$ for all ω. The distribution of the random variables e_t is usually assumed to be Gaussian, i.e.

$$e_t \sim \mathcal{N}(0, \sigma_e^2 I). \tag{3.17}$$

For Gaussian variables the uncorrelated components of e_t are also independent and the term *iid* (independent identically distributed) is also used instead of white noise [118]. As the term autoregressive indicates, the present value of the process x_t is generated (regressed) on the p previous values $x_{t-1}, \ldots, x_{t-p}$. In addition, randomness is introduced into the process by the noise term e_t.

In the AR modeling, the observed time series x_t (e.g. measured biosignal) is technically assumed to be an AR process of some specific order p. Then, the model parameters a_j are estimated so that the variance of the prediction error or residual ϵ_t

$$\epsilon_t = x_t + \sum_{j=1}^{p} a_j x_{t-j} \tag{3.18}$$

is minimized in some sense. In the case of AR model, these estimation methods are linear and, thus, easy to implement. In the next section, two common methods for estimating the AR parameters are presented, namely the *Yule-Walker* (YW) and least squares methods.

Another general class of time series models is the MA model. Time series x_t is called a MA process of order q, denoted by MA(q), if it satisfies

$$x_t = \sum_{k=0}^{q} b_k e_{t-k} \tag{3.19}$$

where $b_0, b_1, \ldots, b_q$ are the MA parameters and e_t is a white noise process. By comparing the AR and MA models it is noted that the white noise process e_t is used in both models. The difference between the models is, however, that in AR model the value of e_t influences the value x_t and, thereby, also all the future values $x_{t+1}, x_{t+2}, \ldots$. In the MA model, on the other hand, the value of e_t influences only a finite extent of future values of x_t, namely $x_{t+1}, \ldots, x_{t+q}$. This difference accounts for the fact that the autocorrelation function of an MA(q) process cuts off after lag q, whereas the autocorrelation function of an AR(p) process extincts gradually [151].

A natural generalization of AR and MA models is to combine them to yield a mixed autoregressive moving average model. The process x_t is called ARMA(p,q) process if it satisfies the difference equation

$$x_t = -\sum_{j=1}^{p} a_j x_{t-j} + \sum_{k=0}^{q} b_k e_{t-k} \tag{3.20}$$

where $a_1, a_2, \ldots, a_p$ and $b_0, b_1, \ldots, b_q$ are the AR and MA parameters respectively. Clearly, AR and MA models are special cases of an ARMA model. The AR model is obtained by setting $q = 0$ and $b_0 = 1$ in the ARMA model and, correspondingly, the MA model by setting $p = 0$.

3.3 AR parameter estimation

The procedure of fitting a parameter model to observed time series can be divided into three separate steps. The first step is to identify the general structure of the model which would be most appropriate. This is usually done according to the prevailing practice in the field of application and the case of implementation may also have some weight. In addition, examination of the data autocorrelation function and, especially, spectral analysis of observed data can be useful approaches in the selection of the model structure. The second step in the model identification is the selection of the model order. For this, various criteria have been developed. All these criteria, however, employ the estimates of the model parameters and, thus, the final step of parameter estimation is considered first. Here, only the estimation of AR model parameters, which is a linear estimation problem, is considered. The estimation of MA or ARMA parameters is instead a nonlinear problem and is not considered here. Different methods for solving ARMA model parameters are presented, e.g., in [24].

3.3.1 Yule-Walker method

The problem of estimating AR model parameters is as follows. Given the N observations $x_1, x_2, \ldots, x_N$ the problem is to estimate the unknown parameters $a_1, a_2, \ldots, a_p$. In the Yule-Walker method, also known as the *autocorrelation method* [84], the AR parameters are estimated such that the prediction error variance σ_e^2 is minimized. This is minimized if the prediction error given by (3.18) is

orthogonal to the data, i.e.

$$E\{(x_t + \sum_{j=1}^{p} a_j x_{t-j}) x_{t-k}\} = 0, \quad \forall k = 1, 2, \ldots, p. \tag{3.21}$$

Noting that $E\{x_{t-j}x_{t-k}\} = r_x(k-j)$, the set of equations in (3.21) can be written in matrix form as

$$\underbrace{\begin{pmatrix} r_x(0) & r_x(1) & \cdots & r_x(p-1) \\ r_x(1) & r_x(0) & \cdots & r_x(p-2) \\ \vdots & \vdots & \ddots & \vdots \\ r_x(p-1) & r_x(p-2) & \cdots & r_x(0) \end{pmatrix}}_{R_x} \underbrace{\begin{pmatrix} a_1 \\ a_2 \\ \vdots \\ a_p \end{pmatrix}}_{\theta} = - \underbrace{\begin{pmatrix} r_x(1) \\ r_x(2) \\ \vdots \\ r_x(p) \end{pmatrix}}_{r_x} \tag{3.22}$$

where θ denotes the AR parameter vector. When the biased autocorrelation estimate given in (3.13) is used in (3.22), these equations are called Yule-Walker normal equations. The AR parameter estimates are obtained as

$$\hat{\theta}_{\mathrm{YW}} = -R_x^{-1} r_x. \tag{3.23}$$

For a true AR(p) process x_t the prediction error term $x_t + \sum_{j=1}^{p} a_j x_{t-j}$ is equal to the white noise process e_t and, thus, by setting $k = 0$ in (3.21) it yields $E\{e_t x_t\} = E\{e_t^2\} = \sigma_e^2$ since e_t is uncorrelated with $x_{t-1}, \ldots, x_{t-p}$. Thus, the prediction error variance σ_c^2 can be estimated as

$$\hat{\sigma}_c^2 = E\{(x_t + \sum_{j=1}^{p} a_j x_{t-j}) x_t\} = r_x(0) + \hat{\theta}_{\mathrm{YW}}^T r_x. \tag{3.24}$$

3.3.2 Least squares method

The AR equations, i.e. one step forward prediction equations, for all possible observations x_t are given by

$$x_t = -\sum_{j=1}^{p} a_j x_{t-j} + \epsilon_t, \quad t = p+1, \ldots, N \tag{3.25}$$

where ϵ_t is the prediction error. This set of equations can be written in matrix form as

$$\underbrace{\begin{pmatrix} x_{p+1} \\ x_{p+2} \\ \vdots \\ x_N \end{pmatrix}}_{x} = - \underbrace{\begin{pmatrix} x_p & x_{p-1} & \cdots & x_1 \\ x_{p+1} & x_p & \cdots & x_2 \\ \vdots & \vdots & \ddots & \vdots \\ x_{N-1} & x_{N-2} & \cdots & x_{N-p} \end{pmatrix}}_{H} \underbrace{\begin{pmatrix} a_1 \\ a_2 \\ \vdots \\ a_p \end{pmatrix}}_{\theta} + \underbrace{\begin{pmatrix} \epsilon_{p+1} \\ \epsilon_{p+2} \\ \vdots \\ \epsilon_N \end{pmatrix}}_{\epsilon}. \tag{3.26}$$

In the LS method, the AR parameter estimates are obtained by minimizing the squared prediction error norm $\|\epsilon\|^2$. According to Section 2.3 the LS solution can be written in the form

$$-H^T H\hat{\theta}_{\mathrm{LS}} = H^T x \tag{3.27}$$

and the AR parameter estimates are obtained as

$$\hat{\theta}_{\mathrm{LS}} = -(H^T H)^{-1} H^T x. \tag{3.28}$$

By comparing equations (3.22) and (3.27) it is noticed that they are of the same form, but with different autocorrelation estimates. Roughly speaking it can be said that the autocorrelation functions are connected such that $R_x^{\mathrm{YW}} = \frac{1}{N-p} E\{H^T H\}$ and $r_x^{\mathrm{YW}} = \frac{1}{N-p} E\{H^T x\}$ [110]. Technically, however, in the LS method the same amount of data is averaged for each lag in the autocorrelation estimates, whereas in YW less data is averaged for bigger lags as pointed out by (3.13). Nevertheless, it can be argued that the two methods are asymptotically equivalent.

3.3.3 Modified covariance method

One popular method for estimating AR parameters is the so-called *modified covariance method* [110], which is simply a forward-backward LS estimation procedure. This method can be derived as follows. Corresponding to the forward prediction equations given in (3.25) the backward prediction equations are given by

$$x_t = -\sum_{j=1}^{p} a_j^{\mathrm{b}} x_{t+j} + \epsilon_t^{\mathrm{b}}, \quad t = 1, \ldots, N-p \tag{3.29}$$

where the superscript b stands for backward prediction. These equations can be written in the matrix form

$$x^{\mathrm{b}} = -H_{\mathrm{b}}\theta^{\mathrm{b}} + \epsilon^{\mathrm{b}} \tag{3.30}$$

where $x^{\mathrm{b}} = (x_1, x_2, \ldots, x_{N-p})^T$, $\epsilon^{\mathrm{b}} = (\epsilon_1, \epsilon_2, \ldots, \epsilon_{N-p})^T$, and

$$H_{\mathrm{b}} = \begin{pmatrix} x_2 & x_3 & \cdots & x_{p+1} \\ x_3 & x_4 & \cdots & x_{p+2} \\ \vdots & \vdots & \ddots & \vdots \\ x_{N-p+1} & x_{N-p+2} & \cdots & x_N \end{pmatrix}. \tag{3.31}$$

The minimized quantity is now the sum of the squared prediction error norms $\|\epsilon^{\mathrm{f}}\|^2 + \|\epsilon^{\mathrm{b}}\|^2$, where ϵ^{f} is the forward prediction error term given in (3.26). Due to the symmetry of the autocorrelation, it can be shown that the forward and backward AR coefficients for stationary processes are equal, i.e. $\theta^{\mathrm{f}} = \theta^{\mathrm{b}} = \theta^{\mathrm{fb}}$ [110]. Therefore, the combined forward-backward prediction equations can be written in the matrix form

$$\underbrace{\begin{pmatrix} x^{\mathrm{f}} \\ x^{\mathrm{b}} \end{pmatrix}}_{x^{\mathrm{fb}}} = -\underbrace{\begin{pmatrix} H_{\mathrm{f}} \\ H_{\mathrm{b}} \end{pmatrix}}_{H_{\mathrm{fb}}} \theta^{\mathrm{fb}} + \underbrace{\begin{pmatrix} \epsilon^{\mathrm{f}} \\ \epsilon^{\mathrm{b}} \end{pmatrix}}_{\epsilon^{\mathrm{fb}}}. \tag{3.32}$$

The LS solution for the forward-backward parameter estimation is, thus, given by

$$\hat{\theta}_{\mathrm{LS}}^{\mathrm{fb}} = -(H_{\mathrm{fb}}^T H_{\mathrm{fb}})^{-1} H_{\mathrm{fb}}^T x^{\mathrm{fb}}. \tag{3.33}$$

The estimate for the prediction error variance σ_ϵ^2 in the LS methods is obtained simply as the average of the squared prediction error values. In the forward-backward approach this yields

$$\hat{\sigma}_{\epsilon^{\mathrm{fb}}}^2 = E\{(\epsilon^{\mathrm{fb}})^2\} = \frac{1}{2(N-p)} (\hat{\epsilon}^{\mathrm{fb}})^T \hat{\epsilon}^{\mathrm{fb}} \tag{3.34}$$

where the prediction error term ϵ^{fb} is simply estimated as $\hat{\epsilon}^{\mathrm{fb}} = x^{\mathrm{fb}} + H_{\mathrm{fb}} \hat{\theta}_{\mathrm{LS}}^{\mathrm{fb}}$. In case of accurate estimation, the prediction error terms are sensitive to numerical errors and, therefore, procedures with improved numerical accuracy for solving the prediction error variance have been proposed, see, e.g., [171].

3.4 Model order selection

The central problem in the model order determination is the trade-off between the model fit (i.e. the residual variance) and model complexity (i.e. the number of model parameters). Suppose that an AR model of order p is fitted into a realization of an AR process of finite order. If the order p is smaller than the true model order, the estimated residual variance $\hat{\sigma}_\epsilon^2$ is expected to be larger than the true white noise variance σ_e^2. When p is increased over the true order, on the other hand, the residual variance is not expected to decrease significantly. Thus, the optimal model order could be determined by plotting the estimated residual variance $\hat{\sigma}_\epsilon^2$ as a function of the model order p and selecting the optimal order p from the point where the graph levels off. This method for AR model order determination was proposed in [199].

Various refined versions of the above method have been proposed ever since, see, e.g., the review in [53]. Some of the well-known model order selection criteria are the two developed by Akaike. The first of these being the *final prediction error* (FPE) criterion [3], where the model order p is selected so that the term

$$\mathrm{FPE}(p) = \hat{\sigma}_\epsilon^2 \frac{N+p}{N-p} \tag{3.35}$$

where N is the number of data samples, is minimized [151]. After this, Akaike proposed the *Akaike's information criterion* (AIC) [4] that includes a term of maximized log-likelihood of the model and a term of number of parameters, i.e.

$$\mathrm{AIC}(p) = -2 \max \left\{ \sum_{j=1}^{N} \ln p(x_t | \hat{\theta}) \right\} + 2p. \tag{3.36}$$

For AR processes with Gaussian variables the AIC reduces into the form [84]

$$\mathrm{AIC}(p) = N \ln(\hat{\sigma}_\epsilon^2) + 2p. \tag{3.37}$$

Again the optimal model order p is selected such that AIC(p) is minimized. AIC has also been used for estimating the AR and MA orders p and q of an ARMA model. This is done by simply replacing p with the sum $p+q$ and calculating AIC(p,q) for finite combination of p and q values. Yet another criterion for model order selection is the so-called *minimum description length* (MDL) criterion proposed in [160]. This criterion, resembling the AIC in shape, is given by

$$\mathrm{MDL}(p) = N\ln(\hat{\sigma}_\epsilon^2) + p\ln(N). \tag{3.38}$$

All the previous model order selection criteria are derived for true AR processes and are, therefore, known to work well for simulated AR processes. Actual measured biosignals are, however, hardly AR processes. In this case, the model bias increases the residual variance and, therefore, affects on the model order selection criteria. In other words, the suitability of the model order selection criteria depends on how well the signal is modeled by an AR process. Thus, the model order selection criteria can only be used as guidelines for the model order in real applications.

3.5 Spectrum estimation

Additional information about the process of interest can be achieved by presenting the process in frequency-domain using the power spectrum representation of the process. According to (3.14) the PSD is defined as the Fourier transform of the autocorrelation sequence. The true autocorrelation sequence is not usually known and, thus, the spectrum must be estimated. Methods for estimating PSD can be divided into classical (nonparametric) and parametric methods. The classical PSD estimators are based on the Fourier transform which for finite discrete-time processes is usually calculated using the *fast Fourier transform* (FFT). In the parametric methods, on the other hand, the observed process is modeled with some parametric model (e.g. AR or ARMA) and the PSD is obtained from the estimated model parameters.

3.5.1 Fourier transform

The *continuous Fourier transform* (CFT) of function $x(t)$ can be defined as

$$X(f) = \int_{-\infty}^{\infty} x(t)e^{-i2\pi ft}\,dt \tag{3.39}$$

where i is the imaginary unit and f is frequency. The function $X(f)$ is a complex function and can, thus, be presented in the form

$$X(f) = |X(f)|e^{i\Phi(f)} = A(f)e^{i\Phi(f)} \tag{3.40}$$

where $A(f)$ is the amplitude spectrum and $\Phi(f)$ the phase spectrum of $x(t)$. The power spectrum is the square of the amplitude spectrum, that is $P(f) = X(f)X^*(f) = |X(f)|^2$, where the superscript $(\cdot)^*$ denotes the complex conjugate operation. The analogy between $x(t)$ and $X(f)$ is denoted shortly as

$x(t) \longleftrightarrow X(f)$. One important property of Fourier transform is that convolution in time-domain corresponds to multiplication in frequency-domain, i.e.

$$x(t) * y(t) \longleftrightarrow X(f)Y(f) \tag{3.41}$$

which is known as *convolution theorem* and applies also the other way around.

Let x_t be a discrete-time sequence sampled from $x(t)$ at $f_s = 1/\Delta T$ Hz, where ΔT is the sampling interval. Clearly, the sampled sequence x_t can be represented as $x_t = \sum_{j=-\infty}^{\infty} x(j\Delta T)\delta(t - j\Delta T)$ and the Fourier transform of x_t yields

$$X(f) = \sum_{j=-\infty}^{\infty} x_j e^{-i2\pi jf/f_s} \tag{3.42}$$

where $x_j = x(j\Delta T)$. It turns out that (3.42) is a periodic replication of (3.39) with period f_s. In general, sampling in time-domain results in periodicity in frequency-domain and vice versa. Therefore, to avoid the overlapping of the spectrum periods (*frequency aliasing*) the continuous signal $x(t)$ must be bandlimited with maximum frequency $f_{\max}$, i.e. the transform of $x(t)$ is zero for all $f > f_{\max}$, and the sampling frequency must satisfy $f_s \geq 2f_{\max}$, where $2f_{\max}$ is known as the *Nyquist frequency.*

If only a finite data sequence of N points is observed the transform (3.42) reduces to

$$X(f) = \sum_{j=0}^{N-1} x_j e^{-i2\pi jf/f_s} \tag{3.43}$$

which can be considered as the transform of the infinite sequence x_t windowed with a N-point rectangular window. This is still a continuous function of frequency. Evaluation of the previous equation in discrete frequencies $f_k = k\, f_s/N$, $k = 0, 1, \ldots, N-1$ yields

$$X_{\mathrm{DFT}}(f_k) = \sum_{j=0}^{N-1} x_j e^{-i2\pi jk/N} \tag{3.44}$$

which is called the *discrete Fourier transform* (DFT) of sequence x_t. Since the sampling in the frequency-domain results in periodicity in time-domain, the DFT should actually be considered as the transform of a periodic extension of x_t windowed with a rectangular window. The length of the window being equal to the length of the period. Efficient algorithms that evaluate the DFT equation (3.44) are, in general, called FFT algorithms.

3.5.2 Classical spectral estimation

The classical PSD estimators are divided into indirect and direct approaches. In the indirect approach the PSD is obtained as the transform of the autocorrelation sequence, whereas in the direct approach PSD is obtained by taking the transform of the process directly. Collectively, the indirect approaches are called *correlograms*

and direct approaches *periodograms*. Only the latter approaches are considered here. The periodogram PSD estimate for the observed sequence x_l is defined as

$$P_x(f_k) = \frac{1}{Nf_s}\left|\sum_{j=0}^{N-1} x_j e^{-i2\pi jk/N}\right|^2 \tag{3.45}$$

where the scaling term Nf_s is required for proper power determination [110]. The periodogram can be shown to be an asymptotically unbiased estimate of PSD, but it is not consistent because the standard deviation (square root of variance) of periodogram for any frequency is approximately equal to the power density value to be estimated and does not depend on N [84]. The variance of periodogram can, however, be reduced by averaging periodograms calculated from shorter epochs of the data sequence. The spectral resolution of the periodogram, on the other hand, is roughly the reciprocal of the length of the observed sequence, that is $\sim f_s/N$. This leads to the fundamental trade-off in periodogram spectrum estimation, namely between the frequency resolution and the estimate variance. Another important issue in periodogram estimators is the effect of windowing which will be discussed next.

Effect of windowing

It is recalled, that in discrete Fourier transform the observed data sequence was considered as a multiplication of its periodic extension with a rectangular window. In the frequency-domain, this corresponds to convolution of the transform of the periodic extension and the transform of the window. The Fourier transform of a rectangular window is known to be a sinc-function and, thus, the DFT is implicitly convolved with sinc-function. This phenomenon is known as *spectral leakage* to sidelobes and it tends to broaden the spectral peaks and can also cover weaker spectral components. The effect of windowing for a short sinusoid is presented in Fig. 3.1, where the DFT magnitude of a 32-point sinusoid is presented along with the DFT magnitude of 32-point rectangular window. The relative frequency of the sinusoid is 0.1.

Various window functions have been derived to decrease the spectral leakage produced by the rectangular window. These include, e.g., triangular, Hanning, Hamming, and Gaussian windows. Each window function has characteristic mainlobe widths (the DFT hump at zero frequency) and sidelobe levels. Rectangular window has the narrowest mainlobe and, thus, the best frequency resolution of all windows. However, other window functions have lower sidelobe levels and are, therefore, used to reduce spectral leakage. The selection of the window function is, thus, a trade-off between spectral resolution and sidelobe level.

Periodogram modifications

Several modifications of the periodogram PSD estimate (3.45) have been developed [110]. The reason for these modifications is to reduce the variance of the periodogram by means of averaging. In *Daniell's modification* the periodogram is

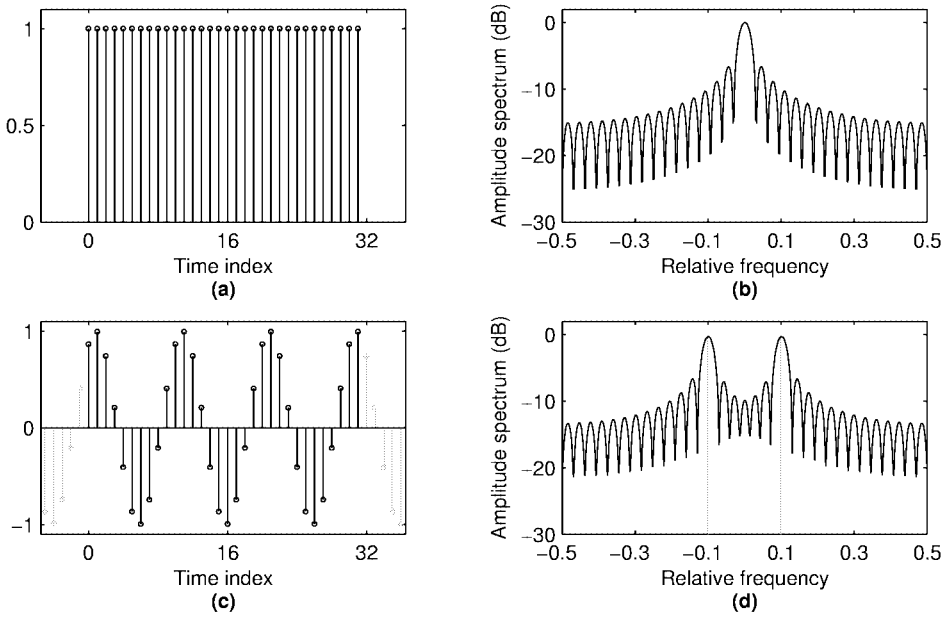

Figure 3.1: The influence of spectral leakage on the DFT of a sampled sinusoid. (a) A 32-point rectangular window and (b) its DFT magnitude. (c) A 32-point sinusoid and (d) its DFT magnitude.

smoothed by averaging over adjacent frequency bins. The evident generalization of this modification is simply to low-pass filter the periodogram. In *Bartlett periodogram*, on the other hand, the observed sequence of N points is divided into nonoverlapping shorter segments of D points and a periodogram is calculated for each segment. The Bartlett periodogram is then obtained by averaging the segment periodograms. The Bartlett periodogram was further modified by Welch. In *Welch's modification*, a window function is applied to the data in each segment to reduce spectral leakage and the segments are allowed to overlap. The purpose of overlapping segments is to increase the number of segments and, thus, to decrease the spectrum estimate variance further. The Welch's periodogram is obtained as

$$P_{\text{Welch}}(f_k) = \frac{1}{M}\sum_{m=1}^{M}\left(\frac{1}{NF_sU}\left|\sum_{j=0}^{D-1} w_j x_j^{(m)} e^{-i2\pi jk/D}\right|^2\right) \tag{3.46}$$

where $w = (w_0, \ldots, w_{D-1})$ is the discrete window function, $x_j^{(m)}$ is the m'th data segment, M is the number of segments, and

$$U = \frac{1}{f_s} \sum_{j=0}^{D} w_j^2 \tag{3.47}$$

is the window energy. The scale factor U removes the energy bias caused by windowing.

3.5.3 Parametric spectral estimation

In the classical spectral estimation methods, the Fourier transform of the observed sequence or its autocorrelation yielded the PSD estimate. Next, parametric spectral estimation methods, where the observed sequence is first modeled as an output of a linear filter with a white noise input (i.e. a time series model) and then the PSD estimate is obtained from the estimated filter coefficients. It is assumed here that the reader is familiar with the basics of signal analysis and filter theory. For example, the so-called z-transform is not defined here. If this is not the case, the reader is referred to see, e.g., [134, 110].

Here, the parametric ARMA spectrum estimation is considered. The ARMA(p,q) model can be presented as

$$\sum_{j=0}^{p} a_j x_{t-j} = \sum_{k=0}^{q} b_k e_{t-k} \tag{3.48}$$

where $a_0 = 1$ and, in addition, the usual assumption $b_0 = 1$ is adopted. By taking the z transforms from both sides this yields

$$X(z)A(z) = E(z)B(z) \tag{3.49}$$

where $X(z)$ is the z-transform of sequence x_t, $E(z)$ is the transform of white noise process e_t, and $A(z) = 1 + \sum_{j=1}^{p} a_j z^{-j}$ and $B(z) = 1 + \sum_{k=1}^{q} b_k z^{-k}$ are the transforms of the AR and MA polynomials. Considering x_t as an output of a linear filter for the white noise input e_t the system function $H(z)$ relating input and output transforms as $X(z) = H(z)E(z)$ is

$$H(z) = \frac{B(z)}{A(z)} = \frac{1 + \sum_{k=1}^{q} b_k z^{-k}}{1 + \sum_{j=1}^{p} a_j z^{-j}} \tag{3.50}$$

which can also be written in the equivalent factored form

$$H(z) = \frac{\Pi_{k=1}^{q}(z - \beta_k)}{\Pi_{j=1}^{p}(z - \alpha_j)} \tag{3.51}$$

where β_k are the roots of the numerator polynomial, also called the zeros of $H(z)$, and α_j are the roots of the denominator polynomial, also called the poles of $H(z)$. For a stable system the roots must lie inside the unit circle, i.e. $|\alpha_k| < 1$ for all k.

Furthermore, it can be shown that the z-transform of the autocorrelation of x_t is related to the transform of the input autocorrelation by [110]

$$P_x(z) = H(z)H(1/z)P_e(z) = \frac{B(z)B(1/z)}{A(z)A(1/z)}P_e(z) \tag{3.52}$$

where $P_e(z) = \sigma_e^2$. The PSD of the ARMA process x_t is obtained by substituting $z = e^{i2\pi f/f_s}$ and scaling with the sampling frequency f_s. This yields

$$P_{\mathrm{ARMA}}(f) = \sigma_e^2/f_s \frac{|1 + \sum_{k=1}^{q} b_k e^{-i2\pi kf/f_s}|^2}{|1 + \sum_{j=1}^{p} a_j e^{-i2\pi jf/f_s}|^2} \tag{3.53}$$

which becomes an PSD estimate when the estimated model parameters $\hat{a}_j$ and $\hat{b}_k$ and prediction error variance $\hat{\sigma}_\epsilon^2$ are substituted. The PSD estimates for pure AR or MA processes are obtained by setting $b_k = 0$ for all $k = 1, \ldots, q$ or $a_j = 0$ for all $j = 1, \ldots, p$ respectively.

Besides the method used in the parameter estimation, the quality of the parametric PSD estimate mainly depends on the used model, i.e. the general model structure and model order. The selection of the model structure is often based on common practice and ease of implementation. The benefit of ARMA model is that it can represent diverse spectral shapes with substantially lower model orders. The selection of the model order was already discussed in Section 3.4 and can be accomplished using some of the criteria presented there. In addition, prior knowledge on the spectral content of the observation can be used in model order selection. Since each pair of complex roots of the AR polynomial produce a peak into the spectrum, it is obvious that a smaller AR model order will result in a smoother spectrum estimate and the selection of too high a model order can produce spurious peaks in the spectrum. In any case, the order of the AR part should be at least twice the number of expected peaks in the spectrum.

Note that equation (3.53) is a continuous function of frequency f and can, therefore, be evaluated at any desired frequencies up to the Nyquist frequency $f_s/2$. The frequency resolution is naturally not, however, infinite, but is determined by the underlying model. When compared to classical PSD estimation methods, the resolution of parametric PSD estimators is higher due to the implicit extrapolation of the autocorrelation sequence [110].

Spectral decomposition

One property of the parametric spectrum estimation methods, that has been found advantageous in many applications, is that the spectrum can be divided into separate components [208]. Consider a pole α_j of an AR(p) model positioned at frequency f_j. The spectrum of this single component in the vicinity of f_j can be estimated as

$$P_j(f) \approx \frac{c_j}{(z - \alpha_j)(1/z - \alpha_j^*)}, \quad z = e^{i2\pi f/f_s} \tag{3.54}$$

where the constant c_j is given by

$$c_j \approx \frac{\sigma_e^2/f_s}{\Pi_{k\neq j}(z-\alpha_k)(1/z-\alpha_k^*)}, \quad z = e^{i2\pi f_j/f_s}. \tag{3.55}$$

That is, the part c_j of the AR spectrum estimate is assumed to be constant when $f \approx f_j$. The sum of the component spectra should be approximately equal to the AR spectrum estimate, i.e. $P_{\mathrm{AR}}(f) \approx \sum_{j=1}^{p} P_j(f)$.

The powers of the components can be estimated using the method proposed in [72]. According to this, the power of the component positioned at frequency f_j can be estimated with the residue

$$P_{f_j} = d\,\mathrm{Re}\left\{\mathrm{Res}\left\{\frac{P_{\mathrm{AR}}(z)}{z}\right\}\Big|_{z=e^{i2\pi f_j/f_s}}\right\} \tag{3.56}$$

where the residue is evaluated at $z = e^{i2\pi f_j/f_s}$ and the coefficient $d = 1$ for real poles and $d = 2$ for complex poles. The previous equation can be solved by evaluating

$$P_{f_j} = d\,\mathrm{Re}\left\{\frac{\sigma_e^2(z-\alpha_j)}{zA(z)A(1/z)}\right\} \tag{3.57}$$

where $A(z) = \Pi_{k=1}^{p}(1-\alpha_k z^{-1})$, at $z = \alpha_j$ [110]. This method for component power estimation works for well-separated poles, but for poles close to each other power estimates can yield negative values.

3.6 Cross spectrum and coherence

The cross power spectrum $P_{xy}(f)$ of sequences x_t and y_t is defined as the Fourier transform of the cross correlation function $r_{xy}(\tau)$. The cross spectrum describes the correlation of the two sequences in the frequency-domain. A concept closely related to cross spectrum is that of coherence. The coherence function is defined as

$$\mathrm{Coh}_{xy}(f) = \frac{P_{xy}(f)}{\sqrt{P_x(f)}\sqrt{P_y(f)}}. \tag{3.58}$$

The squared magnitude of this, i.e. $|\mathrm{Coh}_{xy}(f)|^2$, is often used as a measure of similarity between the two sequences as a function of frequency. This is because $|\mathrm{Coh}_{xy}(f)|^2$ returns 0 for frequencies where there is no correlation and 1 for frequencies where sequences are perfectly correlated. The coherence phase spectrum is given as

$$\Phi_{xy}(f) = \tan^{-1}(\mathrm{Im}\{\mathrm{Coh}_{xy}(f)\}/\mathrm{Re}\{\mathrm{Coh}_{xy}(f)\}) \tag{3.59}$$

which represents the phase difference between the two sequences as a function of frequency.

Using the classical spectrum estimation methods presented in Section 3.5.2 the coherence function can be calculated by substituting the spectra $P_x(f)$, $P_y(f)$, and $P_{xy}(f)$ with the corresponding averaged periodograms. That is, sequences x_t and y_t are divided into shorter segments and periodogram estimates are calculated for

each segment. Periodogram estimates $P_x(f)$ and $P_y(f)$ are given by (3.45) and the cross spectrum periodogram estimate is given by

$$P_{xy}(f_k) = \frac{1}{Nf_s} X_{\mathrm{DFT}}(f_k) Y^*_{\mathrm{DFT}}(f_k). \tag{3.60}$$

The averaging over segments reduces both the variance of the periodogram estimates and the bias in the coherence estimate. In the extreme case when the periodograms are calculated without segment averaging the coherence function is clearly $\mathrm{Coh}_{xy}(f) = 1$, i.e. a constant independent of data. This points out the extreme effect of bias in the coherence function.

The coherence function can also be evaluated using the parametric spectral estimation techniques presented in Section 3.5.3. To do this, the parameter model needs to be redefined in vectorized form, see, e.g., [110]. This is not, however, in the scope of this thesis and will not be presented here.

CHAPTER IV

Time-varying time series models

In the previous chapter, stationary time series modeling was concerned. The observation was considered to be an output of a linear time-invariant system which could be described by a finite set of constant variables. Next, it is assumed that the underlying system is time-varying and an observation of the system output at time t is denoted as x_t. The resulting sequence of observations x_t will be nonstationary and it must be modeled as an output of a time-varying or dynamic model. The time-varying autoregressive moving average ARMA(p,q) model can be written in the form

$$x_t = -\sum_{j=1}^{p} a_t^{(j)} x_{t-j} + \sum_{k=1}^{q} b_t^{(k)} e_{t-k} + e_t \tag{4.1}$$

where $a_t^{(j)}$ is the value of the j'th AR parameter at time t and $b_t^{(k)}$ the value of the k'th MA parameter at time t. In this chapter, some popular adaptive algorithms for estimating the time-varying parameters of model (4.1) are presented. Time-varying AR or MA models are not considered separately, since the revision of the results for these models is straightforward. At the end of the chapter, time-varying spectrum estimation methods, including the popular short-time Fourier transform and wavelet transform time-frequency representations, are discussed. The main references for this chapter are [5, 60, 63, 81, 167].

4.1 Time-dependent parameter estimation

Let x_t be an output of the time-varying ARMA(p,q) model given in (4.1). The problem is then to estimate the $p+q$ unknown parameters $a_t^{(1)}, \ldots, a_t^{(p)}$ and $b_t^{(1)}, \ldots, b_t^{(q)}$ for each time instant t. This is clearly a highly undeterministic problem, but it can be solved recursively with the Kalman filter algorithm derived in Section 2.9. The Kalman filter is based on state-space formalism.

4.1.1 Kalman filtering

To utilize the Kalman filter algorithm, the state-space model for the observations need to be established. To do this, the time-varying ARMA(p,q) model given in

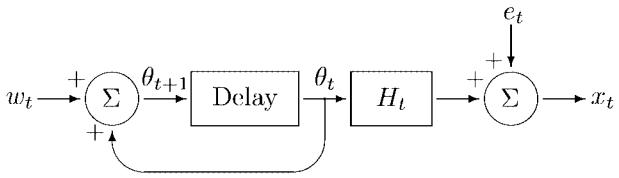

Figure 4.1: Structure of the state-space signal model.

(4.1) is written in vector form by denoting the AR and MA parameters at time t as

$$\theta_t = (-a_t^{(1)}, \ldots, -a_t^{(p)}, b_t^{(1)}, \ldots, b_t^{(q)})^T \tag{4.2}$$

and the sequences of the past observations and noise terms as

$$H_t = (x_{t-1}, \ldots, x_{t-p}, e_{t-1}, \ldots, e_{t-q}). \tag{4.3}$$

Using the above notations the time-varying ARMA(p,q) model can be written in the form

$$x_t = H_t\theta_t + e_t \tag{4.4}$$

which is formally a linear observation model with H_t being the regression vector and e_t the observation error. Note that the sequence $e_{t-1}, \ldots, e_{t-q}$ in the regression vector is not measured unlike x_t, but it has to be estimated together with other parameters. The evolution of the state θ_t when no prior information is available is typically described with the *random walk model* [60] yielding a state equation of the form

$$\theta_{t+1} = \theta_t + w_t. \tag{4.5}$$

Equations (4.4) and (4.5) form the state-space signal model for the time-varying ARMA process x_t. The structure of this signal model is presented in Fig. 4.1.

The Kalman filter solution for the state θ_t, i.e. for parameters $a_t^{(j)}$ and $b_t^{(k)}$, can now be written as in Section 2.9. By comparing the state equations (2.55) and (4.5) it is, however, noted that now $F_t \equiv I$ and $G_t \equiv I$. Thus, the Kalman filter equations reduce to

$$\begin{aligned}
C_{\tilde{\theta}_{t|t-1}} &= C_{\tilde{\theta}_{t-1}} + C_{w_{t-1}} && (4.6)\\
K_t &= C_{\tilde{\theta}_{t|t-1}} H_t^T (H_t C_{\tilde{\theta}_{t|t-1}} H_t^T + C_{e_t})^{-1} && (4.7)\\
\epsilon_t &= x_t - H_t\hat{\theta}_{t-1} && (4.8)\\
\hat{\theta}_t &= \hat{\theta}_{t-1} + K_t\epsilon_t && (4.9)\\
C_{\tilde{\theta}_t} &= (I - K_t H_t) C_{\tilde{\theta}_{t|t-1}}. && (4.10)
\end{aligned}$$

Note that the unknown observation noise term e_t is estimated as the one step prediction error ϵ_t of the observation x_t in every step of the iteration.

To operate the Kalman filter algorithm in practice, both the initial values for the state and the error covariance and the noise covariances C_{w_t} and C_{e_t} need to be specified. In practice, the distribution of the initial state θ_0 is rarely known and, therefore, the initial values $\hat{\theta}_0$ and $C_{\tilde{\theta}_0}$ are usually determined by some conventional means. A common approach for the initialization is to set the initial state, e.g., for $\hat{\theta}_0 = 0$ and the error covariance, e.g., for $C_{\tilde{\theta}_0} = I$ and then to run a short segment from the beginning of data backwards in time. The values obtained for the state and error covariance in the backward run are then used as initial values in the forward run. This kind of initialization is not, however, needed if sufficient amount of data before the point of interest is available.

The state noise covariance C_{w_t} is the term that determines the adaptation (i.e. the speed of change of the state) of the Kalman filter. In [67], it was assumed that $C_{w_t} = \sigma_w^2 I$ and $C_{e_t} = \sigma_e^2 = 1$, where σ_w^2 is the state noise covariance coefficient and σ_e^2 the observation noise covariance coefficient. In this case, the adaptation of the filter can be adjusted with a single coefficient. The bigger the value of σ_w^2 the quicker the adaptation. The variance of the state estimates is, however, inversely proportional to the value of σ_w^2 and, therefore, σ_w^2 should be specified in such a way that a desired balance between the filter adaptation and estimate variance is obtained. The above selections for the covariances seems reasonable since the parameter estimates only depend on the ratio σ_w^2/σ_e^2. Another approach is to adjust the covariances iteratively [70, 31]. An extensive review of Kalman filtering with different choices for C_{w_t} and C_{e_t} can be found in [167]. In this thesis, the assumptions $C_{w_t} = \sigma_w^2 I$ and $C_{e_t} = 1$, which were found to be favorable in [167], are adopted.

4.1.2 Fixed-interval smoothing

The fixed-interval smoothing equations were derived in Section 2.10. The fixed-interval smoothing is an off-line procedure and it assumes that the Kalman filter state estimates and the error covariances are known for each time t. Fixed-interval smoothed estimates $\hat{\theta}_{t|N}$ for state θ_t and $C_{\tilde{\theta}_{t|N}}$ for error covariance are then given by running the Kalman filter estimates backwards in time by taking $t = N-1, N-2, \ldots, 1$. The smoothing equations can be summarized as

$$\hat{\theta}_{t|N} = \hat{\theta}_t + A_t(\hat{\theta}_{t+1|N} - \hat{\theta}_t) \tag{4.11}$$

$$C_{\tilde{\theta}_{t|N}} = C_{\tilde{\theta}_t} + A_t(C_{\tilde{\theta}_{t+1|N}} - C_{\tilde{\theta}_{t+1|t}})A_t^T \tag{4.12}$$

$$A_t = C_{\tilde{\theta}_t} C^{-1}_{\tilde{\theta}_{t+1|t}} \tag{4.13}$$

where the filtered estimate $\hat{\theta}_N$ is used for the initialization, that is $\hat{\theta}_{N|N} = \hat{\theta}_N$. Note that the operation of the smoother does not require any additional specifications, but the ones made for Kalman filter algorithm act on the smoothed estimates as well. An estimator consisting of the Kalman filter algorithm along with smoothing equations is in general called Kalman smoother. In this thesis, this term refers in particular to fixed-interval smoothed Kalman filtering.

4.1.3 LMS and RLS algorithms

Parallel to the Kalman filter, several other recursive algorithms have been proposed, see, e.g., [60, 167]. In biosignal applications the most popular such algorithms are the *least mean square* (LMS) and *recursive least squares* (RLS) algorithms. The LMS algorithm is often considered as a standard against other recursive algorithms, mainly because of its simplicity. The RLS algorithm is computationally more complex, but its convergence is typically an order of magnitude faster than that of LMS algorithm.

LMS ALGORITHM

The LMS algorithm was proposed in [200]. It is a gradient based adaptive algorithm closely related to the steepest descent algorithm. In the gradient based algorithms the state estimate is updated in the direction of the negative gradient of the mean square error, that is

$$\hat{\theta}_t = \hat{\theta}_{t-1} + \frac{1}{2}\mu\left(-\frac{\partial E\{e_{t-1}^2\}}{\partial \theta_{t-1}}\right) \tag{4.14}$$

where μ is a positive constant, a step size parameter. In the LMS algorithm the gradient is approximated by differentiating the prediction error term $\epsilon_t = x_t - H_t\hat{\theta}_{t-1}$ [60]. The partial derivative of ϵ_t^2 with respect to $\hat{\theta}_{t-1}$ is $-2H_t^T x_t + 2H_t^T H_t\hat{\theta}_{t-1}$. Substituting this into (4.14) yields the LMS algorithm, which is of the form

$$\hat{\theta}_t = \hat{\theta}_{t-1} + \mu H_t^T(x_t - H_t\hat{\theta}_{t-1}) \tag{4.15}$$

where the step size parameter μ controls the convergence of the algorithm. A small value of μ results in slow adaptation while a larger value gives faster adaptation but with the expense of estimate stability. The details of the convergence of the LMS algorithm have been extensively discussed, e.g., in [60], where a simplified condition, stipulating that the adaptation parameter μ must satisfy

$$0 < \mu < \frac{2}{H_t H_t^T} \tag{4.16}$$

at every step of iteration, for the convergence of LMS was given. The term $H_t H_t^T$ in (4.16) represents the total input power at time t. This condition can be implemented into the algorithm by adjusting μ iteratively as $\mu_t = c/(H_t H_t^T)$, where c is a constant smaller than 2.

RLS ALGORITHM

The RLS algorithm is a method for solving the least squares estimate for state θ_t at time t by updating the previous state estimate. The estimation criterion in RLS algorithm is, thus, to minimize the LS functional. In order to improve the

adaptation of the algorithm the ordinary LS functional (2.21) need to be replaced with the weighted LS functional

$$l(\theta_t) = \sum_{j=1}^{t} \lambda^{t-j} e_j^2 \tag{4.17}$$

where λ is called the *forgetting factor* which must satisfy $0 < \lambda \leq 1$. The RLS algorithm could be derived by differentiating the above functional with respect to θ_t. The resulting algorithm can be summarized as [60]

$$\hat{\theta}_t = \hat{\theta}_{t-1} + K_t(x_t - H_t\hat{\theta}_{t-1}) \tag{4.18}$$

where

$$K_t = \frac{P_{t-1}H_t^T}{H_t P_{t-1} H_t^T + \lambda} \tag{4.19}$$

$$P_t = \lambda^{-1}(I - K_t H_t)P_{t-1}. \tag{4.20}$$

The adaptation speed of the RLS is controlled with the forgetting factor λ. This is clearly seen from the functional (4.17). For smaller values of λ more weight is given to the recent error terms than the first terms and, thus, the algorithm adapts faster to changes. If $\lambda = 1$ the solution returns to the regular LS solution. In practice the forgetting factor is typically chosen between $0.9 \leq \lambda \leq 1$.

Connections to Kalman filter

The Kalman filter equations given in (4.6) (4.10) can be written in simplified form by denoting $P_t = C_{\tilde{\theta}_t} + C_{w_t}$ and substituting (4.6) into (4.7)–(4.10). This yields

$$\hat{\theta}_t = \hat{\theta}_{t-1} + K_t(x_t - H_t\hat{\theta}_{t-1}) \tag{4.21}$$

where

$$K_t = \frac{P_{t-1}H_t^T}{H_t P_{t-1} H_t^T + C_{e_t}} \tag{4.22}$$

$$P_t = (I - K_t H_t)P_{t-1} + C_{w_t}. \tag{4.23}$$

Thus, the RLS and Kalman filter algorithms differ only on the form of the gain vector K_t. In fact, it can be shown that with a specific choices of C_{e_t} and C_{w_t} the Kalman filter gives the RLS algorithm [102, 60, 81]. Furthermore, it turns out that also the LMS algorithm can be derived from the Kalman filter equations with specific choices for C_{e_t}, C_{w_t}, and P_0 [81]. Finally, it can be summarized that all three algorithms can be presented in the form (4.21) with different choices of gain K_t. For the LMS algorithm the gain K_t is clearly of the form $K_t = \mu H_t^T$.

4.2 Model order selection

The selection of the model order in the time-varying case is not as straightforward as in the stationary case, where simple criteria such as FPE and AIC for selecting the model order were given (see Section 3.4). Some approaches for estimating the model order in nonstationary case can be found, e.g., in [50, 59]. For example, in [50], a modified AIC was used for estimating the order of the AR model along with the model parameters iteratively. In practice, however, the model order is usually fixed according to some prior knowledge or known guidelines. A fixed value for the model order can also be roughly estimated by using some of the criteria from the stationary case.

4.3 Time-varying spectrum estimation

The definition of the power spectral density given in (3.14) is valid only for stationary processes. The real life processes are, however, rarely stationary, but their properties change in time. One traditional approach to manage nonstationary processes is to transform them into stationary form by removing specific trend components from the processes. This approach is basically useful for processes with time-varying mean, but it is inadequate when higher order nonstationarities are included. In the latter case, time-varying spectrum estimation methods are required. For this, several time-frequency representation methods have been proposed. A traditional TFR method is the STFT, which is also known as the *spectrogram*. Another common TFR method that is shortly discussed here is the wavelet transform. In addition to these two linear TFRs, various quadratic TFRs such as the *Wigner distribution* and its numerous smoothed versions have been proposed. For good tutorials on TFR methods, see, e.g., [26, 63, 5]. An alternative approach is to use parametric time-varying spectrum estimation methods discussed in Section 4.3.2.

4.3.1 Time-frequency representations

A TFR describes the energy density of the observed process simultaneously in time and frequency. TFR methods can be divided into linear and quadratic methods based on how they depend on the observation x_t [63]. Both the STFT and WT methods presented here are linear TFRs.

Short-time Fourier transform

The STFT consists simply of local spectra of the observation at different times. In the STFT the spectrum at time t is estimated by taking the Fourier transform of the observed process x_t multiplied with an analysis window w_t centered at time t and the time-variation is obtained by sliding the analysis window over the whole observation. For the discrete-time process x_t of N points the STFT is defined as

$$X_{\mathrm{STFT}}(t, f_k) = \sum_{j=0}^{N-1} x_j w_{j-t} e^{-i2\pi jk/N}, \quad f_k = kf_s/N \tag{4.24}$$

where the analysis window is such that $w_{j-t} > 0$ for $|j-t| < D/2$ and $w(j-t) = 0$ otherwise. The value $D \ll N$ is the effective length of the analysis window. The time-varying power spectrum or PSD estimate is then given as the squared magnitude of the STFT with proper power scaling, i.e.

$$P_{\text{STFT}}(t, f_k) = \frac{1}{N f_s U} |X_{\text{STFT}}(t, f_k)|^2 \tag{4.25}$$

where U is the energy of the analysis window given by (3.47). The TFR given by the above equation is also commonly known as the spectrogram.

The time-frequency resolution of the spectrogram depends on the length D of the analysis window. The frequency resolution is inversely proportional to the window length according to $\Delta f = f_s/D$, whereas the time resolution behaves vice versa. That is, an improvement in the time resolution is obtained by shortening the analysis window. Thus, it is impossible to accomplish arbitrarily good resolution in both time and frequency, but a trade-off must be committed. It should also be noted that the observation is assumed to be stationary within each windowed segment which might not be true for signals which include short-term nonstationarities even when rather short window is used. Besides the length, also the form of the analysis window need to be specified. This can be done as in the stationary case (see Section 3.5.2).

The STFT given in (4.24) has another useful interpretation as follows. Multiplying the STFT by $e^{i2\pi tk/N}$ in both sides yields

$$\begin{aligned} X_{\text{STFT}}(t, f_k) &= e^{-i2\pi tk/N} \sum_{j=0}^{N-1} x_j w_{j-t} e^{i2\pi(t-j)k/N} && (4.26) \\ &= e^{-i2\pi tk/N} (x_t * w_t e^{i2\pi tk/N}) && (4.27) \end{aligned}$$

where w_t is assumed to be symmetric. From the above presentation it is observed that STFT can also be interpreted as filtering the observation with a causal filter with impulse response

$$h_t = w_t e^{i2\pi tk/N} \tag{4.28}$$

and multiplying the filter output with phase shift factor $e^{-i2\pi tk/N}$. In frequency-domain this filtering corresponds to windowing the observation spectrum with the window transform centered at frequency f_k, i.e.

$$x_t * w_t e^{i2\pi tk/N} \leftrightarrow X(f) W(f - f_k). \tag{4.29}$$

In other words, STFT can be interpreted as filtering the observation x_t with a band-pass filter having constant band-width for all frequencies f_k.

Wavelet transform

The WT is a fairly new TFR method, originally introduced as a time-scale method [159, 158, 191]. The WT has a clear interpretational connection to STFT. That is, the WT can also be interpreted as filtering the observed process with a band-pass

filter centered at specific frequency. The fundamental difference to STFT is that in WT the band-width of the filter is proportional to frequency. The WT has also been termed as a *constant-Q transform* since the filter quality factor Q defined as the ratio of the center frequency and band-width is constant [159]. Thus, the WT results in improved time-resolution but decreased frequency resolution for higher frequencies and vice versa for lower frequencies.

The *continuous wavelet transform* (CWT) is defined as

$$X_{\mathrm{CWT}}(\tau, \mathfrak{a}) = \int x(t) h^*_{\mathfrak{a},\tau}(t)\, dt = \frac{1}{\sqrt{\mathfrak{a}}} \int x(t) h^*\left(\frac{t-\tau}{\mathfrak{a}}\right) dt \tag{4.30}$$

where $h_{\mathfrak{a},\tau}(t)$ is the prototype wavelet localized in time, $\mathfrak{a}$ is a scale parameter, and τ a shifting factor. Thus, the wavelet basis is obtained by scaling and shifting in time the single wavelet prototype $h_{\mathfrak{a},\tau}(t)$. For large values of $\mathfrak{a}$ the wavelet is a stretched low frequency version of the prototype and for small values of $\mathfrak{a}$ a contracted high frequency version is obtained. If compared to STFT given above, it is noted that in STFT the "analyzing wavelet" is a modulated version of the analysis window.

The CWT can also be seen as an orthonormal basis decomposition and, furthermore, it preserves energy [159]. Therefore, the CWT can be used to define a TFR which can be considered as a modified version of the spectrogram. The frequency scale for the WT is obtained by substituting $\mathfrak{a} = f_0/f$, where f_0 is the center frequency of the wavelet [158]. The wavelet PSD estimate, known as the *scalogram*, is obtained as the squared magnitude of the CWT

$$P_{\mathrm{CWT}}(\tau, f) = |X_{\mathrm{CWT}}(\tau, f)|^2. \tag{4.31}$$

In the discrete time case, the scale factor $\mathfrak{a}$ and time shift τ are discretized. In the discretization corresponding to a dyadic time-frequency grid, this is done by setting $\mathfrak{a} = 2^m$ and $\tau = n2^m\Delta T$, where ΔT is the sampling interval of the discrete signal and m and n are integers [191]. The discretized wavelet prototype can be written in the form

$$h_{m,n}(t) = 2^{-m/2} h(2^{-m}t - n\Delta T). \tag{4.32}$$

The fundamental decision in wavelet analysis is how to select the wavelet prototype. Numerous such prototypes have been proposed. One such prototype, that has been applied in Section 6.5.2 for estimating the TFR of an event-related EEG sample (see Fig. 6.9), is the modulated Gaussian function known as *Morlet wavelet* which is of the form

$$h(t) = e^{-\frac{1}{2}t^2 + i\omega_0 t} \tag{4.33}$$

where $\omega_0 = 5.33$.

4.3.2 Parametric time-varying spectrum estimation

Consider next that the process x_t is a time-varying ARMA(p,q) process satisfying the difference equations given in (4.1). That is, x_t is an output of a linear time-varying filter with white noise input. Then, the spectral density of x_t at time

t is given according to the stationary case (3.53) from the momentary system coefficients as

$$P_{\mathrm{ARMA}}(t,f) = \sigma_e^2(t)/f_s \frac{|1+\sum_{k=1}^{q} b_t^{(k)} e^{-i2\pi kf/f_s}|^2}{|1+\sum_{j=1}^{p} a_t^{(j)} e^{-i2\pi jf/f_s}|^2} \tag{4.34}$$

where $a_t^{(j)}$ and $b_t^{(k)}$ are the time-varying AR and MA model coefficients and $\sigma_e^2(t)$ is the variance of the white noise process e_t at time t. This time-varying PSD estimate is also called the *instantaneous spectrum* [88]. One fascinating detail of this spectrum estimate is the fact that it can be derived from the evolutionary spectrum theory as described in [151].

The time-varying ARMA spectrum can be estimated by substituting the ARMA coefficient estimates $\hat{a}_t^{(j)}$ and $\hat{b}_t^{(k)}$, calculated using some adaptive algorithm presented in Section 4.1, and the estimated variance $\hat{\sigma}_e^2(t)$ of the prediction error process ϵ_t into (4.34). That is, the variance of the unknown white noise process e_t is approximated with the variance of the prediction error ϵ_t. The prediction error ϵ_t is calculated at every step of iteration in all presented estimation methods. The variance of ϵ_t can be estimated, for example, as [23]

$$\hat{\sigma}_\epsilon^2(t) = \frac{1}{t-m+1} \sum_{j=m}^{t} \epsilon_t^2 \tag{4.35}$$

where m is the time index at which the algorithm used to estimate the model parameters converges.

As in the stationary case, the frequency resolution of the time-varying ARMA spectrum estimate is implicitly restricted by the model structure even though equation (4.34) is a continuous function of frequency f and can be evaluated at any desired frequencies up to the Nyquist frequency $f_s/2$. The time resolution, on the other hand, is determined by the update coefficient of the adaptive algorithm. In the Kalman smoother this implicates the selection of the state noise covariance that adjusts the adaptation speed of the algorithm. In practice, a trade-off between the adaptation speed of the algorithm (time resolution of the spectrum) and estimate variance need to be done.

CHAPTER V

Analysis of galvanic skin responses

This chapter is concerned with analysis of galvanic skin responses. GSR is known to reflect autonomic response and has been, for example, used in the traditional lie detector devices. At first, a short introduction to GSRs including its origin, measurement, and waveform characteristics is given. After this, an advanced method for analyzing the patterning of successive GSRs is presented in detail. The proposed method is based on principal component analysis and was originally published in [175]. As a case study the method is applied to GSR measurements of 20 healthy controls and 13 psychotic patients.

5.1 Introduction

Electrodermal activity, that is the variation of skin resistance, is a simple, useful, and reproducible method of capturing the autonomic nerve response as a parameter of the sweat gland function [168]. One common term applied to this activity is the galvanic skin response. Physically GSR is a change in the electrical properties of the skin in response to different kinds of stimuli and any stimulus capable of an arousal effect can evoke the response.

The terminology applied to electrodermal activity is diverse. It is also known as the *psychogalvanic reflex*, *peripheral autonomic surface potential*, *skin potential response*, or more commonly as *sympathetic skin response* (SSR) [54]. Another measure of the electrodermal activity is the *skin conductance response* (SCR), which is a measure of skin conductance instead of potential. Most of the GSR studies in last decades have been concerned with the normal values of response amplitude and latency. Also the typical GSR waveshapes and the habituation effect of GSR responses for repeated stimulations have been studied.

In this chapter, a new practical method for analyzing the patterning of successive GSRs is presented. The method was originally proposed in [175] and it is based on PCA. The description of the method is given in Section 5.3.2 and in Section 5.4 the method is applied to GSR measurements of 20 healthy control subjects and 13 psychotic patients. The observed degree of similarity within successive GSRs was clearly higher for healthy subjects. For psychotic patients no clear time-locking or pattern was observed in measured responses. It will be

pointed out how PCA can be used to evaluate the patterning of responses and thereby discriminate GSRs of control subjects and psychotic patients. By means of clustering techniques presented in Section 5.3.2 a significant discrimination of the two subject groups is obtained.

5.2 Origin and measurement of electrodermal activity

The electrodermal activity originates from the eccrine sweat gland activity. The sweat gland secretion is activated by the sympathetic nervous system. Two types of sweating are generally recognized. That is, thermoregulatory sweating occurring over the whole body and emotional sweating which is confined to palmar and plantar sites and axilla. The two types of sweating do interact even though they have distinct basic neuroregulatory mechanisms [190]. The sweat gland secretion changes the conductivity of the skin. The surface of the skin consists of dead cells on top of the living cells. The sweat, on the other hand, can be considered equivalent to a 0.3% sodium chloride (NaCl) saline and, thus, sweat secretion increases the conductivity of the surface of the skin [108]. This change in skin conductivity can be easily measured.

There are practically two different methods for recording electrodermal activity, namely skin potential and skin conductance measurements [42]. In skin conductance (or resistance) measurements, current is applied between the recording electrodes and the resulting voltage is measured. In skin potential measurements, on the other hand, current is not applied, but the potential between the electrodes is generated due to differences in electrochemical reactions within the electrode-skin interfaces [121]. When amplitude levels are of interest, the conductance measurement should be preferred because the sensitivity of skin potential levels to hydration effects is probably greater that that of skin conductance levels [42]. The detection of skin potentials is, however, more sensitive than that of skin conductances and, thus, they can be preferred when amplitudes are not of particular interest. In addition, the measurement of skin potential is easier since it can be measured without applying voltage or current across the skin.

For electrodermal recordings silver-silver chloride (Ag/AgCl) electrodes with either potassium chloride (KCl) or sodium chloride (NaCl) electrolyte can be used. A bipolar electrode placement should be used in skin conductance measurements, whereas skin potentials must be recorded using a reference electrode placed on an inactive site. Palmar sites should be preferred, but also the plantar side of the feet can be used in recordings if necessary. Recommended places for the active electrode(s) on the palmar surface of the hand are the medial and distal phalanges of the fingers and the thenar and hypothenar eminences, see Fig. 5.1 (a). The reference electrode for skin potential recordings can be placed, for example, on the forearm or dorsal side of the hand.

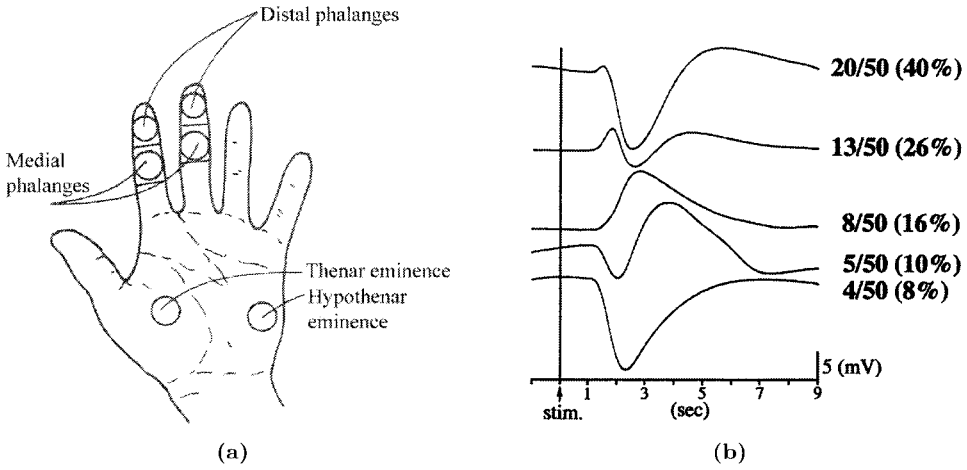

Figure 5.1: GSR measurements. (a) Typical electrode placements for recording electrodermal activity (redrawn from [30]). (b) Typical GSR waveforms, the most common waveform beginning with negative polarity in triphasic pattern is shown on top (redrawn from [7]).

5.3 Event-related GSRs

5.3.1 Waveforms and habituation

The waveform of GSR is typically either biphasic or triphasic, see Fig. 5.1 (b). Probably the most common waveform is a triphasic one starting with a small negative component followed by a strong positive component and ending with a slow negative component [9, 7, 183]. The waveform remains usually fairly unaltered between repeated stimulation, but also a clear change from one waveform to another is possible. The normal values of the response amplitudes and latencies have been studied extensively. Response amplitudes vary substantially, depending on the experimental conditions. In [40], an auditory stimulus was delivered to both ears and a mean amplitude of (2.8 ± 1.2) mV measured from the palmar site was observed, whereas in [187] a mean amplitude of (0.985 ± 0.300) mV was reported. The corresponding latencies for the palmar site where (1.50 ± 0.09) seconds in [40] and (1.49 ± 0.17) seconds in [187]. Latencies for the plantar site are about 0.6 seconds larger and amplitudes less than half of those for palmar site [184].

Common stimuli in GSR studies are the auditory stimulation, electrical stimulation, and transcranial magnetic stimulation. Response amplitudes have been shown to correlate with the stimulus intensity [40, 185], but it is also acknowledged that response amplitude is more dependent on the surprise effect of the stimulus than on the physical stimulus strength. Also the waveform has been reported to be dependent on stimulus intensity [185]. When GSRs are recorded for repeated

stimulations, the amplitudes tend to decrease and also the waveform can change. The largest response amplitudes are usually obtained for the first stimuli after which response amplitudes tend to decrease and at some point vanish completely. In addition, the latency of the response for repeated stimuli was reported to increase in [40], whereas in [20] the latency remained constant, but the duration of the response increased. This phenomenon in general is known as the habituation effect of GSRs and is mainly due to the decrease of the surprise effect of the stimulus [40]. Other factors affecting the normal values of GSR include the mental and emotional state [91, 193], ambient and skin temperature [96, 35], and age [36].

The duration of the response is typically between 2 and 6 seconds. Because GSRs are such long lasting waveforms interstimulus intervals (ISIs) should be long enough. When using short ISIs response overlapping should be considered by decomposing the overlapped responses. Such a decomposition for skin conductance responses is presented in [98].

5.3.2 Principal component analysis of GSRs

Principal component analysis discussed in Section 2.4 is a multivariate statistical procedure, where the vector containing the measured signal is presented as a weighted sum of orthogonal basis vectors. The central idea in PCA is to reduce the dimensionality of the data set, while retaining as much as possible of the variance in the original data. The dimensionality of measurements can be estimated by the number of basis vectors needed to estimate measurements in a certain accuracy.

Let the following notation for GSR measurements be used. The sampled potential after j'th stimulus is denoted with a length N column vector

$$x_j = (x_j(1), x_j(2), \ldots, x_j(N))^T. \tag{5.1}$$

As an observation model for the measurements the so-called additive noise model

$$x_j = s_j + e_j \tag{5.2}$$

is used, where s_j is the response signal corresponding to j'th stimulus and e_j is measurement noise. The measurement noise is assumed to be a stationary zero mean process. If there are M measurements, the response signals s_j will span a vector space $\mathcal{S}$, which will be at most of $\min\{M, N\}$ dimensions. In the case that the waveforms of the measured signals are rather similar, the dimension of the vector space $\mathcal{S}$ will be $K \leq \min\{M, N\}$ and measurements can be well approximated with some lower dimensional subspace of $\mathcal{S}$. Thus, each measurement can be expressed as linear combination

$$x_j = H_{\mathcal{S}}\theta_j + e_j \tag{5.3}$$

where $H_{\mathcal{S}} = (\psi_1, \psi_2, \ldots, \psi_K)$ is a $N \times K$ matrix of basis vectors which span the K dimensional subspace of $\mathcal{S}$ and $\theta_j \in \mathbb{R}^K$ is a column vector of weights to j'th measurement. By defining a $N \times M$ measurement matrix $X = (x_1, x_2, \ldots, x_M)$ the observation model (5.3) can be written in the form

$$X = H_{\mathcal{S}}\theta + e \tag{5.4}$$

where $\theta = (\theta_1, \theta_2, \ldots, \theta_M)$ is a $K \times M$ and $e = (e_1, e_2, \ldots, e_M)$ is a $N \times M$ matrix.

The critical point in the use of model (5.4) is the selection of basis vectors ψ_k. A variety of ways to select these basis vectors exist. Here a special case, i.e. principal component analysis introduced in Section 2.4, is considered. In PCA the basis vectors are selected to be the eigenvectors of either the data covariance or correlation matrix. Here, the correlation matrix is utilized. The eigenvectors of the correlation matrix are orthonormal and, therefore, according to Section 2.4.1 the ordinary least squares solution for the parameters (i.e. PCs) becomes

$$\hat{\theta}_{\mathrm{PC}} = H_S^T X \tag{5.5}$$

and the measurements X can be reconstructed by

$$\hat{X}_{\mathrm{PC}} = H_S \hat{\theta}_{\mathrm{PC}} = H_S H_S^T X. \tag{5.6}$$

Interpretation of principal components

The fact that the basis vectors are orthogonal has sometimes lead to interpretations that the basis vectors could represent some independent physiological sources of activity. This interpretation is however wrong because the fact that basis vectors are orthogonal is because they are eigenvectors of a symmetric matrix. Signals from independent physiological generators, however, are not necessarily orthogonal and as shown in [164] they can not be extracted with PCA. Even though the basis vectors have no clear meaning, it is reasonable to argue, based on [116], that variations in GSR latencies is here the main reason for the existence of additional components in PCA.

Quantitatively the first basis vector is the best mean square fit of a single waveform to the entire set of measurements. The second basis vector is the best mean square fit to the residual from the fit of the first factor, with a constraint that it is orthogonal to the first basis vector etc. Hence by using eigenvectors $(v_1, v_2, \ldots, v_K)$ corresponding to largest eigenvalues $(\lambda_1, \lambda_2, \ldots, \lambda_K)$ as basis, the best K dimensional approximation of measurements in the mean square sense is obtained. Because principal component solution is a best fit of a set of orthogonal functions to the set of signals, the solution will depend on the nature of the signal set.

In this work, the main interest is on the patterning, i.e. the similarity of the waveforms, of successive GSR responses. By normalizing the measured data PCA becomes sensitive to waveshape but not the signal amplitude. Information about the nature of measurements can be obtained from the PCs $\theta_j(k)$ and from eigenvalues λ_k. Whenever the observation matrix H_S is orthonormal, the coefficient $\theta_j^2(k)$ has the property of being the mean square contribution of k'th basis vector to j'th measurement [71]. When measurements are normalized $\sum_{k=1}^{\min\{N,M\}} \theta_j^2(k) = 1$ and $\theta_j^2(k) \times 100\%$ can be directly interpreted as the percentage contribution. The expected value of coefficients $(\theta_1^2(k), \theta_2^2(k), \ldots, \theta_M^2(k))$ associated with k'th basis

vector is [128]

$$E\{(\theta_1^2(k),\ldots,\theta_M^2(k))\} = E\{(v_k^T X)^2\} = E\{v_k^T X X^T v_k\} \quad (5.7)$$

$$= v_k^T E\{XX^T\} v_k = v_k^T R_X v_k = \lambda_k. \quad (5.8)$$

So that each eigenvalue λ_k represents the mean square contribution of the corresponding basis vector v_k to the measurements. If the first K eigenvectors are used in the observation model (5.4), the mean square reconstruction error averaged over all waveforms will be $\sum_{k=K+1}^{\min\{N,M\}} \lambda_k$. This is also the smallest conceivable mean square error. If the measurements are normalized $\sum_{k=1}^{\min\{N,M\}} \lambda_k = 1$. An ideal example of patterning is the case that all the measured waveforms are identical. Then there would be only one nonzero eigenvalue and the eigenvector corresponding to it would have the same shape as the measurements. So it is obvious that the magnitudes of largest eigenvalues describe the degree of patterning in the measured waveforms.

One possible visual way to estimate the patterning of waveforms is to plot the cumulative sum of the eigenvalues. The shape of such a curve describes the degree of patterning between various waveforms. A highly patterned signal set will have a sharply rising curve, rapidly approaching to its maximum $\sum_{k=1}^{\min\{N,M\}} \lambda_k$. If, on the other hand, there are only few common features between various signals the curve will approach the maximum very slowly.

Graphical representation of the data using PCs

One of the most useful properties of PCA is that the dimensionality of the original data set can be reduced substantially. This enables a distinct graphical representation of the multidimensional data in some lower dimensional subspace. For example, if two or three first PCs account for most of the variance in data, the data can be represented in two or three dimensions with respect to these PCs. If the aim is to represent characteristics of a set of measurements instead of a single measurement in, e.g., two-dimensional co-ordinates, the eigenvalues of the correlation matrix should be used instead of PCs. A natural choice would be to plot the first two or three eigenvalues of a data set, but also some other sensible combinations of the eigenvalues can be used. Other techniques, such as *principal co-ordinate analysis*, *biplots*, *correspondence analysis*, and *Andrews' curves*, for representing high dimensional data can be found in [73].

Besides the graphical representation, the PCs or the eigenvalues can be used in discrimination analysis. For example, measurement sets of different subjects can be discriminated into two or more groups based on the eigenvalues. Or similarly, single measurements can be discriminated based on PCs. For accomplishing such discriminations some kind of clustering or classification techniques need to be utilized.

Clustering techniques

The classification problem, in general, is to divide the observations into two or more groups based on their properties. The development of the classifier can be

divided into supervised and unsupervised techniques. In supervised techniques, learning sets for each group are first established using some sample observations and then each new observation can be classified by comparing its properties with the properties of each group. In unsupervised techniques, on the other hand, the properties of the groups are not known beforehand, but only some measure of proximity or similarity between observations is used. Such unsupervised classification techniques are often called *clustering*. In the clustering process, the set of observations is divided into a number of groups called clusters. The number of the clusters can be fixed in advance. Instead of clustering the original observations it could be more appropriate to perform PCA and cluster the obtained PCs or eigenvalues. Using this kind of approach the obtained clusters can be visually presented in two or three dimensions. This kind of approach has been used, e.g., in [48].

In this thesis, a simple hierarchical agglomerate clustering method will be employed. The basic idea in agglomerate clustering is to merge two closest clusters into one repeatedly, until the desired number of clusters is achieved or some predefined criterion is satisfied. The initial cluster partition is usually a singleton partition, in which each observation forms its own cluster. The crucial point of the method is the definition of the cluster-wise distance function. One simple cluster-wise distance function is the Euclidean distance of cluster centers. Let G_1 and G_2 denote two specific clusters and $\overline{G}_1$ and $\overline{G}_2$ the corresponding cluster centers (the mean values of the observations included in G_1 and G_2). The distance of the cluster centers is then given by

$$D(G_1, G_2) = \left\| \overline{G}_1 - \overline{G}_2 \right\|^2 \tag{5.9}$$

where $\|\cdot\|$ is the Euclidean norm. A clustering method using (5.9) as a distance function is called the *centroid method*. This method assumes that the observations within a cluster are Gaussian distributed with equal variance in each direction. Another distance function that takes into account the covariance structure of the group when calculating the distance between an observation and the group is the Mahalanobis distance. Several other clustering methods using different definitions for the cluster-wise distance function have been presented, e.g., in [16].

5.3.3 Practical method for analyzing GSRs

In the previous section, a PCA based method for analyzing GSR measurements was presented. To summarize the proposed method, it will be presented here in practical manner for discriminating response sets of different degrees of waveform patterning. The proposed method is described stepwise as follows.

1. Measure a set of GSR responses $X = (x_1, x_2, \ldots, x_M)$. Because GSR is a long lasting waveform, the ISI should be long enough to avoid response overlapping. Novelty stimuli are preferable in order to obtain distinct responses.

2. If habituation effect is strong, it is reasonable to reject the weakest GSRs from the analysis.

3. When waveshapes are of interest, the measured data should be normalized in some manner. One way to do this is to set the norm

$$\| x_j \| = 1, \quad \forall j = 1, \ldots, M. \tag{5.10}$$

This normalization makes PCA sensitive to waveshapes, but not to signal amplitudes.

4. Calculate the data correlation matrix R_X, which for discrete case can be approximated by

$$R_X \approx \frac{1}{M} \sum_{j=1}^{M} x_j x_j^T \tag{5.11}$$

and solve the ordinary eigendecomposition $R_X V = \lambda V$. Form observation matrix $H_S = (v_1, v_2, \ldots, v_K)$, where v_k is the k'th eigenvector of R_X corresponding to k'th largest eigenvalue λ_k. PCs $\hat{\theta}_{\mathrm{PC}}$ can be solved from (5.5) and estimates $\hat{X}_{\mathrm{PC}}$ for GSRs from (5.6). Note that when correlation matrix is used, an approximation for the mean of the GSRs is modeled automatically as the first eigenvector of the matrix, but if covariance matrix is used instead, the mean has to be included in the equations explicitly.

5. Information about the nature of a set of GSRs is obtained from the eigenvalues. If the patterning of the measured waveforms is high, the first eigenvalue will be relatively large. When patterning exist, but there are variations in response latencies it can be speculated that the second eigenvalue, which describes the derivative of the mean, will also be significant. Furthermore, the rest of the eigenvalues should be quite insignificant in the case of patterned waveforms. Corresponding information about single responses is obtained from coefficients $\theta_j^2(k)$. If the waveforms are not normalized these coefficients depend on amplitudes and they can be used to describe habituation. For example, the parameter

$$c_h = \frac{\Sigma_{j=1}^{3} \left(\theta_j^2(1) + \theta_j^2(2) \right)}{\Sigma_{j=1}^{\min\{N,M\}} \left(\theta_j^2(1) + \theta_j^2(2) \right)} \tag{5.12}$$

describes the relative dominance of the first three waveforms.

5.4 Case study

5.4.1 Materials and experimental procedure

As a case study, the GSR recordings of the first data set addressed in Section 1 were analyzed. The recordings were conducted on 20 healthy controls and on 13 first-episode patients with acute psychosis admitted for hospital evaluation. The *positive and negative syndrome scale* (PANSS) scores for the patients ranged from 99 to 120. None of the patients had ever used medication for psychiatric problems. Although main inclusion criterion was disturbance of reality-testing, the diagnostic

confirmation was verified by the *structured clinical interview* (SCID), carried out by a trained interviewer (Minna Valkonen-Korhonen, MD). GSRs were recorded using Ag/AgCl electrodes affixed to the palm and dorsum of the non-dominant hand. As a recording device a NeuroScan system (Compumedics Limited) was used. The sampling frequency of the device was 500 Hz and the passband was 0.3–50 Hz. For the analysis, the GSR signals were decimated to 31 Hz.

The experimental procedure for all subjects, used in this case study, was as follows. Two kinds of auditory stimuli, standard and target, were used in the stimulation according to classical oddball paradigm (85% standard stimuli of 800 Hz and 15% pitch deviants of 560 Hz with 1 second ISI). The duration of the standard and target stimuli were 84 ms including 7 ms rise and fall times. The total number of stimuli was 600. Among the standard and target tones there were 11 randomly presented unique novelty sounds (human sounds). Tone intensity was individually adjusted 55 dB above the sensation level. Subjects were advised not to pay attention to standard stimuli and to push a button when hearing a target stimulus. They were not informed about the novelty sounds. GSR was recorded continuously during the session and 8 second epoch after each novelty stimulus was extracted for analysis. The time between consecutive novelties was random but at least 30 seconds. Because of the long ISIs of novelty stimuli no response overlapping appeared in the measurements.

During the experiment, the identification of the target tones and the corresponding reaction times were measured. On average, the patients made 2.0 incorrect reactions for the standard tones and missed 3.9 target tones. The corresponding averages for the control subjects were 0.5 incorrect reactions and 0.8 missed targets. In other words, the patients made about four times more mistakes than the controls. The reaction times did not, however, differ significantly between the groups.

5.4.2 Results

The proposed method was then applied to the GSR measurements of the 20 healthy controls and the 13 psychotic patients. Measurement sets for all subjects are presented in Fig. 5.2. For each subject 11 responses of 8 second length were measured. Responses are plotted from bottom to top (the response for the first stimulus at the bottom) and the vertical axis is inverted (negative peaks point upward). The amplitude scale is different for each subject and the time instant 0 corresponds the occurrence of the stimulus.

At first, the method is demonstrated by applying it to GSR sets of typical control and psychotic subject. Afterwards, the discrimination of the two subject groups with respect to different parameters obtained from the method will be shown. For the typical control subject and psychotic patient, subjects C17 and P5 were selected. The 11 measured GSRs for these subjects are presented in Fig. 5.3 in the same amplitude scale.

The degree of patterning between these 11 successive responses is clearly higher for the control subject, latency variation is small and the response waveshape does not change prominently between repetitions. The approximated onset latency is

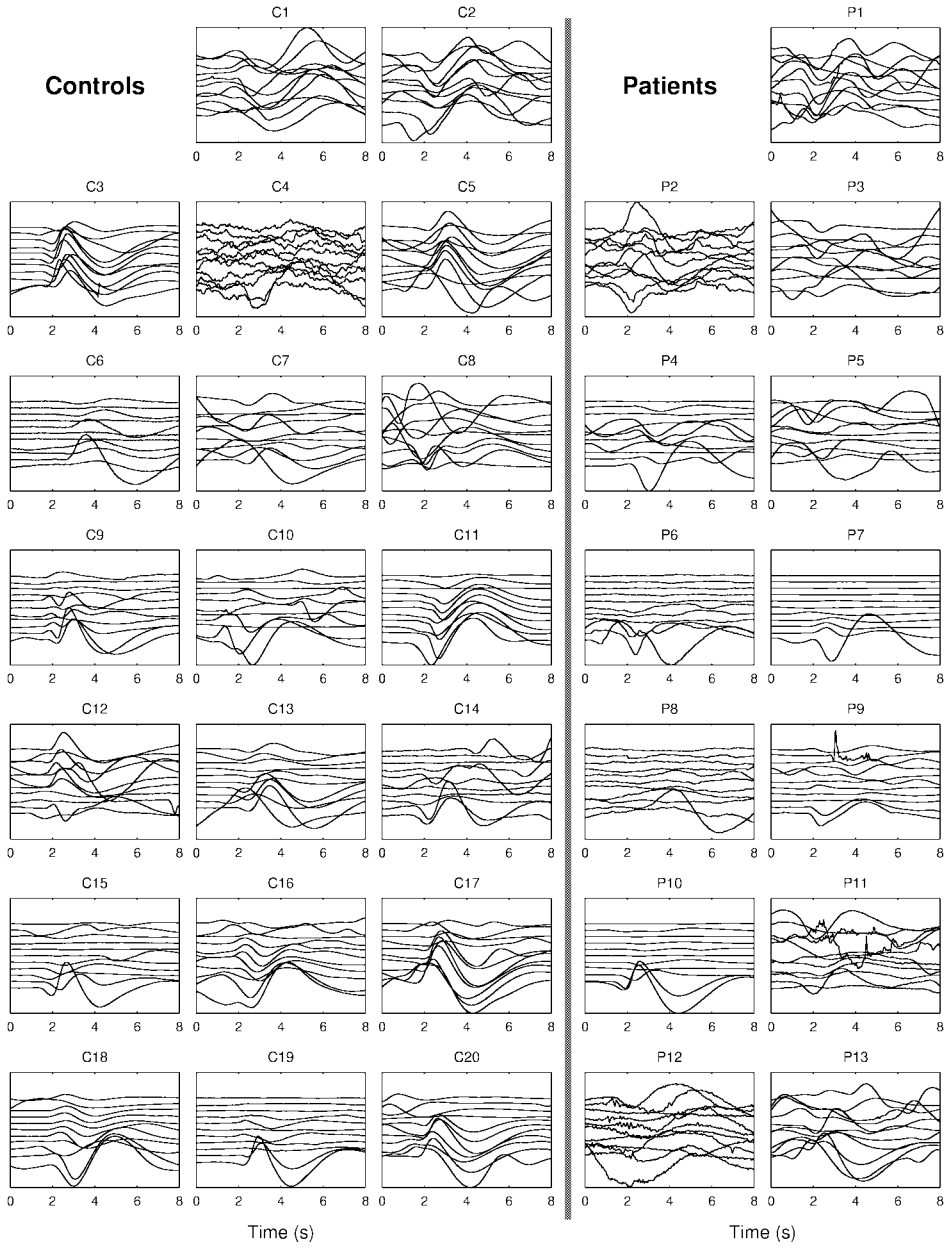

Figure 5.2: GSR measurements for healthy controls C1, C2, ..., C20 and for psychotic patients P1, P2, ..., P13 as waterfall plots. The amplitude scale is unique for each subject.

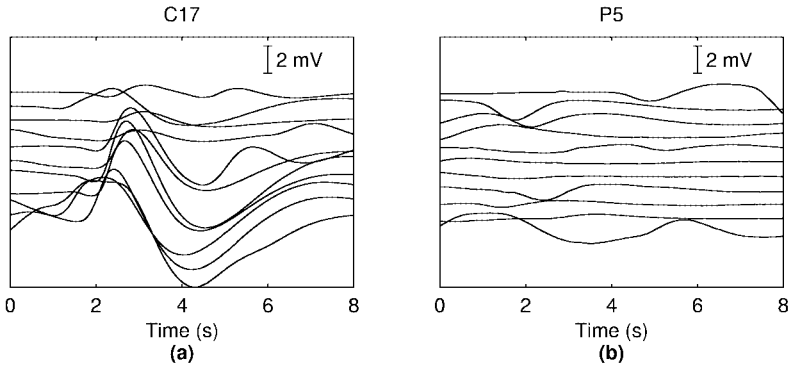

Figure 5.3: Measured responses for (a) healthy control (C17) and (b) psychotic patient (P5) as a waterfall plot.

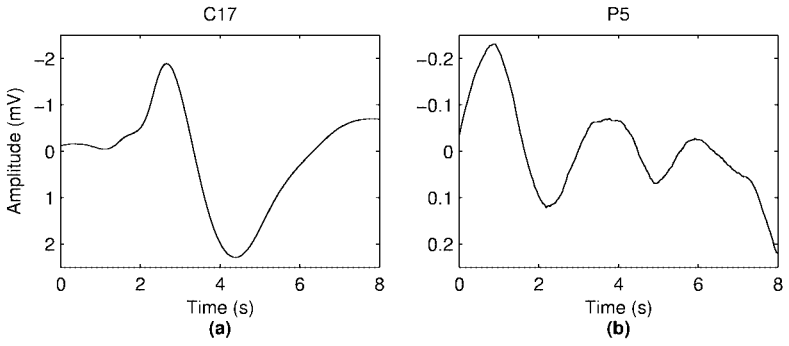

Figure 5.4: The mean values of measurements for (a) healthy control (C17) and (b) psychotic patient (P5). Note that the amplitude scale for psychotic patient is 10 times smaller than for healthy control.

about 1.8 seconds. For psychotic patient the lack of time-locking in GSRs seems to be characteristic and there is not any observable pattern in the measurements. Mean values of the 11 responses are presented in Fig. 5.4. The mean value for the healthy subject represents a very common response waveform starting with a negative phase. For the psychotic subject the mean value is not a realistic prototype for a GSR waveform and it seems to arise immediately after the stimulus. Conclusions about the waveform patterning and normality of the responses could be drawn by simply looking at the mean of the measurements. Instead of stopping here we are aiming to a more sophisticated way to analyze GSR responses.

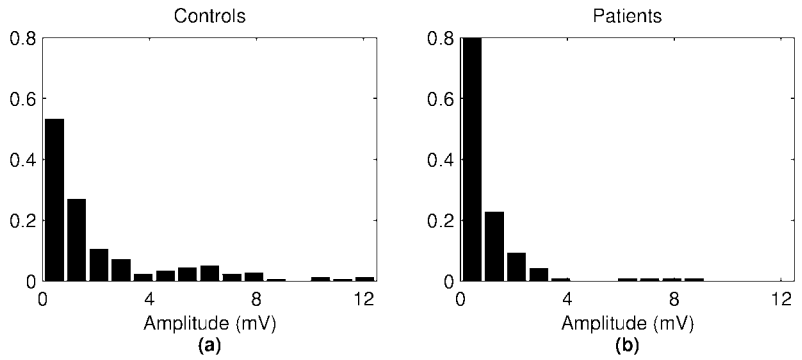

Figure 5.5: Peak to peak amplitudes for (a) healthy controls and (b) psychotic patients.

Amplitudes and habituation

GSR amplitudes were defined from peak to peak at time window from 1 to 6 seconds after stimulus onset. This is the time frame in which GSR peaks normally appear. Response amplitudes in Fig. 5.3 are much higher for the control subject compared with the patient. In fact, there is a small difference in amplitudes between the two subject groups as can be seen from Fig. 5.5, which shows the histograms of peak to peak amplitudes of all responses of all subjects in the two groups. However, the amplitude variation within control subjects is rather substantial and, therefore, response amplitudes can not be used to discriminate the subject groups.

For most subjects a significant habituation of amplitudes was observed. The habituation is seen from responses of the control subject in Fig. 5.3. The largest response amplitude is 7.75 mV and the smallest only 0.85 mV. So the decrease in amplitudes is about 89%. Within all control subjects the habituation varies between 67 and 99%, even though novelties were used in stimulation.

Observed habituation effect must be taken into account in the analysis. It is possible that the weakest measurements in a set do not feature responses to specific stimuli at all. Instead, a weak measurement can include a response to some preceding target stimulus and the contribution of measurement noise is also notable. Based on these observations it is reasonable to reject the weakest responses from the analysis and focus on the patterning between the most substantial waveforms.

PCA analysis

Because of the strong habituation effect, it was decided that only the 6 most substantial waveforms are analyzed. The rejected 5 measurements of smallest norms are usually responses to last stimuli and do not necessarily feature responses to specific stimuli. Because waveshapes are of interest, each selected response is

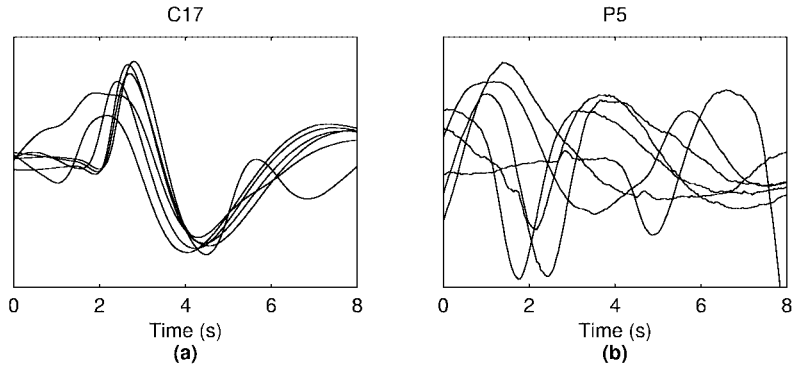

Figure 5.6: Selected normalized responses for (a) healthy control (C17) and (b) psychotic patient (P5).

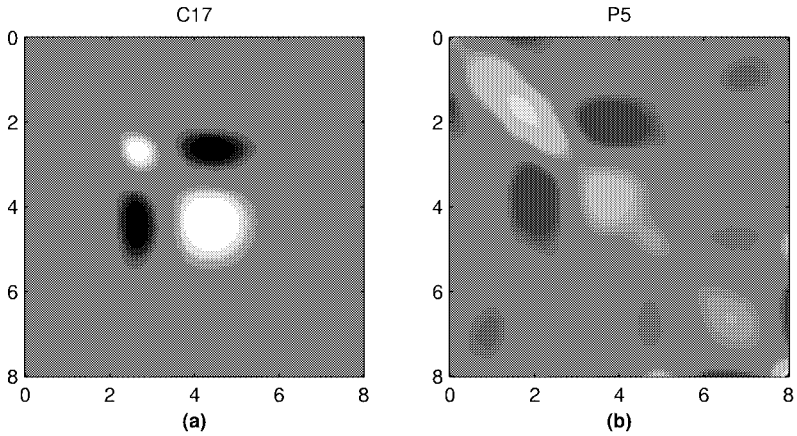

Figure 5.7: Correlation matrix for (a) healthy control (C17) and (b) psychotic patient (P5) displayed as an gray-scale image. The values of positive correlation are printed in white and the values of negative correlation in black.

normalized to unit norm. This normalization makes PCA sensitive to waveshapes only. The normalized selected responses are presented in Fig. 5.6.

First step in PCA is to calculate the correlation (or covariance) matrix of data. Correlation matrices of selected responses are presented in Fig. 5.7. For control subject one can distinguish regions of strong positive and negative correlations. The two regions of positive correlation (printed in white) in the diagonal are due to the time-locking of the two peaks in GSR signals. For the regions of negative

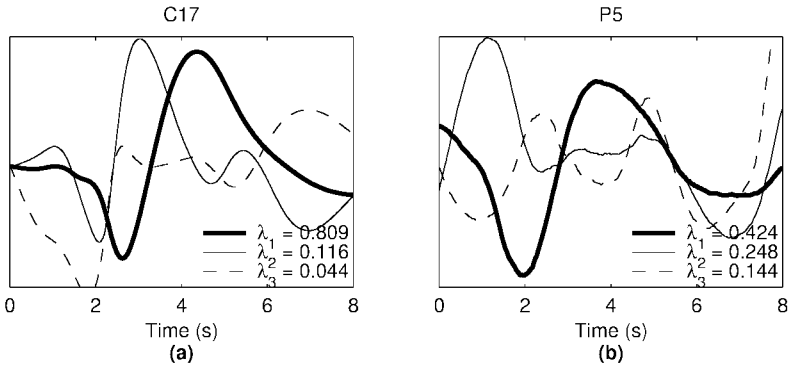

Figure 5.8: Eigenvectors corresponding to the three largest eigenvalues (λ_1, λ_2, and λ_3) of the correlation matrix of the measured GSRs for (a) healthy control (C17) and (b) psychotic patient (P5).

correlation (printed in black) the peaks in signals are negatively correlated. For psychotic patient there is not as significant strongly correlated regions as for control subject.

Three eigenvectors, obtained from eigendecomposition of data correlation matrix, corresponding to largest eigenvalues are presented in Fig. 5.8. For the control subject the first eigenvector is quite similar with the mean of the measurements in Fig. 5.4. The mean square contribution of the first eigenvector to the measurements is approximately 81% and the contribution of the first two eigenvectors is over 92%. For the psychotic patient, for whom the patterning of the GSR waveforms is clearly weaker, the total contribution of the first two eigenvectors is only about 67%.

The nature of the eigenvalues can be presented visually by plotting the cumulative sum of the eigenvalues. The cumulative sum of six largest eigenvalues is presented in Fig. 5.9. The curve for control subject is more rapidly rising and approaches the maximum earlier. This is characteristic for a highly patterned signal set.

When calculating parameters θ and estimates for measurements the number of eigenvectors to be used in the observation matrix H_S has to be decided. Some rules for this decision are discussed in [73]. Here, three most dominant eigenvectors, which are presented in Fig. 5.8, are used. Parameters θ are solved from (5.5) and the squares $\theta_j^2(1)$, $\theta_j^2(2)$ and $\theta_j^2(3)$ that describe the mean square contributions of the three largest eigenvectors to selected measurements ($j = 1, \ldots, 6$) are presented in Fig. 5.10. For control subject the contribution of the first eigenvector is clearly the most substantial to all waveforms and the contribution of the third factor is effective only to the first measurement. For psychotic patient the contribution of the first eigenvector is biggest only to half of the responses while the other half are contributed more by the second or third eigenvector. The estimates for the

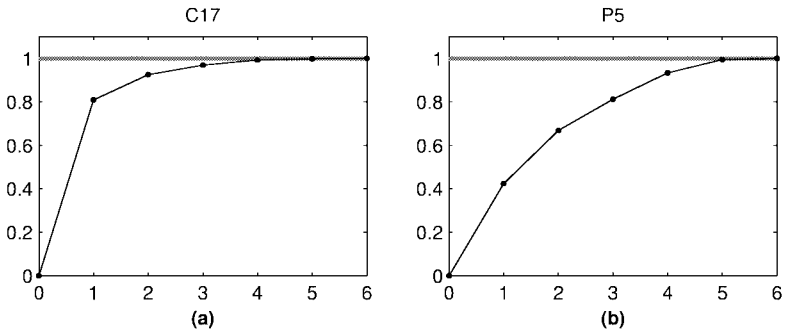

Figure 5.9: The cumulative sum of largest eigenvalues for (a) healthy control (C17) and (b) psychotic patient (P5) as a function of the number of eigenvalues summed (•). The sum of all eigenvalues is 1 (═).

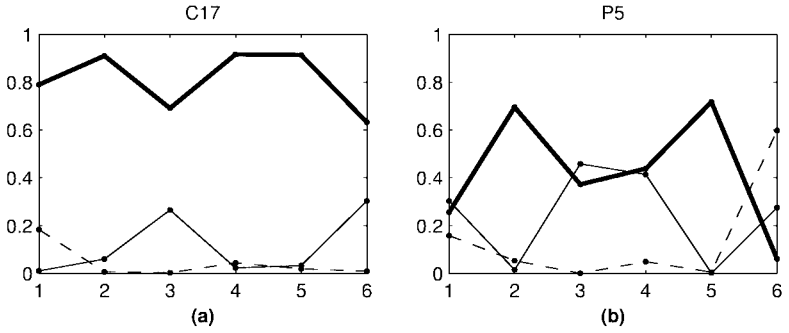

Figure 5.10: Coefficients $\theta_j^2(1)$ (▬), $\theta_j^2(2)$ (—), and $\theta_j^2(3)$ (– –) for selected measurements ($j = 1, \ldots, 6$) for (a) healthy control (C17) and (b) psychotic patient (P5).

six selected waveforms calculated from equation (5.6) are presented in Fig. 5.11. Clearly, the responses of the control subject can be modeled more accurately with the three first eigenvectors.

Cluster analysis

In this section, the clustering of the two subject groups is examined. Since the purpose is to discriminate GSR sets, instead of single responses, the clusterization will mainly consist on the eigenvalues that describe the mean square contributions of corresponding eigenvectors. However, the regression parameters $\theta_j(k)$ are also considered because they contain all the information about the nature of

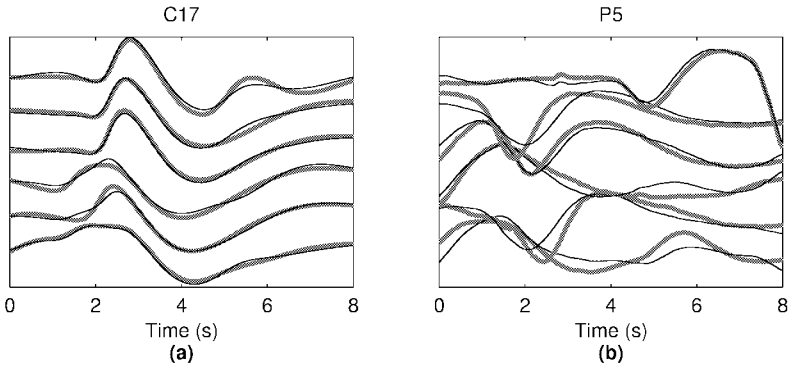

Figure 5.11: Selected normalized measurements (═) and estimates (—) for (a) healthy control (C17) and (b) psychotic patient (P5).

single GSRs. All clusters are formed with a hierarchical agglomerate clustering algorithm, with cluster-wise distance defined by equation (5.9).

First, the clusterization of the groups when only six most substantial waveforms, normalized to unit norms, are analyzed. Fig. 5.12 shows a plot of the sum of two largest eigenvalues $\lambda_1 + \lambda_2$ with respect to sum $\sum_{k=1}^{M} \lambda_k$ (reconstruction error when measurements are estimated with three most dominant eigenvectors). The clustering of groups is clearly seen, but is not complete. Most of the control subjects (14/20) are clearly clustered in the bottom right corner. For these controls the contribution of two largest eigenvectors is over 85% and the reconstruction error when three largest eigenvectors are used in reconstruction is less than 5%. But there are also six controls among psychotic patients.

The same kind of clustering is seen in a plot of third eigenvalue λ_3 with respect to fourth eigenvalue λ_4 in Fig. 5.13. Both λ_3 and λ_4 are small for a majority of control subjects. Now eight control subjects are among psychotic subjects and six of these are in fact the same ones which deviated from other controls in Fig. 5.12. Figs. 5.12 and 5.13 clarify the capabilities of PCA to discriminate GSR sets, even though the clusterizations are not complete.

For comparison, PCA is performed to all 11 waveforms without normalization. Then PCA is sensitive to signal amplitudes and, thus, the strongest signals dominate the shapes of the eigenvectors. The clusterization with respect to the sum $\lambda_1 + \lambda_2$ and $\sum_{k=4}^{M} \lambda_k$ is shown in Fig. 5.14. There are four psychotic patients among the controls group. This is due to a strong habituation effect of GSR waveforms as can be seen from Fig. 5.15, where parameter c_h calculated from (5.12) with respect to $\lambda_1 + \lambda_2$ is presented. Figure shows a strong habituation for all the four patients clustered into controls group.

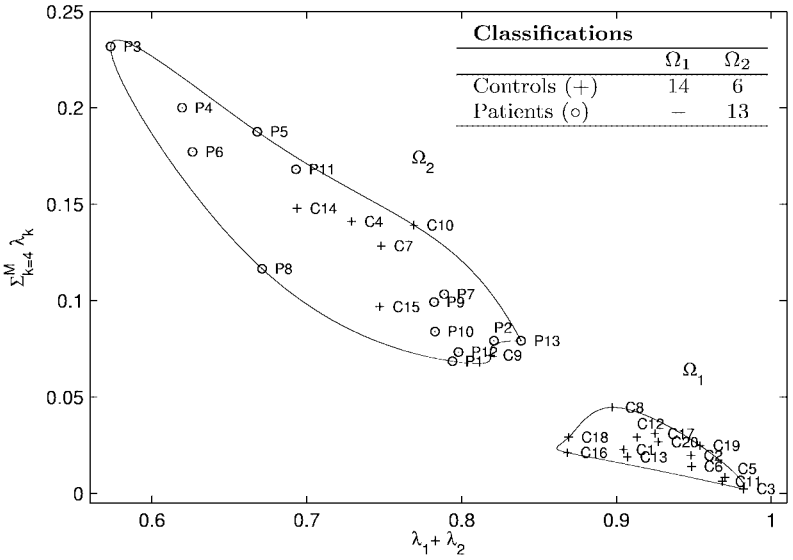

Figure 5.12: Clusterization of healthy controls (+) and psychotic patients (o) with respect to the sum of largest eigenvalues $\lambda_1 + \lambda_2$ and sum $\sum_{k=4}^{M} \lambda_k$. Six most substantial waveforms ($M = 6$), normalized to unit norms, were analyzed.

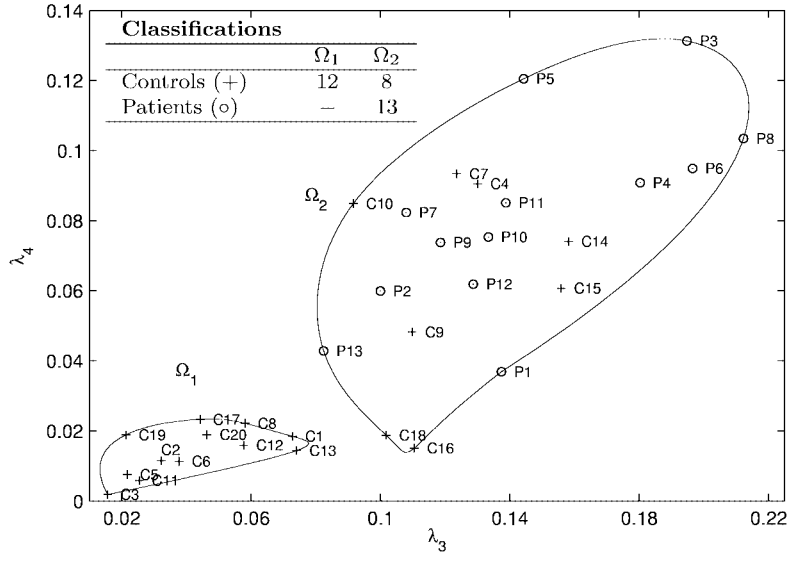

Figure 5.13: Clusterization of healthy controls (+) and psychotic patients (o) with respect to their third and fourth largest eigenvalues λ_3 and λ_4. Six most substantial waveforms ($M = 6$), normalized to unit norms, were analyzed.

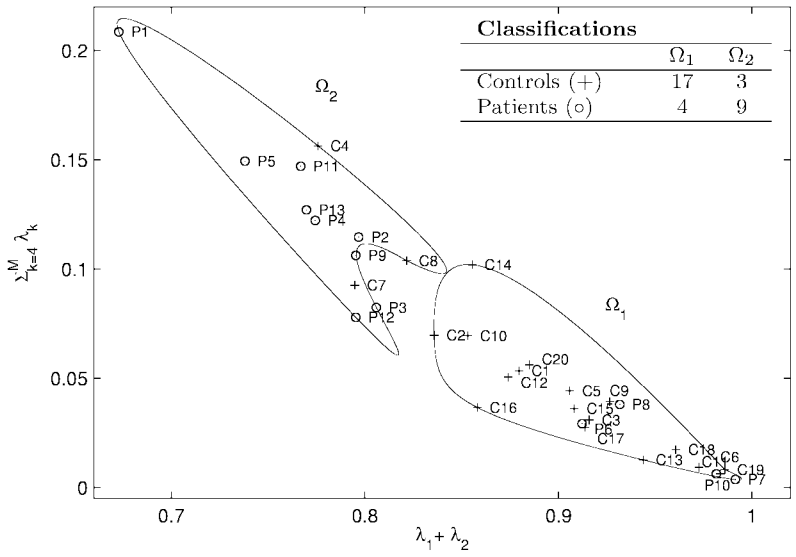

Figure 5.14: Clusterization of healthy controls (+) and psychotic patients (o) with respect to the sum of largest eigenvalues $\lambda_1 + \lambda_2$ and sum $\sum_{k=4}^{M} \lambda_k$. All 11 non-normalized waveforms ($M = 11$) were analyzed.

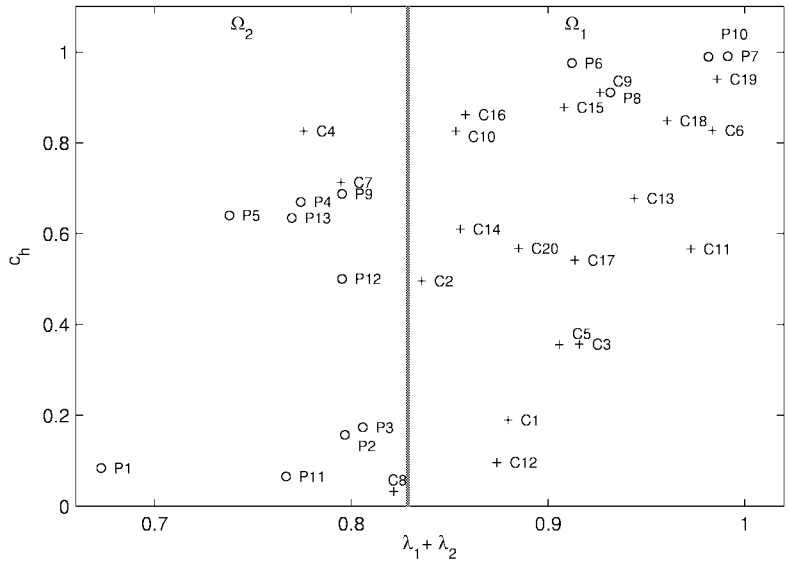

Figure 5.15: Plot of healthy controls (+) and psychotic patients (o) with respect to coefficient c_h and sum of largest eigenvalues $\lambda_1 + \lambda_2$.

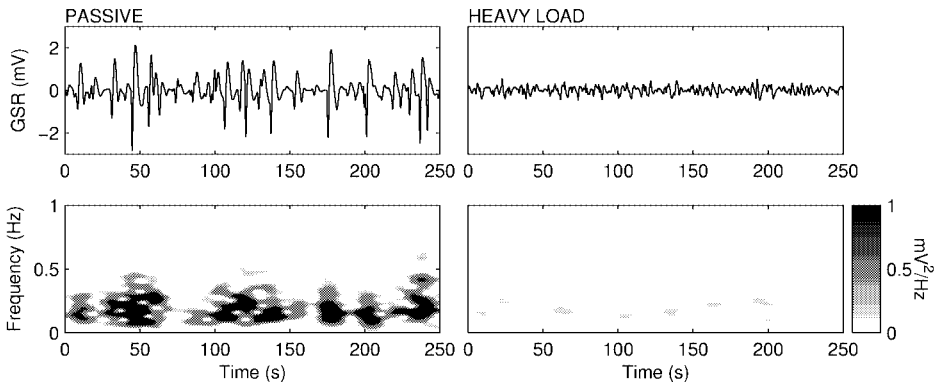

Figure 5.16: Typical spontaneous GSR signals and corresponding spectrograms for a healthy subject measured during a passive oddball paradigm (passive) and Wisconsin card sorting test (heavy load).

5.5 Spontaneous GSR

Instead of analyzing GSRs elicited to specific stimuli, it might also be useful to consider the spontaneous changes in GSR activity. Since GSR activity is controlled by sympathetic nervous system an increase in GSR activity, i.e. increase in amplitude and occurrence rate, can be interpreted as increased sympathetic activity. In addition, GSR has been related to factors such as attention, emotional arousal, and information processing [28]. Therefore, analysis of spontaneous GSR activity is a promising method. It has been used, e.g., in determination of drowsiness [204] and sleep stage quantification [97].

One obvious approach to analyze the spontaneous GSR activity is to consider its time-frequency representation. The most traditional such representation is the spectrogram. The frequency range of spontaneous GSR activity is usually between 0.01 and 1 Hz and the amplitudes are usually smaller than amplitudes of GSRs evoked by some surprising external stimuli.

Here, it is demonstrated how the cognitive task effects the spontaneous GSR activity. The spontaneous GSR was measured from a healthy subject during a passive oddball paradigm (passive) and during a Wisconsin card sorting test (heavy load) as in Neuroscan STIM (Compumedics Limited), see Fig. 5.16. In the passive oddball paradigm, the subject watched a silent video and was instructed not to pay attention to the tone stimuli. The amplitude of GSR activity is, as expected, higher for the passive task. This can also be seen from the spectrograms presented below the GSR signals. The center frequency of GSR activity is about 0.2 Hz corresponding to wavelength of 5 seconds and most of the power is confined between 0 and 0.4 Hz. Thus, one appropriate measure of GSR activity would be the average power within specific frequency band. Other useful measures are, e.g., the

number of slopes per time and the corresponding amplitudes.

5.6 Discussion

In this chapter, a new practical method for analyzing the patterning of successive GSRs was presented. The method was originally proposed in [175]. It was shown that GSR responses of different nature can be discriminated with the PCA based procedure. Regression methods are also needed when single responses are of interest. Previously PCA has been applied to skin conductance responses in [163] without application to clustering, but the procedure presented in this chapter is a totally new approach in GSR analysis. As a specific application the method was applied to GSR sets of healthy controls and psychotic patients and a good discrimination of the two subject groups was obtained.

The best obtained discrimination of healthy controls and psychotic patients is presented in Fig. 5.12. All patients were ranked correctly, but six controls were ranked as patients. This gives the method a sensitivity of 100%, specificity of 70%, and overall correct ratings of 82%. Furthermore, by using the binomial distribution it can be argued that in 95% probability the sensitivity of the method is 75.3 100%, specificity 45.7 88.1%, and overall correct ratings 64.5 93.0%. In a different kind of approach, the same data sets were visually examined and rated into patient and normal categories by 20 evaluators (10 physicists and 10 physicians) and an overall average for correct ratings of 78% was attained [189]. All evaluators were shown a picture of the single trial trend of a typical control and patient beforehand. None of the evaluators had any previous experience in GSR analysis, but 10 of them were professionals in signal processing and EEG analysis.

There were altogether six false-positive classifications (subjects C4, C7, C9, C10, C14, and C15 were classified as patients) in Fig. 5.12. These misclassifications are partly due to the habituation effect of GSR waveforms suggesting the extinction of GSR in repetitions. Responses of subject C4 seem to present abnormally large measurement noise, since the amplitudes of the responses are exceptionally small. Subject C4 was not however rejected because there were no problems in the recordings in our knowledge. Despite these misclassifications it should be noted that all patients were ranked correctly giving the proposed method a sensitivity of 100%. Thus, there were no false-negative rankings. This fact makes the method a promising approach to be applied in clinical practice as a screening test for specific risk-groups and prodromal patients in future. The method is inexpensive and noninvasive and, therefore, appropriate for the screening of larger populations as well. Subjects rated falsely as positive can be sorted out in more focused further follow-up studies (e.g. psychiatrist's interviews or structural magnetic resonance imaging).

One significant factor effecting on the proposed method is the selection of the number of waveforms M per subject to be analyzed. It is practically impossible to define a generic criterion for the selection of M. Instead M should be selected based on the experimental procedure. For example, the number of stimuli and the surprising effect of these are both decisive in selecting M. For example, when

several novelty sounds are presented the novelty sound starts to lose its surprising effect and is probably not able to evoke GSR response for long. This habituation effect should be taken into account when selecting M, since totally habituated responses do not carry information about the true GSR and can, therefore, cause distortion to analysis. In this study, the selection $M = 6$ seemed to be appropriate considering the number of stimuli and the habituation rate.

It should be emphasized that the basis for the proposed method is the experimental procedure. For the used test, the 11 successive GSR responses were typically clearly patterned for healthy controls whereas for psychotic patients the lack of time-locking was characteristic. Because of such clear distinctions in morphologies of GSR sets for healthy controls and psychotic patients, the second order statistics of the proposed method is sufficient for obtaining good results in practice. However, for more complicated test procedures some nonlinear methods could be necessary. One advantage of the proposed method is that the dimensionality of data set is reduced while retaining as much as possible of the variance in the original data. This reduction enables the graphical representation of the data and further analysis of clusterization. Another important property is the formability of the method according to the problem. Adjustments of the method can and should be done based on the signals under consideration. In this study, the sum of two largest eigenvalues was used as a measure of patterning of a GSR set instead of just the first eigenvalue. The second eigenvalue was included because it allows some variation in response latencies, which is thought to be normal in GSRs. The capability of the normalized correlation coefficient, which is a measure of similarity between two waveforms, to discriminate GSR sets was also tested, but results were not as good as were results obtained from PCA.

Chapter VI

Estimation of nonstationary electroencephalographic signals

In this chapter, the measurement of EEG recordings and the basic quantitative analysis methods are shortly introduced. For more extensive introduction to EEG research see, e.g., the handbook [123]. The main issue of this chapter is the estimation of nonstationary EEG signals. As a specific application, we have focused on the estimation of event-related synchronization/desynchronization dynamics of occipital alpha rhythm. For the estimation of the ERS/ERD dynamics a Kalman smoother approach is proposed. The presented approach was originally proposed in [173], but in this chapter the approach is covered in more details.

6.1 Introduction

Electroencephalogram is a recording of the electrical activity of the brain. It has been found to be a useful tool for studying the functional state of the brain and for diagnosing certain neurophysiological disorders. EEG signals are often quantified based on their frequency-domain characteristics. Typically the spectrum is estimated using the FFT. A fundamental requirement in the FFT-based spectral analysis is the stationarity of the analyzed signal. In [25], it was suggested that EEG epochs shorter than 12 seconds may be considered stationary. However, it is well known that EEG can exhibit considerable short-term nonstationarities. In such situations, time-frequency representation methods, discussed in Section 4.3, are required.

A traditional TFR method is the so-called spectrogram. In this method, the signal is implicitly assumed to be stationary within each windowed segment and the selection of the length of this window is followed by a trade-off between time and frequency resolutions. Another popular TFR method is the wavelet transform in which the window width is inversely proportional to the frequency resulting in improved time resolution at high frequencies and frequency resolution at low frequencies.

TFR methods have various applications in the field of EEG analysis. One of the most common applications is the analysis of ERS/ERD of EEG [83, 41, 39, 49, 51]. The terms ERS and ERD usually refer to stimulus-induced changes in EEG

amplitude or power within certain frequency band rather than synchrony. This is also the case here and, therefore, the present study should not be confused to studies of EEG synchrony such as [106]. TFR methods have also been used in the inspection of the frequency content of event-related brain potentials [117, 179], quantification of epileptic seizure dynamics [47, 206, 166, 202], and analysis of newborn EEG seizure events [15, 22].

Nowadays, one of the most popular TFR methods used in EEG analysis, and in biomedical applications in general, is the WT [188]. This method, however, suffers from the same kind of trade-off between time and frequency resolutions as the traditional spectrogram method. An improved time-frequency resolution can be obtained by using parametric spectral analysis methods based on time-varying linear models. One approach is to use a time-varying autoregressive moving average model. The frequency resolution of parametric methods is superior because of the implicit extrapolation of the autocorrelation sequence [110]. For the same reason the leakage effect of the classical spectral estimators, depending on the used windowing function, is suppressed.

The main task in parametric modeling is the estimation of the time-varying model parameters. For this, adaptive algorithms such as Kalman filter, LMS, and RLS have been adopted (see Section 4.1). Kalman filter, which is an optimal estimator in mean square sense, has been previously used in EEG analysis, e.g., in [67, 17, 68, 8]. A good overview on the analysis of nonstationary EEG with parametric models can be found, e.g., in [75, 167]. A drawback of the Kalman filter, as of all other adaptive algorithms, is the tracking lag present in the estimated parameters. This is especially disadvantageous when the aim is to estimate accurately some abrupt (perhaps event-related) changes of EEG. However, the tracking lag can be avoided by using a so-called smoother algorithm with the Kalman filter as described in Section 4.1.2. An estimator including the Kalman filter along with a smoother is called Kalman smoother.

In this chapter, a Kalman smoother approach for estimating time-frequency structures of nonstationary EEG signals is presented. This approach was originally presented in [173]. The tracking ability of the presented approach is tested with simulations and the advantages against commonly used adaptive filters are pointed out by comparing Kalman smoother with the popular forgetting factor RLS algorithm. As a specific application Kalman smoother is applied to quantification of ERS/ERD dynamics of occipital alpha rhythm. With the presented approach detailed time-frequency representations for single ERS/ERD samples can be extracted. By using the classical spectrogram method such details can no be observed without averaging several consecutive trials due to poor resolution.

6.2 Measurement and quantitative analysis of EEG

EEG is usually recorded with Ag/AgCl electrodes. To reduce the contact impedance between the electrode-skin interface, the skin under the electrode is abraded and a conducting electrode paste used. The electrode placement should conform the international 10-20 system shown in Fig. 6.1 [89]. One important

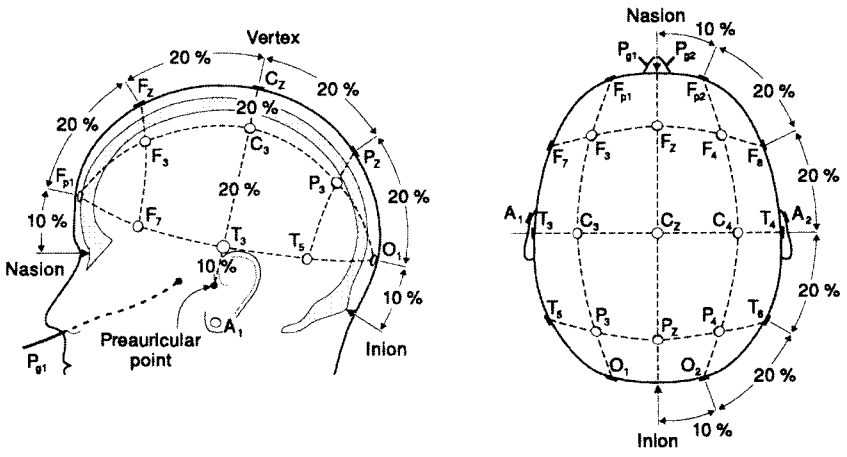

Figure 6.1: The international 10-20 electrode system (redrawn from [108]). A = ear lobe, C = central, Pg = nasopharyngeal, P = parietal, F = frontal, Fp = frontal polar, and O = occipital.

issue in the recording is the selection of the reference electrode. In common reference recordings, the reference site should be electrophysiologically as inactive as possible. Other approach is to use bipolar recordings in which EEG activity between two active sites is recorded. From the EEG recording it is possible to distinguish delta, theta, alpha, and beta waves (see Fig. 6.2). Besides the frequency of the observed rhythm also the site of the synchronized region generating it determines the classification of the rhythm [58]. The frequency content of EEG is confined below 70 Hz and, thus, the minimum sampling rate for acquisition is about 200 Hz.

The extent of different quantitative methods applied to EEG recordings is diverse [126, 127, 69, 148]. Usually, however, EEG activity is quantified in frequency-domain. Both power and amplitude spectrum representations have been used. The spectrum is calculated using either nonparametric or parametric methods. In clinical evaluation of EEG, the spectrum is commonly calculated using the FFT. One important issue in the spectrum estimation is that of stationarity. Usually EEG can be considered to be stationary only within some short epochs. In addition, EEG can exhibit several disruptive artifacts such as eye movement and eye blink artifacts. Therefore, the spectrum is usually obtained from several short artifact free stationary epochs that describe well the background activity (see Fig. 6.3). The epoch length is usually between 1 and 30 seconds depending on the quality of the recording. Longer epochs, yielding better frequency resolution, are preferred as long as sufficient number of epochs can be extracted from the recording. After

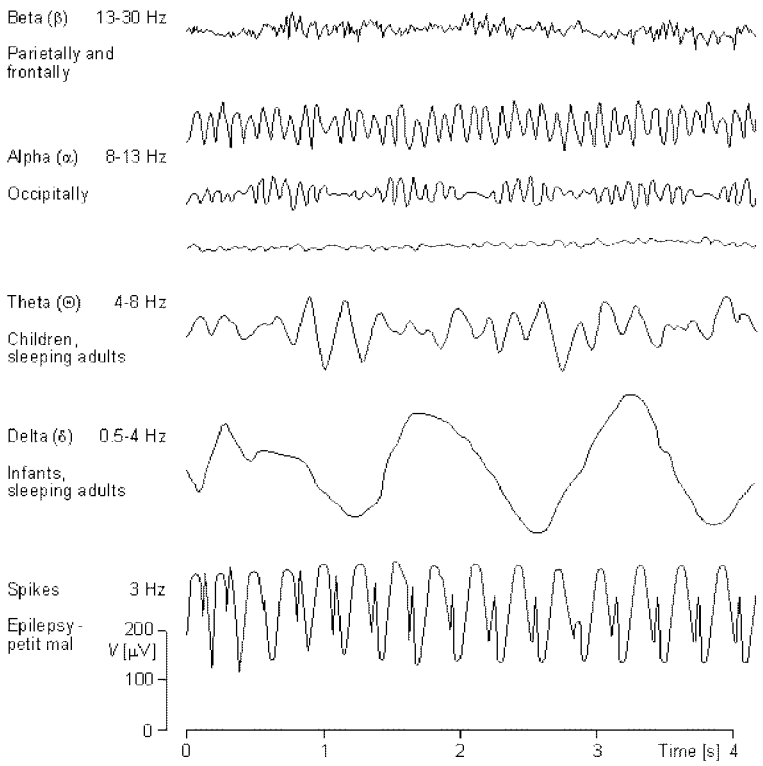

Figure 6.2: Some examples of EEG waves (redrawn from [108]).

the epochs are selected, the power spectrum estimate is obtained by averaging spectra of each epoch. The variance of the resulting spectrum depends on the number of epochs.

In the analysis, the EEG spectrum is divided into frequency bands. The classic frequency bands are 0–4 Hz (delta), 5–7 Hz (theta), 8–13 Hz (alpha), and 14–30 Hz (beta) [126]. These divisions are not, however, always followed. It is also common to further divide some of the bands, e.g., alpha band to alpha-I (8–10 Hz) and alpha-II (10–13 Hz) and beta band to beta-I (13–20 Hz) and beta-II (20–30 Hz). For each band measures such as absolute power and amplitude, relative power and amplitude, peak frequency, and mean frequency are extracted. In addition, power ratios between specific bands are often used.

6.3 Event-related synchronization/desynchronization

6.3.1 Alpha rhythm

EEG activity at the 8–13 Hz frequency band is, in general, called alpha rhythm [109]. To be precise, there are three physiologically distinct alpha rhythms, namely

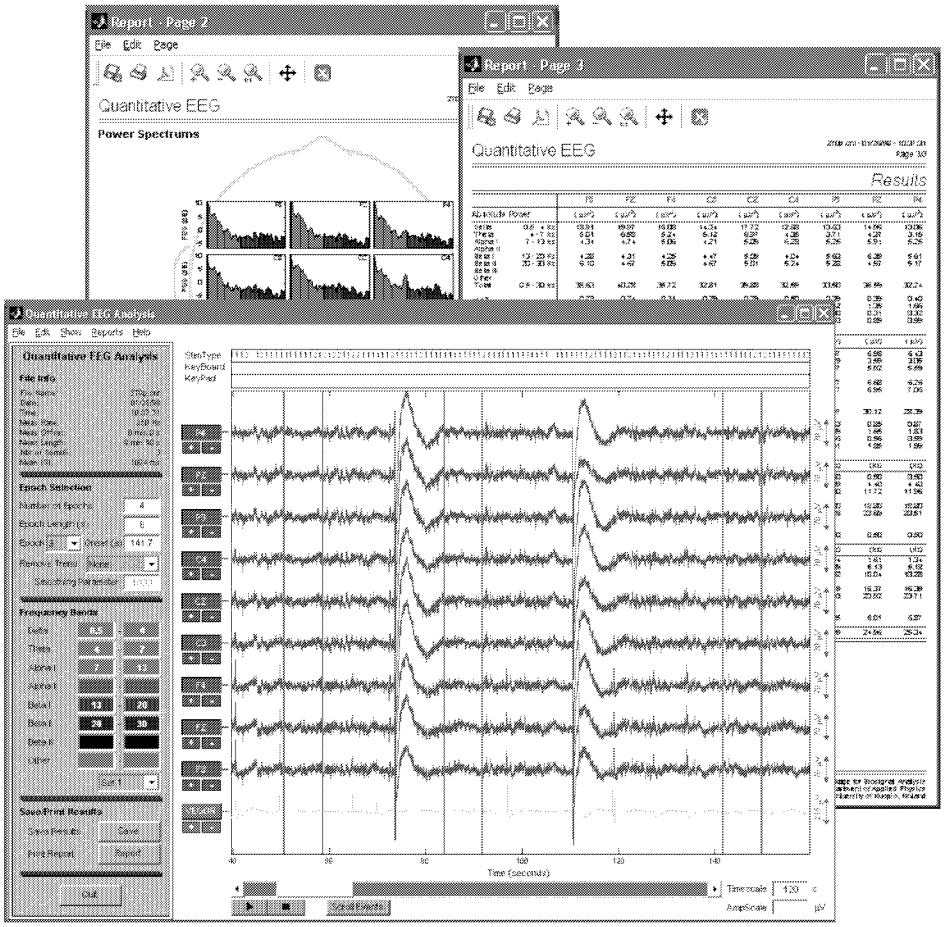

Figure 6.3: Quantitative analysis of background EEG activity. Program interface and reports of quantitative EEG analysis tool, part of the Biosignal analysis software [1].

the classical posterior alpha occurring during relaxed wakefulness, the Rolandic or central mu rhythm reactive to motor actions, and the midtemporal third rhythm which might sometimes fall into the upper theta band [122]. Here, only the classical posterior alpha rhythm will be considered.

The posterior alpha rhythm is best observed from parietal, posterior temporal, and occipital regions of the brain and is, thus, also referred to as occipital alpha rhythm. This rhythm begins to appear at the age of three months and evolves during maturation [122, 165]. At the time of appearance the frequency of this rhythm is about 4 Hz and it increases up to age of 11 12 years reaching the lower

limit of alpha frequency band at the age of 3 years. The amplitude of the alpha rhythm varies substantially between subjects, but it is usually between 20 and 100 μV with a slight asymmetry between hemispheres (higher amplitudes usually occur on the right hemisphere).

The occipital alpha rhythm is strongest with eyes closed during relaxed wakefulness. This rhythm is attenuated by attention and it is usually completely blocked by visual stimulation (e.g. opening the eyes). Such a stimulus induced attenuation or blocking is called ERD and the opposite phenomenon ERS [144]. The ERS/ERD has been differentiated to at least two alpha components with different spatial characteristics [145, 90]. In addition, the ERS after eye closure starts up at higher frequency and directly begins to shift to lower frequencies [109]. This short-term phenomenon of occipital alpha rhythm has been called the *"squeak" effect*. It does not occur every time the eyes are closed and, event though, it has not been reported to have any clinical significance [197] it is a good test for the resolution of the analysis method.

6.3.2 Analysis of ERS/ERD

The changes in ERS/ERD are time but not phase-locked to the entailed stimulus, and can not, therefore, be extracted by simple first order methods such as averaging, but may be detected by frequency analysis [144]. A traditional method, that has been used, e.g., in [143, 145, 144], for quantifying ERD dynamics is as follows. First of all, the ERD trials for every stimuli are filtered with a bandpass filter centered at the desired frequency band. The filter outputs are then squared in order to obtain power values. The ERD time course is finally obtained by averaging the squared filter outputs over all trials. In addition, the obtained time courses can be smoothed by averaging over time samples. A drawback of this approach is the rather low frequency resolution. Furthermore, the selection of the band limits can be problematic, even though, the limits are nowadays usually adjusted individually based on some specific frequency. Another traditional ERD quantification method is the intertrial variance method proposed in [77]. For a review on ERD estimation methods, see, e.g., [62].

An alternative approach is to use a high-resolution TFR method for representing the ERD in the time-frequency plane. This kind of a representation gives a comprehensive picture of the ERD dynamics and no prior frequency band selections are required. In addition, the classical ERD parameters, such as power and mean or peak frequency within some specific frequency band, can be easily extracted from the TFR. Here, the Kalman smoother approach will be used for estimating the time-frequency structure of the ERS/ERD samples.

6.3.3 Kalman smoother approach

In the Kalman smoother approach, the measured ERD trial is first modeled as an output of parametric model with time-varying parameters. Here, the time-varying ARMA(p,q) model given in (4.1) is used. The time-varying model parameters are then estimated using the Kalman filter algorithm along with a fixed-interval

smoother as described in Section 4.1. The state and observation noise covariances of the Kalman filter are set to $C_{w_t} = \sigma_w^2 I$ and $C_{e_t} = 1$, where the state noise covariance coefficient σ_w^2 is adjusted in such a way that a desired compromise between the variance of estimates and algorithm adaptation is achieved. Finally, once the model parameters are solved the time-varying PSD estimate can be obtained from (4.34) for each time instant. However, it is not always desirable to calculate the PSD estimate for each time instant, but only within some short time intervals. This can be obtained by averaging the estimated ARMA parameters with a moving window.

The ERD dynamics can then be easily extracted from the time-varying PSD estimate. The power variation within a specific frequency band is obtained by integrating the PSD estimate over the given frequencies. Correspondingly, the center frequency for the given band can be obtained as the frequency bisecting the power within the band.

6.4 Materials and experimental procedure

The ERS/ERD of occipital alpha rhythm was studied from six healthy subjects included in the second data set addressed in Section 1. In the test procedure, subjects closed and opened their eyes in accordance with auditory stimuli (beeps) at 15 second ISIs. While eyes open state, subject was instructed to focus the eyes to a fixed point. During the test procedure a total of 19 ERS/ERD samples were obtained for each subject.

As a recording device a Braintronics CNV/ISO-1032 amplifier with the international 10-20 electrode coupling was used. The common reference electrode was placed on the right mastoid. The sampling frequency of the device was 256 Hz and the passband was 0.3 70 Hz. The ERS/ERD for visual stimulation is best seen in the posterior and occipital regions of the brain. Therefore, the occipital O2 channel was selected for the analysis. The sampling frequency of the selected channel was reduced after lowpass filtering to 64 Hz. The measured ERS/ERD trials for one of the subjects are presented in Fig. 6.4.

6.5 Results

The dynamics of the measured ERS/ERD trials can be estimated using the Kalman smoother approach. At first, however, the performance and estimation accuracy of the proposed adaptive algorithm is evaluated. Usually, this is done with simulations. Here, two different simulations to test the tracking ability of Kalman smoother were conducted. In both simulations, Kalman smoother was compared to the popular forgetting factor RLS algorithm. After simulations, the time-frequency resolution of the proposed approach was compared with the traditional spectrogram as well as other common approaches and then used for tracking the dynamics of ERS/ERD transitions. At the end of the section, statistics of Kalman smoother spectrum estimates, especially the frequency resolution, is considered.

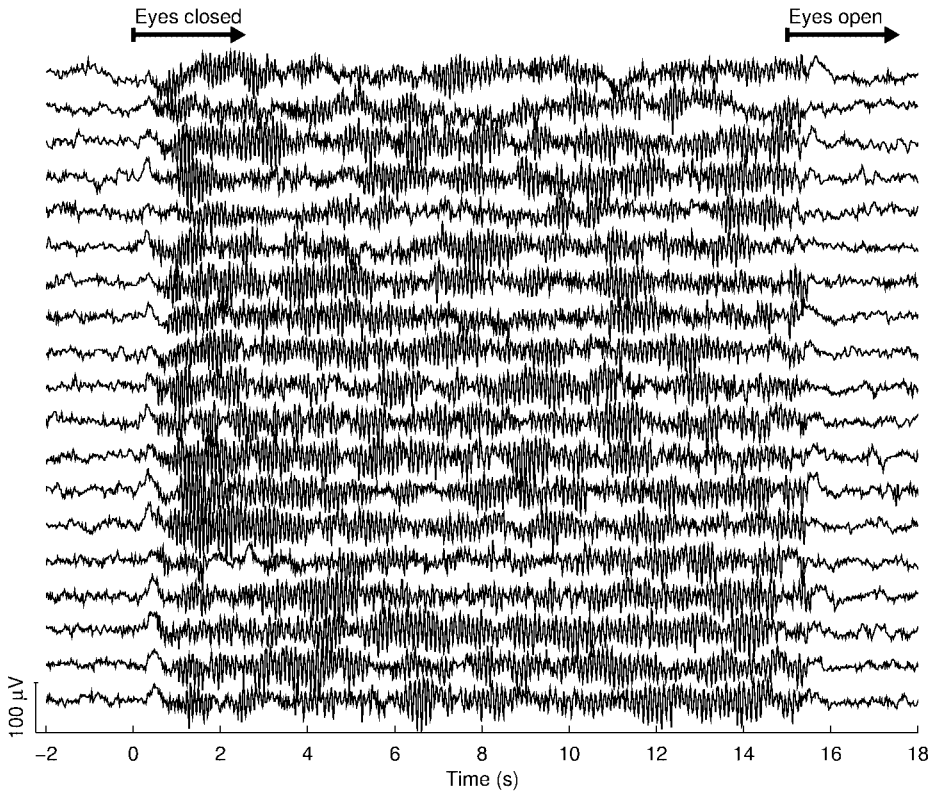

Figure 6.4: Measured ERS/ERD samples from O2 channel for one subject. A total of 19 samples were measured, the first one presented at the bottom. Auditory stimuli instructing subject to close or open eyes are presented at time instants 0 and 15 seconds.

6.5.1 Simulation studies

In the first simulation, a smoothly varying AR(2) process was generated. The trace of the simulated AR(2) model root and typical realization are presented in Fig. 6.5 (a). The parameters controlling the adaptation (i.e. the state noise covariance coefficient σ_w^2 of Kalman smoother and forgetting factor λ of RLS) were selected to minimize the estimation error of AR coefficients. Optimal values for the parameters were $\sigma_w^2 = 0.001$ and $\lambda = 0.935$ and the error for the Kalman smoother was 52% smaller than for RLS. Obtained estimates for the root modulus and frequency are presented in Fig. 6.5 (b). The other RLS estimate was calculated with a substantially larger forgetting factor ($\lambda = 0.98$). It is clearly seen that by increasing λ more stable RLS estimates are obtained but, as a downside,

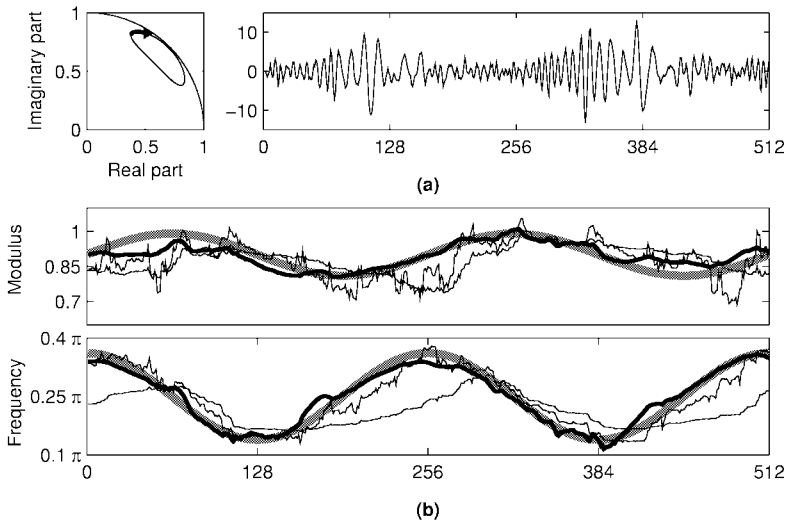

Figure 6.5: AR(2) process estimation with optimized Kalman smoother ($\sigma_w^2 = 0.001$) and RLS ($\lambda = 0.935$) algorithms. (a) The root evolution and a typical realization. (b) Estimates of the root modulus and frequency: true values (═), Kalman smoother estimates (—), and RLS estimates (—). The other RLS estimate (smoother with larger tracking lag) was obtained with $\lambda = 0.98$.

the tracking lag is increased. The tracking accuracy of the Kalman smoother is, however, clearly better than either of the RLS estimates. This simple simulation demonstrates the benefits of the Kalman smoother approach compared to other recursive estimators but, unfortunately, the applicability of the Kalman smoother on tracking of nonstationary EEG is not addressed by this simulation.

In the second simulation, an EEG transition from desynchronized to synchronized state was modeled. The used approach is presented in detail in [76] and is, therefore, described here only briefly. For other approaches to simulate nonstationary EEG see, e.g., [66, 196]. Occipital EEG recorded with the eyes closed shows high intensity in the alpha frequency band, classically defined as 8 13 Hz band [126]. By opening the eyes this intensity is decreased or even blocked. It can be thought that EEG exhibits a transition from one stationary state to another. Such a transition was here simulated by modeling both stationary states as an fifth-order AR process. The roots of the models were estimated from real EEG measured during an eyes open/closed test. The obtained roots for both states and the corresponding power spectra are presented in Fig. 6.6 (a). The strong peak near 0.37π in the eyes closed state spectrum is due to the increased alpha rhythm.

In order to make the simulation more realistic the abrupt transition between the two stationary states was smoothed as described in [76]. In the smoothing

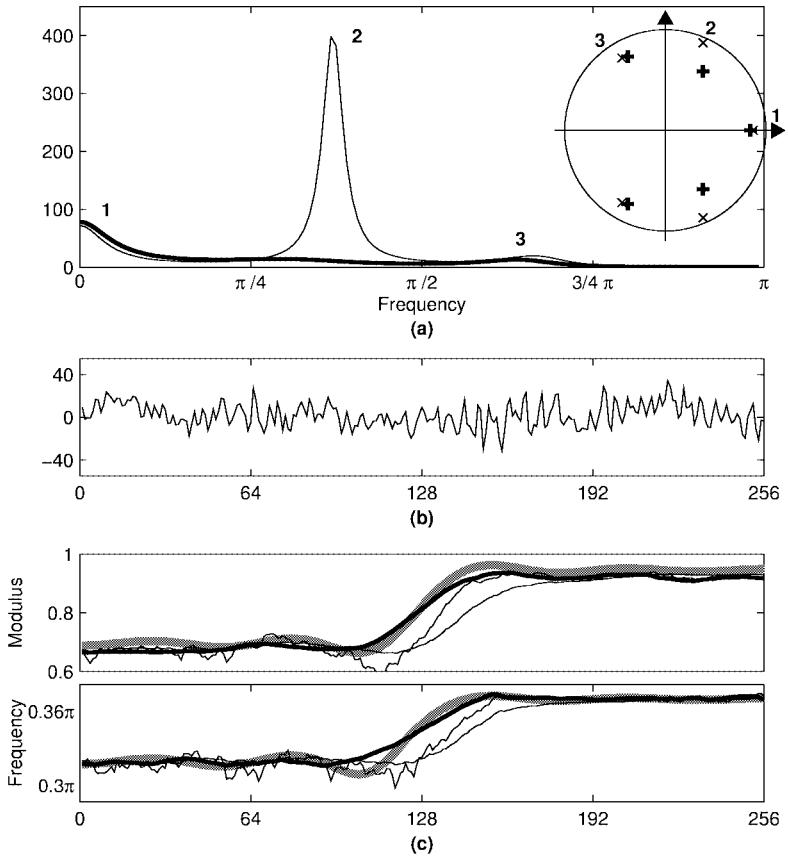

Figure 6.6: A realistic simulation of an EEG transition as an AR(5) process. (a) The roots and the corresponding spectra before (—) and after (—) the transition (eyes open → eyes closed). Numbers 1, 2, and 3 indicate the analogy of the roots and spectral peaks. (b) A typical realization of the smoothed transition. (c) Averaged estimates over 100 realizations of the modulus and frequency of the root 2 corresponding to alpha rhythm: true values (═), Kalman smoother estimates (—) with $\sigma_w^2 = 0.0001$, and RLS estimates (—) with $\lambda = 0.9$ (smaller tracking lag) and $\lambda = 0.98$ (smoother with larger lag).

procedure the time-varying AR coefficients having an abrupt transition at one point are presented as linear combinations of some shifted smooth basis functions. Here, shifted Gaussian functions were used. As well as the AR coefficients, also the prediction error variance evolution was smoothed.

A typical realization of the simulated ERD/ERS transition is presented in Fig. 6.6 (b). The simulated process was then estimated with Kalman smoother and

Table 6.1: Statistics of different estimators for the simulated AR(5) processes. The bias and standard deviation of the estimated AR coefficients $\hat{a}_t^{(1)}, \ldots, \hat{a}_t^{(5)}$ and the bias of the modulus $|\cdot|$ and frequency $\measuredangle\cdot$ of the root $\hat{\alpha}_t^{(2)}$ corresponding to alpha rhythm for RLS and Kalman smoother (KS) estimators. The root $\hat{\alpha}_t^{(2)}$ was obtained from averaged AR coefficients

	RLS ($\lambda = 0.9$)	RLS ($\lambda = 0.98$)	KS ($\sigma_w^2 = 3{\cdot}10^{-4}$)
	Bias±STD	Bias±STD	Bias±STD
$\hat{a}_t^{(1)}$	0.054±0.050	0.069±0.067	0.067±0.064
$\hat{a}_t^{(2)}$	0.128±0.067	0.085±0.089	0.068±0.069
$\hat{a}_t^{(3)}$	0.058±0.067	0.080±0.118	0.094±0.093
$\hat{a}_t^{(4)}$	0.062±0.107	0.117±0.158	0.063±0.146
$\hat{a}_t^{(5)}$	0.287±0.120	0.224±0.161	0.120±0.117
$\lvert\hat{\alpha}_t^{(2)}\rvert$	0.127	0.086	0.029
$\measuredangle\hat{\alpha}_t^{(2)}$	0.061	0.050	0.021

RLS algorithms by using a fifth-order AR model. Estimates were calculated for 100 realizations and the statistics of the obtained results are presented in Table 6.1. The bias of the averaged AR coefficient estimates and the standard deviations of single estimates are presented in the top five rows. A smaller bias for the Kalman smoother estimates is observed for the 2nd and 5th coefficient. These are the two AR coefficients for which the simulated transition effects the most. The estimates for the root corresponding to alpha rhythm were then calculated from the averaged AR coefficient estimates. Obtained estimates of the modulus and frequency of the root are presented in Fig. 6.6 (c). Biases of the estimates are presented in bottom of Table 6.1. RLS estimates were again calculated with two different forgetting factor values ($\lambda = 0.9$ and $\lambda = 0.98$) in order to demonstrate the trade-off between the tracking lag and stability of the estimates. The RLS estimates show that the tracking lag can not be entirely avoided even though quite small forgetting factor value is used. The Kalman smoother, on the other hand, can estimate the change very accurately.

6.5.2 Nonstationary EEG experiments

In order to demonstrate the tracking ability of the Kalman smoother on real EEG data it was first compared with the spectrogram. Both methods were applied to measurements of one subject and time-varying PSD estimates were calculated for every ERS/ERD trial. The underlying model for the Kalman smoother was selected to be ARMA(6,2) and the state noise covariance coefficient adjusting the adaptation was set to $\sigma_w^2 = 0.0001$, whereas a 1-second time-window corresponding to 1 Hz frequency resolution was used in the spectrogram. Averaged Kalman smoother spectra and spectrograms for the 19 ERS/ERD trials are presented in Fig. 6.7. From both averaged spectra it is observed that the synchronization seems

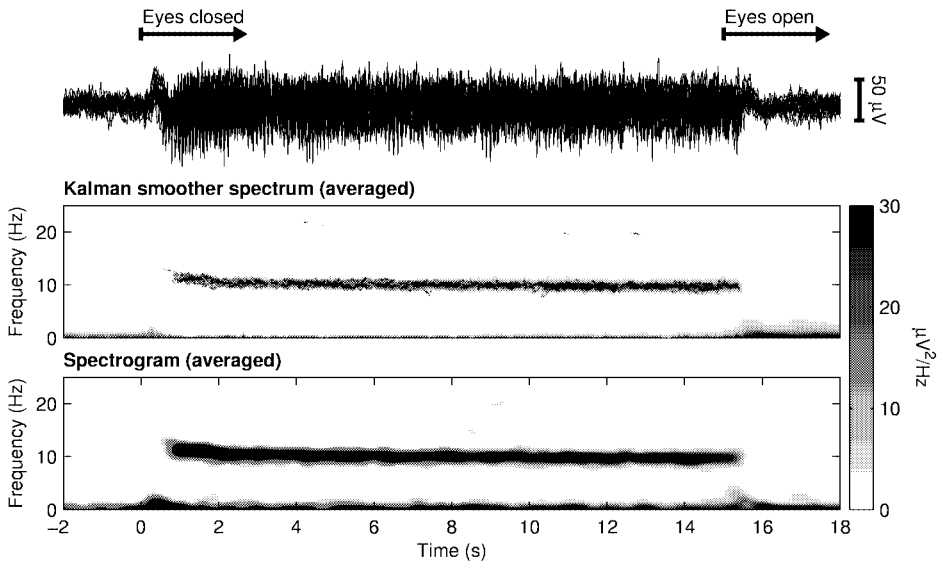

Figure 6.7: Averaged Kalman smoother spectra and spectrograms for the 19 ERS/ERD samples presented in Fig. 6.4.

to start at higher frequency and shifts to lower frequencies within few seconds. This is the well known "squeak" phenomenon of occipital alpha rhythm.

With the Kalman smoother approach the "squeak" effect can be observed even from a single ERS/ERD sample as shown in Fig. 6.8. With the spectrogram, on the other hand, this effect can not be seen from single sample due to the poor time-frequency resolution.

Next, the Kalman smoother approach was compared to some commonly used methods including the popular wavelet scalogram. A typical ERS sample presented on top of Fig. 6.9 was considered. Time-varying PSD estimates obtained with Kalman smoother, RLS, and LMS algorithms as well as spectrogram and scalogram are presented below the ERS sample. An ARMA(6,2) model was again used with the adaptive algorithms. The parameters adjusting the adaptation of each algorithm were selected based on visual inspection. The state noise covariance coefficient of Kalman smoother was set to $\sigma_w^2 = 0.0001$ and the forgetting factor of RLS to $\lambda = 0.94$. The step size of LMS was adjusted adaptively to be smaller than the reciprocal of the input power. In the spectrogram a 1-second time-window was used. The scalogram was computed using the Morlet wavelet as described in [120].

Time instant 0 in Fig. 6.9 corresponds to the stimulus occurrence instructing the subject to close the eyes. Shortly, after the eyes are closed, a substantial increase in alpha band power is observed in all spectra. The poor resolution of the classical spectrogram is evident when compared to the three parametric methods

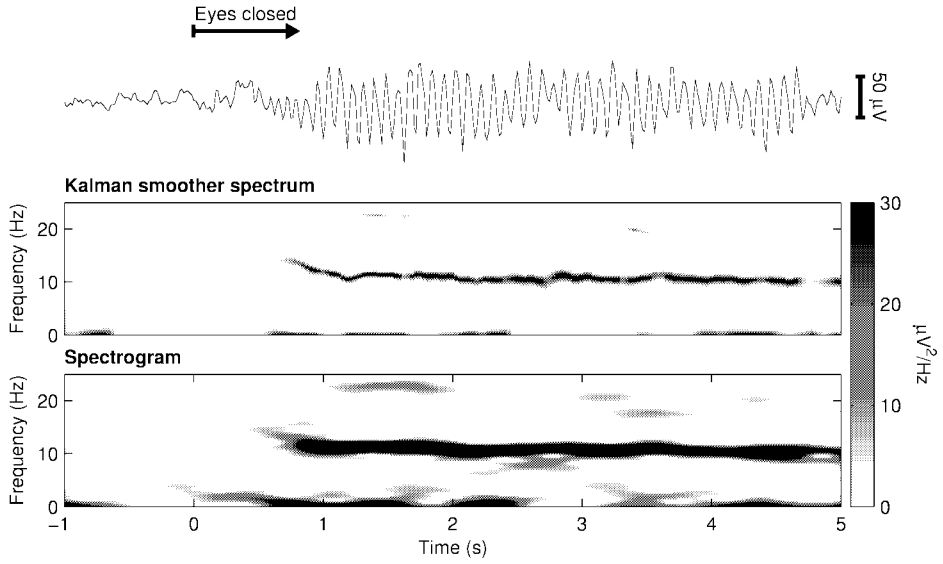

Figure 6.8: Kalman smoother spectrum and spectrogram for a single ERS sample.

and the WT does not produce remarkable improvement. The main drawback of RLS and LMS is the unavoidable tracking lag clearly seen in both spectra. The observed time-frequency resolution of the Kalman smoother is, on the other hand, extremely high. Even the short-term changes in alpha rhythm, e.g., the "squeak" phenomenon and the interval approximately from 4.3 to 4.7 seconds with decreased power in alpha frequency band, are detected reliably.

Finally, the Kalman smoother spectrum estimation method was tested with ERS samples showing short period changes in the alpha rhythm. The results for one such sample are shown in Fig. 6.10. In order to prove the capability of Kalman smoother method to detect short power changes, a simple alpha detection procedure was applied. First of all, the variation of power within alpha band was calculated by integrating the Kalman smoother spectrum over the alpha band (7–13 Hz). The obtained power variation is shown in Fig. 6.10 (a). Then, the original EEG signal was divided into epochs for which the alpha band power was greater/smaller than the selected threshold of 5 $\mu V^2/Hz$. At last, the epochs for which alpha power was greater than the threshold and the epochs for which it was smaller were concatenated and traditional FFT based spectrum estimates were calculated for the resulting signals [Fig. 6.10 (b)]. The results verify the absence of alpha rhythm in the other concatenated signal and, therefore, shows the applicability of Kalman smoother spectrum estimation method in case of short period EEG changes.

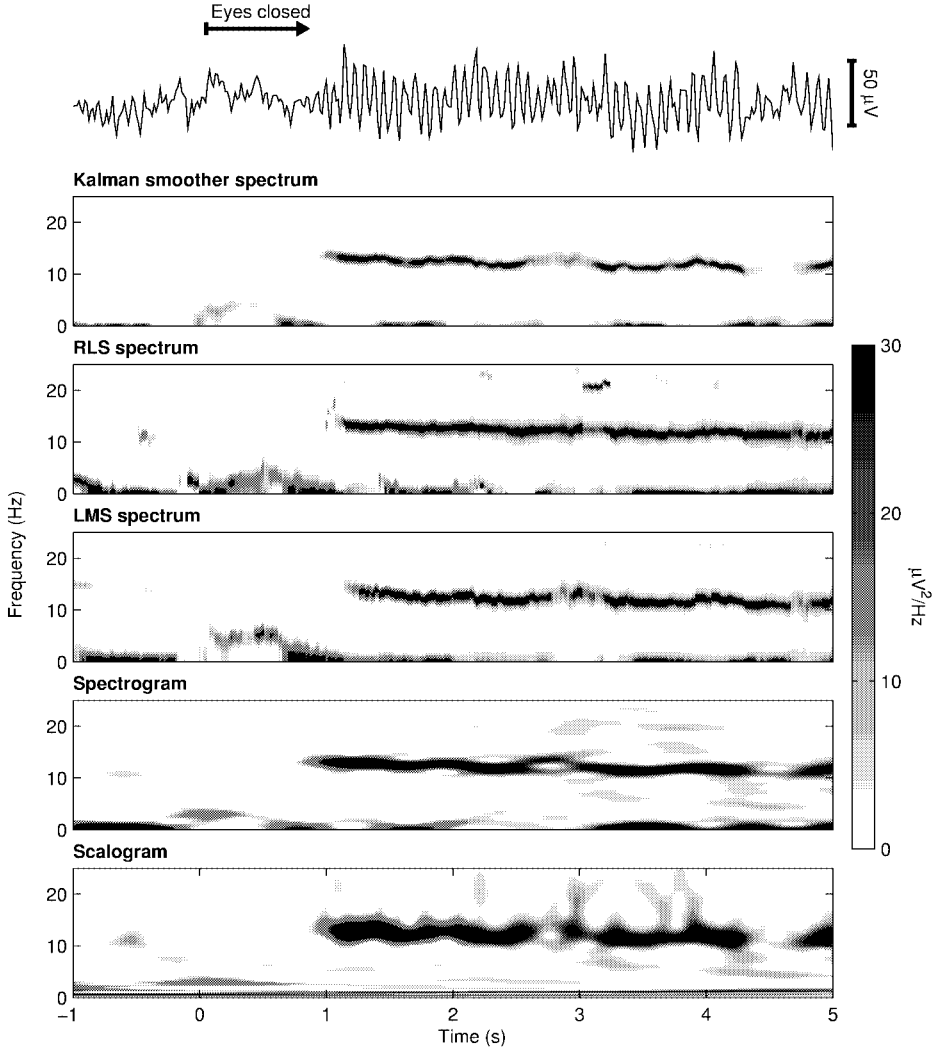

Figure 6.9: Estimation of time-varying PSD for a typical ERS sample with different methods. The measured ERS sample is presented on top and the different spectrum estimates underneath it.

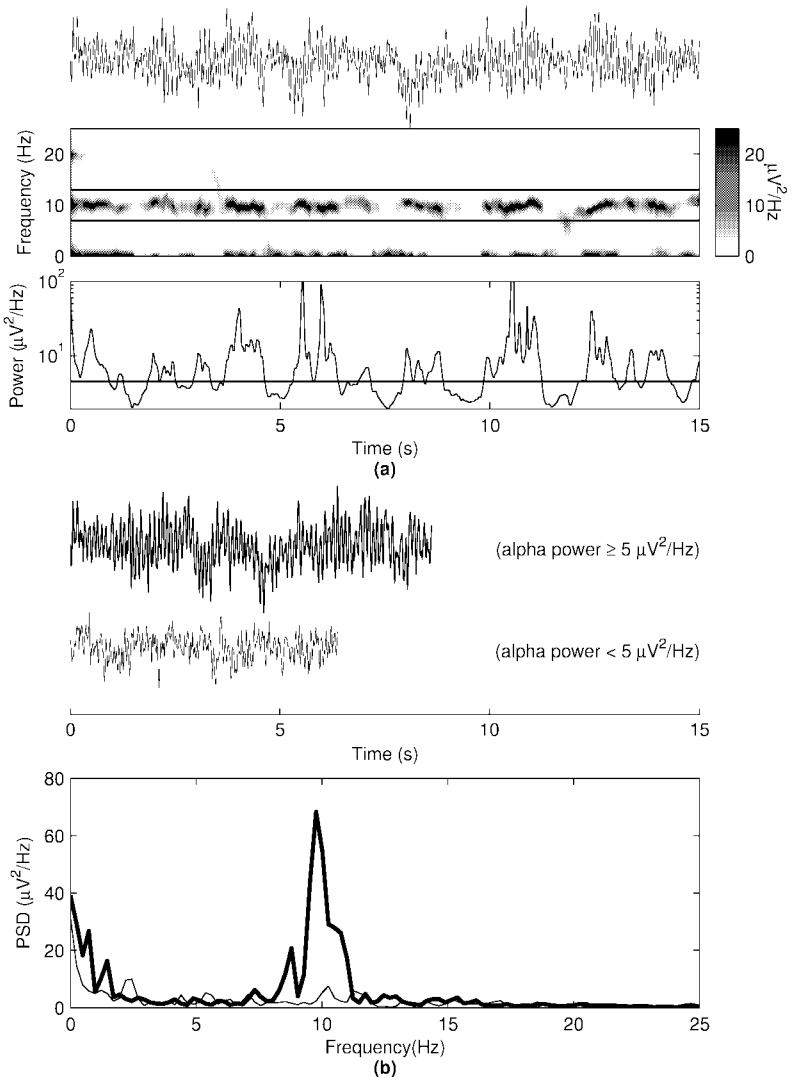

Figure 6.10: The performance of the Kalman smoother spectrum estimation method on EEG data with short period changes in alpha rhythm. (a) The EEG data measured in eyes closed state, corresponding Kalman smoother spectrum, and the power variation within the alpha band. (b) FFT based PSD estimates for the signals obtained by concatenating the EEG epochs where the detected alpha band power was greater (—) or smaller (—) than 5 $\mu V^2/Hz$.

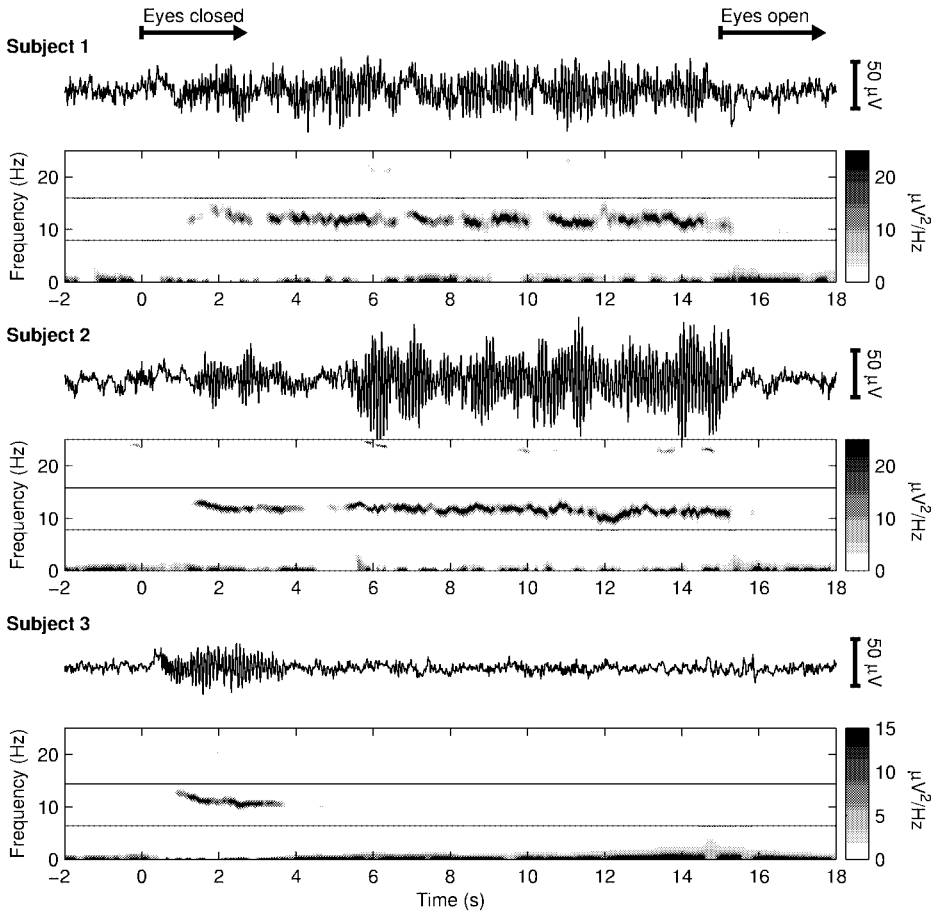

Figure 6.11: Typical ERS/ERD samples for the three selected subjects and the corresponding time-varying Kalman smoother spectra. Stimulus occurrence times (0 and 15 seconds) instructing subjects to close and open their eyes are marked on the top. Individually adjusted alpha frequency bands are marked with horizontal lines on top of each spectrum. The band width is set to 8 Hz.

6.5.3 Tracking of ERS/ERD transition dynamics

The ERS/ERD dynamics of all measured EEG samples were then estimated with the Kalman smoother approach. The results for three selected subject are presented in Figs. 6.11 and 6.12. Each selected subject had different characteristic patterns of alpha rhythms. Typical ERS/ERD sample and the corresponding Kalman smoother spectrum for each subject is presented in Fig. 6.11. For sub-

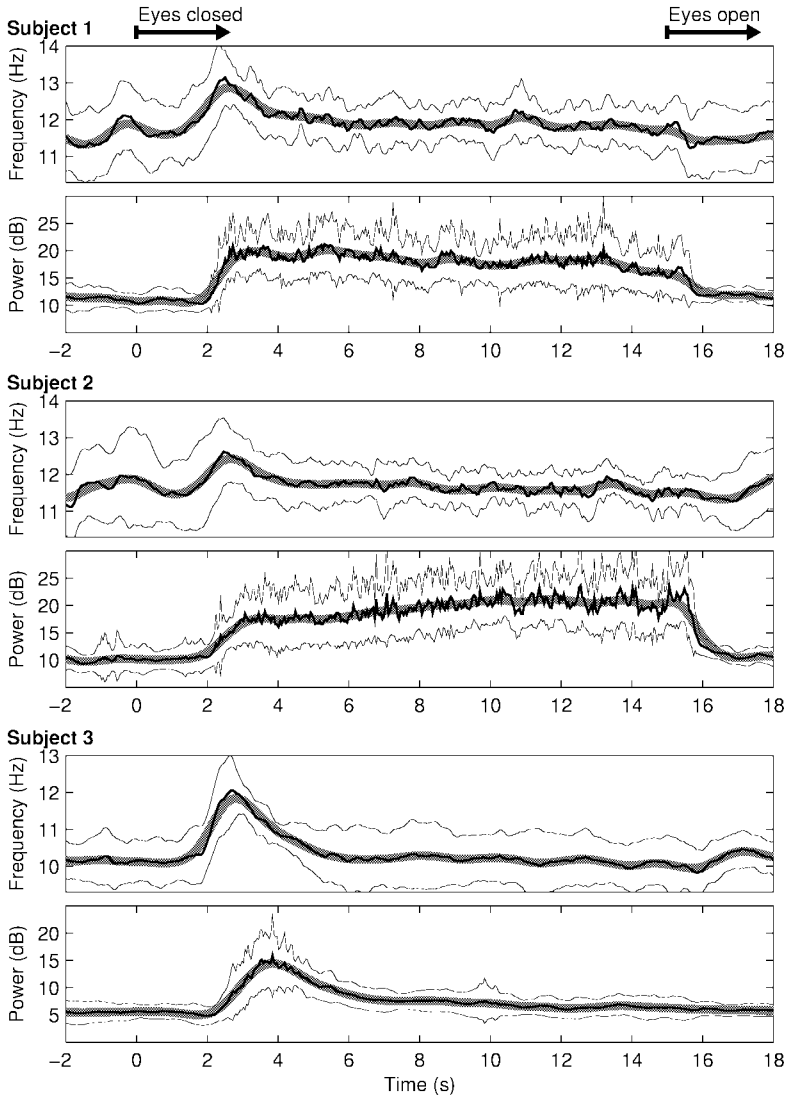

Figure 6.12: Average variation of the center frequency and band power of the alpha band for the three selected subjects. Mean values over the 19 ERS/ERD samples (—), estimated trends (═), and SD intervals (—) are presented. Stimulus occurrence times (0 and 15 seconds) instructing subjects to close and open their eyes are marked on the top.

ject 1 the power of alpha rhythm is quite invariant during the whole eyes closed period while for subject 3 the alpha power attenuates within few seconds after eye closure. For subject 2, on the other hand, a slow increase of alpha power after eye closure seems to be characteristic. The frequency band limits for alpha rhythm in Fig. 6.11 were adjusted based on the individual center frequencies. The center frequency was determined as the mean peak frequency of the spectrum during eye closure. Obtained center frequencies were 12.06, 11.69, and 10.69 Hz for subjects 1, 2, and 3, respectively. The band width was set to 8 Hz to ensure the complete involvement of the "squeak" phenomenon.

The average ERS/ERD dynamics for each subject was then evaluated by extracting the time-variation of the center frequency and power of alpha rhythm from the Kalman smoother spectra. The center frequency was defined as the frequency bisecting the power within the alpha band and the power was obtained by simply integrating the spectrum over the alpha band. Average center frequencies and band powers over the 19 consecutive ERS/ERD samples for each subject are presented in Fig. 6.12 along with estimated trends and SD intervals. The trend was estimated with the smoothness priors based approach presented in Section 2.5.1.

A common trend in the center frequency of alpha rhythm is observed among the subjects. Shortly after the eye closure center frequency reaches its maximum and then starts to decrease. After a while the frequency seems to reach a constant level which can be thought of as the individual characteristic alpha rhythm frequency. The power of alpha rhythm, on the other hand, increases rapidly after eye closure but reaches its maximum a bit later when the center frequency has already started to decrease. After 15 seconds when the eyes are opened a rapid decrease in alpha band power is observed for subjects 1 and 2. For subject 1 the power seems to start decreasing before the eyes are opened which may be due to expectation or anticipation of the upcoming stimuli [145]. For subject 3, on the other hand, the alpha rhythm power has already been attenuated during eyes closed period.

6.5.4 Statistics of Kalman smoother spectrum estimates

The statistics of the Kalman smoother spectrum estimates can be considered as follows. The estimation errors of the ARMA(6,2) model parameters at time t, denoted $\tilde{\theta}_t$, are assumed to be jointly Gaussian with mean zero and covariance $C_{\tilde{\theta}_t}$. The covariance $C_{\tilde{\theta}_t}$ is calculated at every step of the Kalman smoother algorithm according to (2.106) and, thus, the distribution of $\tilde{\theta}_t$ is known for every t. Values from this distribution can be generated as follows. Let x be a Gaussian random variable with mean zero and variance 1, i.e. $x \sim \mathcal{N}(0,1)$, and assume that the covariance matrix $C_{\tilde{\theta}_t}$ can be written in the form $C_{\tilde{\theta}_t} = LL^T$. Then according to equations (2.17) and (2.19) samples from the distribution of $\tilde{\theta}_t$ are given by Lx. The matrix L can be found by using Cholesky decomposition.

Let us consider the Kalman smoother spectrum of the ERS sample shown in Fig. 6.9. Given the ARMA parameter estimates $\hat{\theta}_t$ and error covariances $C_{\tilde{\theta}_t}$ at every time instant t, noisy parameter estimates can be generated as described

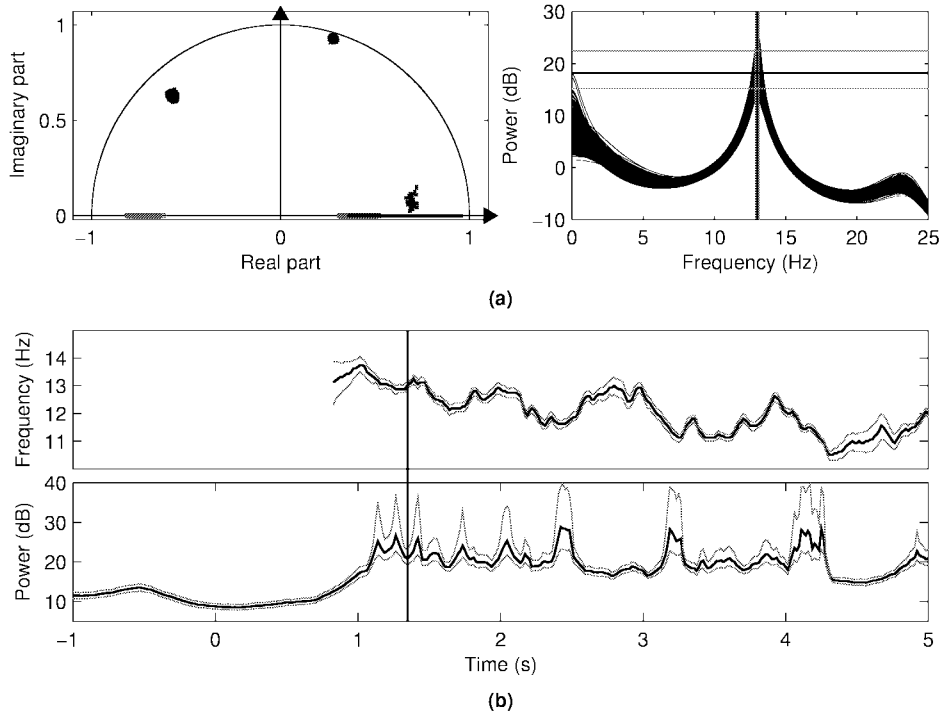

Figure 6.13: Statistics of the Kalman smoother spectrum estimate. (a) The distribution of the ARMA(6,2) model roots and the corresponding spectra for 1000 noisy parameter estimates generated from the Gaussian distribution (see text) at time $t = 1.35$. The means (—) and 95% confidence intervals (---) for peak frequency and power are indicated. (b) The time variation of the peak frequency and alpha band power (—) and the 95% confidence intervals (---).

above. From the noisy estimates, roots of AR and MA polynomials and corresponding spectra can be calculated. In Fig. 6.13 (a), the roots and spectra at time instant $t = 1.35$ s for 1000 noisy parameter estimates are presented. The mean peak frequency and power and the 95% confidence intervals are shown for the peak corresponding the alpha rhythm. Instead of the peak power, one is often more interested in the power of a specific band, here the alpha band (8–16 Hz). The peak frequency and band power statistics were calculated for every time instant t and the results are shown in Fig. 6.13 (b). On average, the 95% confidence interval of the peak frequency is about 0.18 Hz and the confidence interval of the band power is about 2.5 dB.

6.6 Discussion

In this chapter, the Kalman filtering algorithm along with a fixed-interval smoother was applied to tracking of nonstationary EEG. The presented approach was first proposed in [173]. Kalman filter has been previously used in EEG analysis in, e.g., [67, 17, 68, 8], but Kalman smoother, on the other hand, has not been used earlier for analysis of EEG. Compared to other adaptive algorithms such as RLS or LMS the most significant benefit of the Kalman smoother is the avoidance of the time-lag in the estimates.

In addition, due to the properties of parametric spectral estimation methods, the frequency resolution of Kalman smoother is better for narrow band processes than that of the classical FFT-based methods. In Section 6.5.4, the statistics of the peak frequency of the Kalman smoother spectrum presented in Fig. 6.9 were calculated. As a result, it was observed that the uncertainty of the observed peak frequency is in 95% confidence less than 0.18 Hz, whereas the frequency resolution of the corresponding spectrogram in Fig. 6.9 was about 1 Hz.

In the present study, an ARMA model was used as a model for nonstationary EEG. ARMA model has more degrees of freedom than AR model and has, therefore, better ability to generate diverse spectral shapes. The shape of the spectrum also depends on the selected model orders. Too low a model order may result in a too smooth spectrum and, on the other hand, too high a model order may produce spurious components in the spectrum. Some common model order selection criteria for the stationary case were given in Section 3.4, but they can hardly be applied to the time-varying case. Some approaches for the model order selection problem in nonstationary case have been proposed, e.g., in [50, 59]. However, based on our experience, the ARMA model of order (6,2) is suitable for modeling nonstationary EEG.

One problem in terms of application is how to set the state noise covariance coefficient that adjusts the adaptation speed of the Kalman smoother. In the selection of this coefficient a trade-off between the adaptation speed and the estimate variance need to be done. In other words, the improvement in the tracking properties is achieved with the expense of increased estimate variance. Here, a value $\sigma_w^2 = 0.0001$ was used for the update coefficient. The selection was made based on the conducted realistic EEG simulation and on the visual inspection of the estimates for real EEG data. Generally, the initialization of adaptive algorithms is a widely studied fundamental problem. In the case of EEG, probably the first attempt for an approach to find an optimal update coefficient for Kalman filter was made in [17]. However, there is no general solution for this problem. The measurement noise covariance coefficient, on the other hand, was set to $\sigma_e^2 = 1$. This selection is not, however, essential since only the ratio σ_e^2/σ_w^2 has effect on the estimates. Furthermore, the initial guesses for the state θ_0 and error covariance $C_{\tilde{\theta}_0}$ only affect on the initialization time (i.e. the time elapsed while the initial guesses converge near the true values) of the algorithm and, therefore, are not essential when sufficient amount of data before the point of interest is available. Here, θ_0 was set to zero and $C_{\tilde{\theta}_0}$ equal to identity matrix.

The results of tracking the ERS/ERD dynamics for three subjects were presented in Figs. 6.11 and 6.12. The main benefit of the presented method over the traditional ERS/ERD quantification based on bandpass filtering is the improved frequency resolution. Using the Kalman smoother approach the "squeak" effect of alpha rhythm seen in Figs. 6.7 and 6.12 for averaged estimates can be observed even from single sample spectrum estimates (see Figs. 6.8 and 6.11). With the classical spectrogram, on the other hand, this effect can not be observed from a single sample due to the poor time-frequency resolution (Fig. 6.8). However, by averaging spectrograms of several consecutive ERS/ERD samples the "squeak" can be observed (Fig. 6.7). The short-term "squeak" effect can not be observed from the RLS or LMS spectra either because of the unavoidable tracking lag. In addition, the applicability of the Kalman smoother spectrum estimation method in case of short period power changes was shown in Fig. 6.10.

Although "squeak" effect *per se* has been suggested as clinically meaningless [197], the accuracy and usability of the Kalman smoother in the spectral analysis of event-related EEG changes makes it a promising analysis method, e.g., for cognitive ERS/ERD experiments. The high time-frequency resolution of the Kalman smoother could enable the spectral analysis of single ERS/ERD samples. This property is crucial in some cognitive tasks where the transition can not be assumed to recur alike from time to time and, therefore, averaging of all trials would not be an optimal analysis method.

Chapter VII

Analysis of cardiovascular variability signals

This chapter is concerned with heart rate and blood pressure variability signals. The origin of these variability signals, i.e. the influence of different control systems on heart rate and blood pressure, is discussed and the construction of the two variability time series is described. A special emphasis is laid on the importance of preprocessing, and an advanced detrending procedure originally proposed in [176] is presented. In addition, the basic time- and frequency-domain analysis methods as well as modern methods for assessing baroreceptor reflex sensitivity are summarized. During the preparation of this thesis, analysis softwares for HRV and BPV signals including the presented methods were developed. The software was developed using Matlab® (The MathWorks Inc.). The aim of this chapter is to summarize the methodological framework of these software and not to give a detailed documentation for the software.

7.1 Introduction

The main task of the cardiovascular system is to provide sufficient amount of blood delivering nutrients and oxygen for tissues and vital organs and it also participates on body temperature regulation. The work is mainly carried out by the left ventricle of the heart which pumps blood through the aorta into greater circulation. The blood flow into the aorta after contraction is faster than the drain through the arterioles and, therefore, the pressure in the aorta increases. The maximum pressure during systole (*systolic blood pressure*, SBP) is determined mainly by the strength of the contraction and the distensibility of the aortic walls. After systole, the aortic valves are closed and blood flows to peripheral circulation with a rate depending on the pressure difference between the aorta and periphery. The systemic pressure is determined by the relationship between cardiac output and total peripheral resistance.

In different conditions, sufficient blood flow is obtained due to elaborate interacting control systems. The rhythm of the heart is controlled by the *sinoatrial* (SA) node, which is modulated by both the sympathetic and parasympathetic branches of the autonomic nervous system. Sympathetic activity tends to increase heart rate (HR↑) and its response is slow (few seconds) [12]. Sympathetic in-

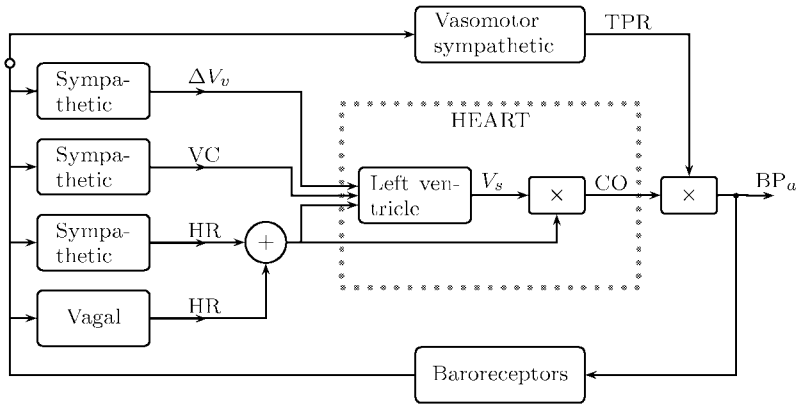

Figure 7.1: The four baroreflex pathways (redrawn from [162]). Variation in venous volume (ΔV_v), left ventricular contractility (VC), sympathetic and parasympathetic (vagal) control of heart rate (HR), stroke volume (V_s), cardiac output (CO), total peripheral resistance (TPR), and arterial blood pressure (BP_a).

nervation covers also arterial walls and causes vasoconstriction, e.g. in physical exertion the vessels of most internal organs contract. Parasympathetic activity, on the other hand, tends to decrease heart rate (HR↓) and mediates faster (0.2 0.6 seconds) [12]. In addition to central control, there are some feedback mechanisms that can provide quick reflexes. One such mechanism is the arterial baroreflex. This reflex is based on baroreceptors which are located on the walls of some large vessels and can sense the stretching of vessel walls caused by pressure increase. Both sympathetic and parasympathetic activity are influenced by baroreceptor stimulation trough a specific baroreflex arc, Fig. 7.1.

The continuous modulation of the sympathetic and parasympathetic innervations results in variations in both heart rate and blood pressure. The most conspicuous periodic component of HRV is the so-called *respiratory sinus arrhythmia* (RSA) which is considered to range from 0.15 to 0.4 Hz [12]. In addition to the physiological influence of breathing on HRV, this *high frequency* (HF) component is generally believed to be of parasympathetic origin. Another widely studied component of HRV is the *low frequency* (LF) component usually ranging from 0.04 to 0.15 Hz including the component referred to as the 10-second rhythm or the Mayer wave [12]. The rhythms within the LF band have been thought to be of both sympathetic and parasympathetic origin [12] even though some researchers have suggested them to be mainly of sympathetic origin [107]. The fluctuations below 0.04 Hz, on the other hand, have not been studied as much as the higher frequencies. These frequencies are commonly divided into *very low frequency* (VLF, 0.003-0.04 Hz) and *ultra low frequency* (ULF, 0-0.003 Hz) bands,

but in case of short-term recordings the ULF band is generally omitted [178]. These lowest frequency rhythms are characteristic for HRV and BPV signals and have been related to, e.g., humoral factors such as the thermoregulatory processes and renin-angiotensin system [12].

The interdependencies between HR, BP, and respiration has lead into studies where the interactions of the signals have been modeled using parametric multivariate models [93, 94]. These models can be divided into open- and closed-loop models. The simplest such model is the multivariate AR model, which is a closed-loop model. Utilization of such a model can provide additional information from the system, for example, through partial spectrum representation.

Even though HRV has been studied extensively during the last decades within which numerous research articles have been published, the practical use of HRV have reached general consensus only in two clinical applications [178]. That is, it can be used as a predictor of risk after myocardial infarction [104, 65] and as an early warning sign of diabetic neuropathy [18, 129]. In addition, HRV has been found to correlate with, e.g., age, mental and physical stress, and attention, see, e.g., the review in [12].

In this chapter, the origin and determination of cardiovascular time series are shortly discussed and the most common time- and frequency-domain analysis methods are reviewed. The importance of removing nonstationarities like slow linear or more complex trends from these time series is particularly emphasized and an advanced detrending method originally presented in [176] is given.

7.2 Materials and experimental procedures

In this chapter, data from three different sources are used. The effect of the detrending method is tested with the passive oddball paradigm data included in the first data set addressed in Section 1. The orthostatic test recording, on the other hand, was carried out in the Department of Applied Physics, University of Kuopio and the measurement used in the demonstration of baroreflex estimation in the Brain@Work Laboratory, Department of Occupational Medicine, Finnish Institute of Occupational Health. In all of the measurements, ECG was recorded using a NeuroScan measurement device (Compumedics Limited) with 500 Hz sampling frequency. The blood pressure recordings were made with a Portapres system (TNO Biomedical Instrumentation) which measures BP continuously from fingertip using the volume-clamp method (also known as the method of Penaz). The sampling frequency of the Portapres was 200 Hz.

7.3 Cardiovascular variability signals

In this section, the formulation of HRV and BPV signals is presented. The term HRV refers, in general, to changes in heart beat interval which is a reciprocal of the heart rate. The starting point for HRV analysis is the ECG recording from which the HRV time series can be extracted. Correspondingly for the BPV analysis, beat-to-beat information of *systolic*, *mean*, and *diastolic blood pressure*

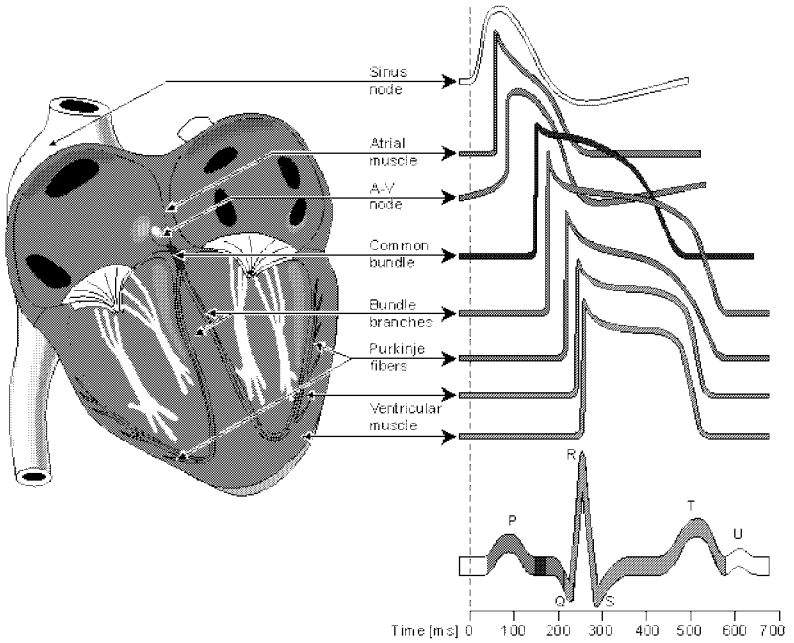

Figure 7.2: Electrophysiology of the heart (redrawn from [108]). The different waveforms for each of the specialized cells found in the heart are shown. The latency shown approximates that normally found in the healthy heart.

values (SBP, MBP, and DBP respectively) are required. In the formulation of the above cardiovascular variability signals, a fundamental issue is the determination of heart beat period.

7.3.1 Heart beat period and QRS detection

The aim in HRV analysis is to examine the sinus rhythm modulated by the autonomic nervous system. Therefore, one should technically detect the occurrence times of the SA-node action potentials. This is, however, practically impossible and, thus, the fiducial points for the heart beat is usually determined from the ECG recording. The nearest observable activity in the ECG compared to SA-node firing is the P-wave resulting from atrial depolarization (see Fig. 7.2) and, thus, the heart beat period is generally defined as the time difference between two successive P-waves. The signal-to-noise ratio of the P-wave is, however, clearly lower than that of the strong QRS complex which results primarily from ventricular depolarization. Therefore, the heart beat period is commonly evaluated as the time difference between the easily detectable QRS complexes.

A typical QRS detector consists of a preprocessing part followed by a decision

rule. Several different QRS detectors have been proposed within last decades [180, 131, 132, 56, 44]. For an easy to read review of these methods, see [2]. The preprocessing of the ECG usually includes at least bandpass filtering to reduce power line noise, baseline wander, muscle noise, and other interference components. The passband can be set to approximately 5–30 Hz which covers most of the frequency content of QRS complex [131]. In addition, preprocessing can include differentiation and/or squaring of the samples. After preprocessing, the decision rules are applied to determine whether or not a QRS complex has occurred. The decision rule usually includes an amplitude threshold which is adjusted adaptively as the detection progresses. In addition, the average heart beat period is often used in the decision. For other approaches on QRS detection, see, e.g., [203, 74]. The fiducial point is generally selected to be the R-wave and the corresponding time instants are given as the output of the detector.

The accuracy of the R-wave occurrence time estimates is often required to be 1–2 ms and, thus, the sampling frequency of the ECG should be at least 500–1000 Hz [178]. If the sampling frequency of the ECG is less than 500 Hz, the errors in R-wave occurrence times can cause critical distortion to HRV analysis results, especially to spectrum estimates [114]. The distortion of the spectrum is even bigger if the overall variability in heart rate is small [146]. The estimation accuracy can, however, be improved by interpolating the QRS complex, e.g., by using a cubic spline interpolation [29]. It should be, however, noted that when the SA-node impulses are of interest there is an unavoidable estimation error of approximately 3 ms due to fluctuations in the AV-nodal conduction time [162].

7.3.2 Derivation of cardiovascular time series

After the QRS complex occurrence times have been estimated, the HRV and BPV time series can be derived as described in Fig. 7.3, where short samples of ECG and BP signals are plotted one upon the other. The inter-beat intervals or RR intervals are obtained as differences between successive R-wave occurrence times, i.e. $\mathrm{RR}_n = t_n - t_{n-1}$. The time series constructed from all available RR intervals is, clearly, not equidistantly sampled, but have to be presented as a function of time, i.e. as values (t_n,RR_n). In some context, normal-to-normal (NN) may also be used when referring to these intervals indicating strictly intervals between successive QRS complexes resulting from SA-node depolarization [178]. In practice, the NN and RR intervals appear to be the same and throughout this thesis the term RR is preferred.

Correspondingly, the BP time series are determined as pressure values as a function of R-wave times. For each beat SBP, MBP, and DBP values can be extracted as shown in Fig. 7.3. The mean pressure is the average pressure level within the heart period and it corresponds to the line dividing the BP signal into two equal parts ($A_1 = A_2$ in Fig. 7.3). The resulting pressure series are those of (t_n,SBP_n), (t_n,MBP_n), and (t_n,DBP_n). The construction of the time series and the correspondence of the RR interval and BP values adopted here conform to those given in [34, 119, 79] but also different approaches have been used [162, 92].

One characteristic property of the above time series that has to be considered

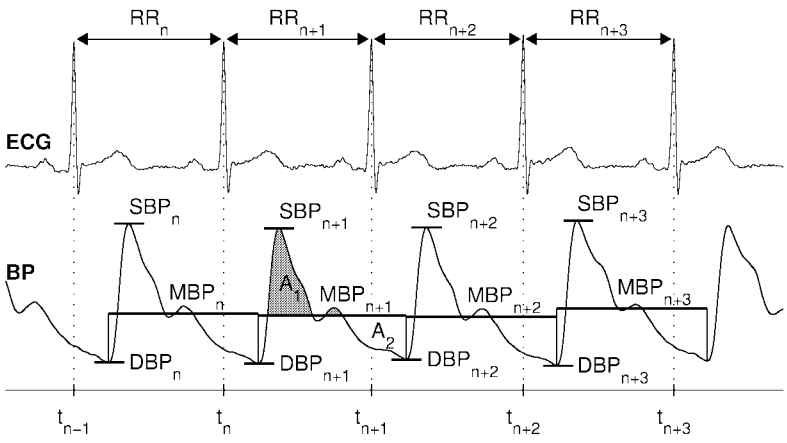

Figure 7.3: Construction of RR interval and systolic, mean, and diastolic BP time series from ECG and BP signals.

prior to frequency-domain analysis is the fact that they are non-equidistantly sampled. In general, three different approaches have been used to get around this issue [178]. The simplest approach that have been adopted in, e.g., [11] is to assume equidistant sampling and calculate the spectrum directly from the RR interval tachogram (RR intervals as a function of beat number), see the left panel of Fig. 7.4. This assumption can, however, cause distortion into the spectrum [111]. This distortion becomes substantial when the variability is large in comparison with the mean level. Furthermore, the spectrum can not be considered to be a function of frequency but rather of cycles per beat [32]. Another common approach, adopted here, is to use interpolation methods for converting the non-equidistantly sampled RR interval time series (also called the interval function) to equidistantly sampled [178], see the right panel of Fig. 7.4. One choice for the interpolation method is the cubic spline interpolation [111]. After interpolation, regular spectrum estimation methods can be applied. The third general approach called the spectrum of counts considers a series of impulses (delta functions positioned at beat occurrence times) [33]. This approach relies on the generally accepted *integral pulse frequency modulator* (IPFM) which aims to model the neural modulation of the SA-node [162]. According to this model, the modulating signal is integrated until a reference level is achieved after which an impulse is emitted and the integrator is set to zero. The spectrum of the series of events can be calculated, e.g., by first lowpass filtering the event series and then calculating the spectrum of the resulting signal [32].

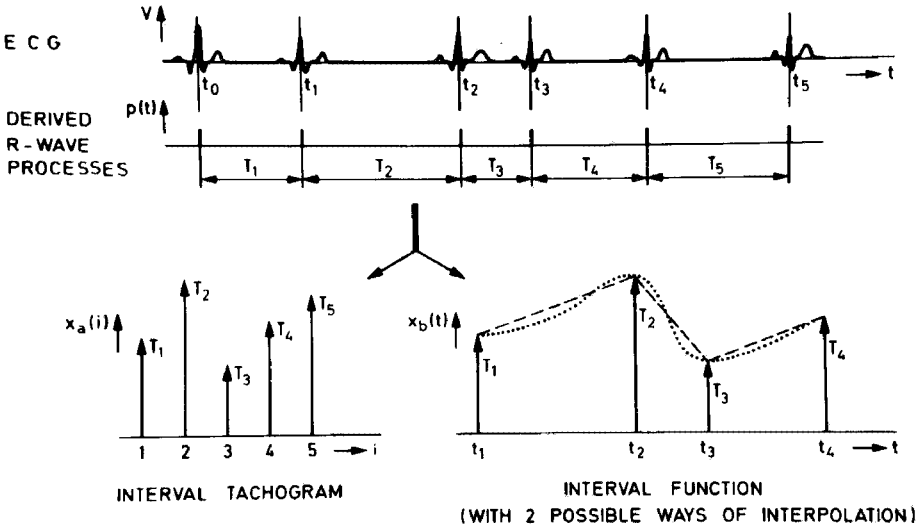

Figure 7.4: Derivation of two HRV signals from ECG (redrawn from [162]): the interval tachogram (left panel) and the interval function (right panel).

7.4 Preprocessing of cardiovascular time series

Any artifact in the RR interval or BP time series may interfere the analysis of these signals. The artifacts within cardiovascular signals can be divided into technical and physiological artifacts. The technical artifacts can include missing or additional QRS complex detections, errors in R-wave occurrence times, and errors in BP values. These artifacts may be due to measurement artifacts or the computational algorithm. One striking technical artifact within continuous BP measurements arises from the calibration pauses of the Portapres device, occurring approximately every 70 heart beats. A correction procedure for recovering these pauses was described in [85]. The physiological artifacts, on the other hand, include ectopic beats and arrhythmic events. In order to avoid the interference of such artifacts, the ECG or BP recordings and the corresponding event series should always be manually checked for artifacts and only artifact-free sections should be included in the analysis [178]. Alternatively, if the amount of artifact-free data is insufficient, proper interpolation methods can be used to reduce these artifacts, see, e.g., [99, 100, 112].

Another common feature that can alter the analysis significantly are the slow linear or more complex trends within the analyzed time series. Such slow nonstationarities are characteristic for cardiovascular variability signals and should be considered before the analysis. The origins of nonstationarities in HRV are discussed, e.g., in [12]. Two kinds of methods have been used to get around the

nonstationarity problem. In [195], it was suggested that HRV data should be systematically tested for nonstationarities and that only stationary segments should be analyzed. Representativeness of these segments in comparison with the whole HRV signal was, however, questioned in [52]. Other methods try to remove the slow nonstationary trends from the HRV signal before analysis. The detrending is usually based on first order [101, 115] or higher order polynomial [149, 115] models. Here, an advanced detrending procedure originally presented in [176] is described. The approach is based on smoothness priors regularization which was discussed in Section 2.5.1.

7.4.1 Smoothness priors based detrending approach

Let $x \in \mathbb{R}^N$ denote the RR interval time series which can be considered to consist of two components

$$x = x_{\text{stat}} + x_{\text{trend}} \tag{7.1}$$

where x_{stat} is the nearly stationary RR interval series of interest and x_{trend} is the low frequency aperiodic trend component. Suppose that the trend component can be modeled with a linear observation model as

$$x_{\text{trend}} = H\theta + e \tag{7.2}$$

where $H \in \mathbb{R}^{N\times p}$ is the observation matrix, $\theta \in \mathbb{R}^p$ are the regression parameters, and e is the observation error. The task is then to estimate the parameters by some fitting procedure so that $\hat{x}_{\text{trend}} = H\hat{\theta}$ can be used as the estimate of the trend. The properties of the estimate depend strongly on the properties of the basis vectors (columns of the matrix H) in the fitting. A widely used method for the solution of the estimate $\hat{\theta}$ is the least squares method. However, a more general approach for the estimation of $\hat{\theta}$ is used here. That is, the so-called regularized least squares solution

$$\hat{\theta}_\kappa = \arg\min_\theta \left\{ \|x - H\theta\|^2 + \kappa^2 \|D_d(H\theta)\|^2 \right\} \tag{7.3}$$

where κ is the regularization parameter and D_d indicates the discrete approximation of the d'th derivative operator. This is clearly a modification of the ordinary least squares solution to the direction in which the side norm $\|D_d(H\theta)\|$ gets smaller. In this way, prior information about the predicted trend $H\theta$ can be implemented to the estimation. The solution of (7.3) can be written in the form (see Section 2.5.1)

$$\hat{\theta}_\kappa = (H^T H + \kappa^2 H^T D_d^T D_d H)^{-1} H^T x \tag{7.4}$$

and the estimate for the trend which is to be removed as

$$\hat{x}_{\text{trend}} = H\hat{\theta}_\kappa. \tag{7.5}$$

The selection of the observation matrix H can be implemented according to some known properties of the data x. For example, a generic set of Gaussian shaped functions or sigmoids can be used. Here, however, the trivial choice of

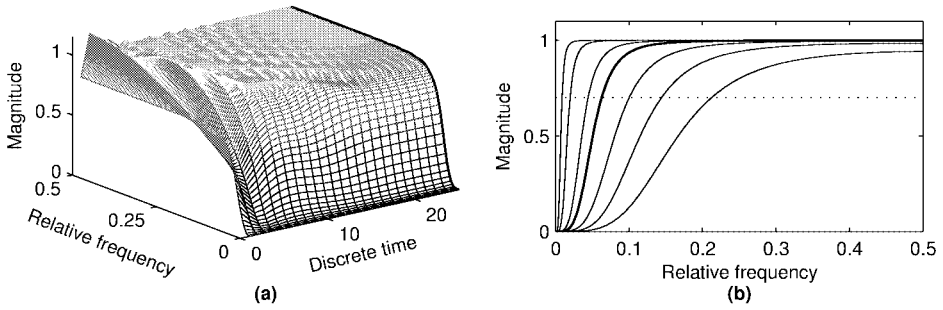

Figure 7.5: a) Time-varying frequency response of $\mathcal{L}$ ($N - 1 = 50$ and $\lambda = 10$). Only the first half of the frequency response is presented, since the other half is identical. b) Frequency responses, obtained from the middle row of $\mathcal{L}$ (cf. bold lines), for $\lambda = 1$, 2, 4, 10, 20, 100, and 500. The corresponding cut-off frequencies are 0.213, 0.145, 0.101, 0.063, 0.045, 0.021 and 0.010 times the sampling frequency.

identity matrix $H = I \in \mathbb{R}^{N \times N}$ is used. In this case, the regularization part of (7.3) can be understood to draw the solution towards the null space of the regularization matrix D_d. The null space of the second order difference matrix given in (2.37) contains all first order curves and, thus, D_2 is a good choice for estimating the aperiodic trend of RR series. With these specific choices, the detrended nearly stationary RR series can be written as

$$\hat{x}_{\text{stat}} = x - H\hat{\theta}_\kappa = (I - (I + \kappa^2 D_2^T D_2)^{-1})x. \tag{7.6}$$

In order to demonstrate the properties of the proposed detrending method, its frequency response is considered. Equation (7.6) can be written as $\hat{x}_{\text{stat}} = \mathcal{L}x$, where $\mathcal{L} = I - (I + \kappa^2 D_2^T D_2)^{-1}$ corresponds to a time-varying finite impulse response highpass filter. The frequency response of $\mathcal{L}$ for each discrete time point, obtained as a Fourier transform of its rows, is presented in Fig. 7.5 (a). It can be seen that the filter is mostly constant but the beginning and end of the signal are handled differently. The filtering effect is attenuated for the first and last elements of x and, thus, the distortion of end points of data is avoided. The effect of the smoothing parameter κ on the frequency response of the filter is presented in Fig. 7.5 (b). The cutoff frequency of the filter decreases when κ is increased. Besides the κ parameter the frequency response naturally depends on the sampling rate of signal x.

7.5 Analysis methods of HRV

Next, a short review of measures used in the analysis of short-term HRV recordings is given. The selection of the presented measures is based on the guidelines given in [178]. Even though most of these measures have been derived for HRV,

several of them can be as well applied for analyzing BPV recordings. The analysis methods of HRV can be roughly divided into time-domain, frequency-domain, and nonlinear methods. In addition, time-varying methods such as time-frequency representations have been utilized. The presented HRV measures are summarized in Table 7.1.

7.5.1 Time-domain methods

The time-domain methods are the simplest to perform since they are applied straight to the series of successive RR interval values. The most evident such measure is the mean value of RR intervals ($\overline{\mathrm{RR}}$) or, correspondingly, the mean HR ($\overline{\mathrm{HR}}$). In addition, several variables that measure the variability within the RR series exist. The standard deviation of RR intervals (SDNN) is defined as

$$\mathrm{SDNN} = \sqrt{\frac{1}{N-1}\sum_{j=1}^{N}(\mathrm{RR}_j - \overline{\mathrm{RR}})^2} \tag{7.7}$$

where RR_j denotes the value of j'th RR interval and N is the total number of successive intervals. The SDNN reflects the overall (both short-term and long-term) variation within the RR interval series, whereas the standard deviation of successive RR interval differences (SDSD) given by

$$\mathrm{SDSD} = \sqrt{E\{\Delta\mathrm{RR}_j^2\} - E\{\Delta\mathrm{RR}_j\}^2} \tag{7.8}$$

can be used as a measure of the short-term variability. For stationary RR series $E\{\Delta\mathrm{RR}_j\} = E\{RR_{j+1}\} - E\{RR_j\} = 0$ and SDSD equals the root mean square of successive differences (RMSSD) given by

$$\mathrm{RMSSD} = \sqrt{\frac{1}{N-1}\sum_{j=1}^{N-1}(\mathrm{RR}_{j+1} - \mathrm{RR}_j)^2}. \tag{7.9}$$

Another measure calculated from successive RR interval differences is the NN50 which is the number of successive intervals differing more than 50 ms or the corresponding relative amount

$$\mathrm{pNN50} = \frac{\mathrm{NN50}}{N-1} \times 100\%. \tag{7.10}$$

The properties of RMSSD and pNN50 were compared in [46], where a modified RMSSD index that is more robust to artifacts and does not saturate like pNN50 was proposed.

In addition to the above statistical measures, there are some geometric measures that are calculated from the RR interval histogram. The HRV triangular index is obtained as the integral of the histogram (i.e. total number of RR intervals) divided by the height of the histogram which depends on the selected bin

width. In order to obtain comparable results, a bin width of 1/128 seconds is recommended [178]. Another geometric measure is the TINN which is the baseline width of the RR histogram evaluated through triangular interpolation, see [178] for details.

7.5.2 Frequency-domain methods

In the frequency-domain methods, a power spectrum estimate is calculated for the RR interval series. The regular PSD estimators implicitly assume equidistant sampling and, thus, the RR interval series should be converted to equidistantly sampled series by interpolation methods prior to PSD estimation. In HRV analysis, the PSD estimation is generally carried out using either FFT based methods or parametric AR modeling based methods, see Section 3.5. The advantage of FFT based methods is the simplicity of implementation, while the AR spectrum yields improved resolution especially for short samples. Another property of AR spectrum that has made it popular in HRV analysis is that it can be decomposed into separate spectral components as described in Section 3.5.3. The disadvantages of the AR spectrum are the complexity of model order selection and the contingency of negative components. Nevertheless, it may be advantageous to calculate the spectrum with both methods to have comparable results.

The generalized frequency bands in case of short-term HRV recordings are the very low frequency (VLF, 0–0.04 Hz), low frequency (LF, 0.04–0.15 Hz), and high frequency (HF, 0.15–0.4 Hz). The frequency-domain measures extracted from the PSD estimate for each frequency band include absolute and relative powers of VLF, LF, and HF bands, LF and HF band powers in normalized units, the LF/HF power ratio, and peak frequencies for each band (see Fig. 7.6 and Table 7.1). In the case of FFT spectrum, absolute power values for each frequency band are obtained by simply integrating the spectrum over the band limits. In the case of AR spectrum, on the other hand, distinct spectral components emerge for each frequency band with a proper selection of the model order and the absolute power values are obtained directly as the powers of these components as described in equations (3.56)-(3.57). The band powers in relative and normalized units are obtained from the absolute values as described in Table 7.1.

7.5.3 Nonlinear methods

Considering the complex control systems of the heart it is reasonable to assume that nonlinear mechanisms are involved in the genesis of HRV. The nonlinear properties of HRV have been analyzed using measures such as Poincaré plot [19, 21], approximate entropy [154, 45], detrended fluctuation analysis [141, 142], correlation dimension [55, 61], and Lyapunov exponent [186, 61], see Table 7.1. During the last years, the number of studies utilizing such methods have increased substantially. The downside of these methods is still, however, the difficulty of physiological interpretation of the results.

One commonly used nonlinear method that is simple to interpret is the so-called Poincaré plot. It is a graphical representation of the correlation between

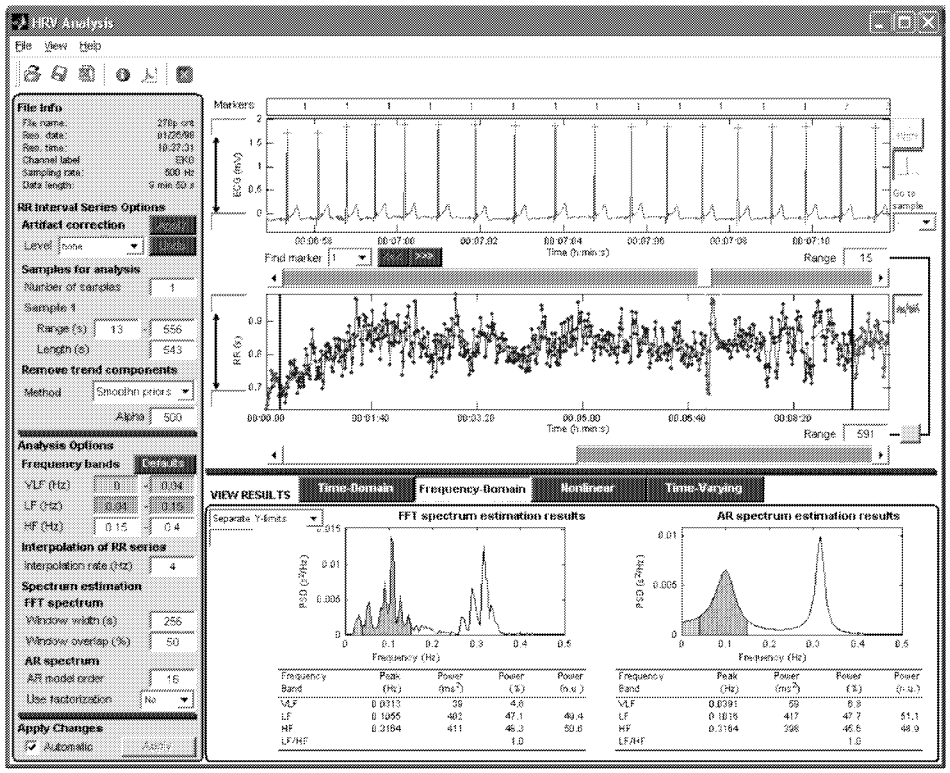

Figure 7.6: The user interface of the HRV analysis software, part of the Biosignal analysis software [1].

successive RR intervals, i.e. plot of RR_{j+1} as a function of RR_j as described in Fig. 7.7. The shape of the plot is the essential feature. A common approach to parameterize the shape is to fit an ellipse to the plot as shown in Fig. 7.7. The ellipse is oriented according to the line-of-identity ($\mathrm{RR}_j = \mathrm{RR}_{j+1}$) [19]. The standard deviation of the points perpendicular to the line-of-identity denoted by SD1 describes short-term variability which is mainly caused by RSA. It can be shown that SD1 is related to the time-domain measure SDSD according to [19]

$$\mathrm{SD1}^2 = \frac{1}{2}\mathrm{SDSD}^2. \tag{7.11}$$

The standard deviation along the line-of-identity denoted by SD2, on the other hand, describes long-term variability and has been shown to be related to time-domain measures SDRR and SDSD by [19]

$$\mathrm{SD2}^2 = 2\,\mathrm{SDRR}^2 - \frac{1}{2}\mathrm{SDSD}^2. \tag{7.12}$$

Table 7.1: Selected measures of HRV for short-term recordings. For each measure preferred units and a short description is given. In addition, related references are given for some measures

	Measure	Units	Description	References
Time-Domain	$\overline{RR}$	[ms]	The mean of RR intervals	
	$\overline{HR}$	[1/min]	The mean heart rate	
	SDNN	[ms]	Standard deviation of RR intervals	
	SDSD	[ms]	Standard deviation of successive RR interval differences	
	RMSSD	[ms]	Square root of the mean squared differences between successive RR intervals	
	NN50		Number of successive RR interval pairs that differ more than 50 ms	
	pNN50	[%]	NN50 divided by the total number of RR intervals	
	HRV triangular index		The integral of the RR interval histogram divided by the height of the histogram	[178]
	TINN	[ms]	Baseline width of the RR interval histogram	[178]
Frequency-Domain	VLF, LF, HF	[Hz]	VLF, LF, and HF band peak frequencies	
	VLF, LF, HF	[ms^2]	Absolute powers of VLF, LF, and HF bands	
	VLF, LF, HF	[%]	Relative powers of VLF, LF, and HF bands VLF [%] = VLF [ms^2]/total power [ms^2] $\times$ 100% LF [%] = LF [ms^2]/total power [ms^2] $\times$ 100% HF [%] = HF [ms^2]/total power [ms^2] $\times$ 100%	
	LF, HF	[n.u.]	Powers of LF and HF bands in normalized units LF [n.u.] = LF [ms^2]/(total power [ms^2] $-$ VLF [ms^2]) HF [n.u.] = HF [ms^2]/(total power [ms^2] $-$ VLF [ms^2])	
	LF/HF		Ratio between LF and HF band powers	
Nonlinear	SD1, SD2	[ms]	The standard deviation of the Poincaré plot perpendicular to (SD1) and along (SD2) the line-of-identity	[19, 21]
	ApEn		Approximate entropy	[154, 45]
	SampEn		Sample entropy	[154]
	K_2		Kolmogorov entropy	[55]
	DFA		Detrended fluctuation analysis	[141, 142]
	MED		Minimum embedded dimension	[152, 61]
	λ		Lyapunov exponents	[186, 61]
	D_2		Correlation dimension	[55, 61]
	RPA		Recurrence plot analysis	[194, 186, 207]
Time-varying spectrum estimation methods				[13, 125, 105, 86, 14, 192, 201, 182]

The standard Poincaré plot can be considered to be of the first order. The second order plot would be a three dimensional plot of values $(RR_j, RR_{j+1}, RR_{j+2})$. In addition, the lag can be bigger than 1, e.g., the plot (RR_j, RR_{j+2}).

7.5.4 Time-varying methods

As already mentioned, cardiovascular signals are often characterized by nonstationary trend components. In addition, the low and high frequency variability which one is usually interested in might also vary in time due to, e.g., change in

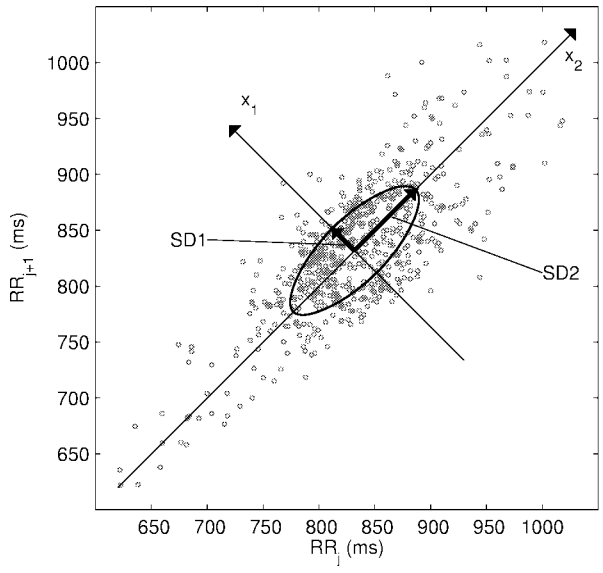

Figure 7.7: Poincaré plot analysis with the ellipse fitting procedure. SD1 and SD2 are the standard deviations in the directions x_1 and x_2, where x_2 is the line-of-identity for which $RR_j = RR_{j+1}$.

physiological conditions. For example, in the orthostatic test, subject stands up rapidly after lying supine for few minutes. After standing up, HR starts to increase to compensate the decrease in BP. On supine, the high frequency variation of HR is typically strong, often higher than the low frequency variation. At the instant of standing, an immediate strong decrease in HF variation and a more gradual increase in LF variation has been observed [86]. Such changes in HRV can be analyzed with time-varying spectrum estimation methods, see Fig. 7.8. The interest towards these methods has increased recently and they have been applied for monitoring different types of transient cardiac events [13, 125, 105, 86, 14, 192, 201, 182]. For example, HRV recording corresponding to an ischemic episode is usually characterized by a marked nonstationarity. In [13, 14], the spectral content of HRV during such episodes was analyzed dynamically by using a parametric time-varying AR model based spectrum estimation method.

7.6 Effect of detrending

Next, the influence of the low frequency trend components that are characteristic for RR interval series is considered by comparing HRV results obtained before and after detrending the RR series. The trends were removed using the smoothness priors based approach presented in Section 7.4. The performance of the detrending

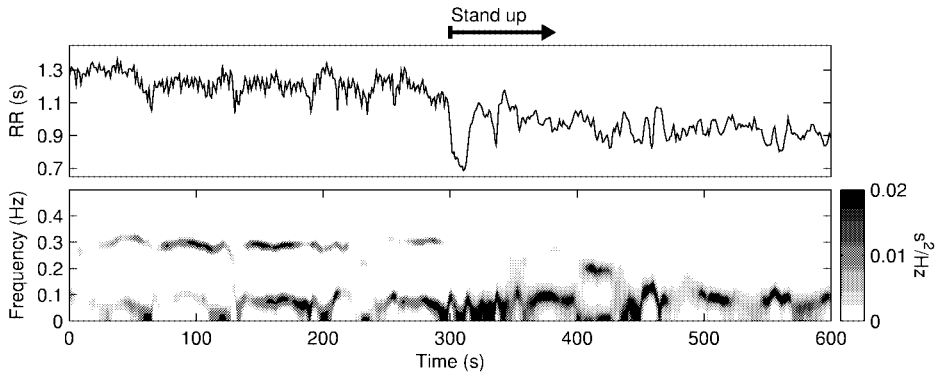

Figure 7.8: Time-varying spectrum of a RR series recorded during an orthostatic test. A 16'th-order AR model was used and the evolution of the model coefficients was solved using the Kalman smoother algorithm.

method on real RR interval data is presented in Fig. 7.9, where it is applied to data of four different subjects. Each RR series was first interpolated to obtain a regularly sampled series using a 4 Hz cubic interpolation. The detrending was then performed using a smoothing parameter $\kappa = 500$, which equals a cut-off frequency of 0.039 Hz. The four RR series with the fitted trends and the corresponding detrended series are presented in Fig. 7.9 (a).

Three different time-domain parameters SDNN, RMSSD, and pNN50, recommended in [178], were selected to demonstrate the effect of the used detrending method on time-domain analysis [Fig. 7.9 (b)]. SDNN, which describes the amount of overall variance of the RR series, is clearly effected the most. Instead only little effect is focused on RMSSD and pNN50 which both describe the variation between successive RR intervals.

The effect of detrending on frequency-domain analysis is presented in Fig. 7.9 (c), where PSD estimates calculated with Welch's periodogram method and by AR modeling before and after detrending are compared. AR model order $p = 16$ was selected according to [178], by using the corrected AIC criterion [53]. In each original PSD estimate the intensity of the VLF component is clearly stronger than the intensity of LF or HF component. Each spectrum is, however, limited to 0.035 s^2/Hz to enable the comparison of the spectra before and after detrending. For Welch's method the VLF components are properly removed while the higher frequencies are not significantly altered by the detrending. But when AR models of relatively low orders are used, which is usually desirable in HRV analysis in order to enable a distinct division of the spectrum into VLF, LF, and HF components, the effect of detrending is remarkable. In each original AR spectrum, the peak around 0.1 Hz is spuriously covered by the strong VLF component. However, in the AR spectra obtained after detrending the component near 0.1 Hz is more

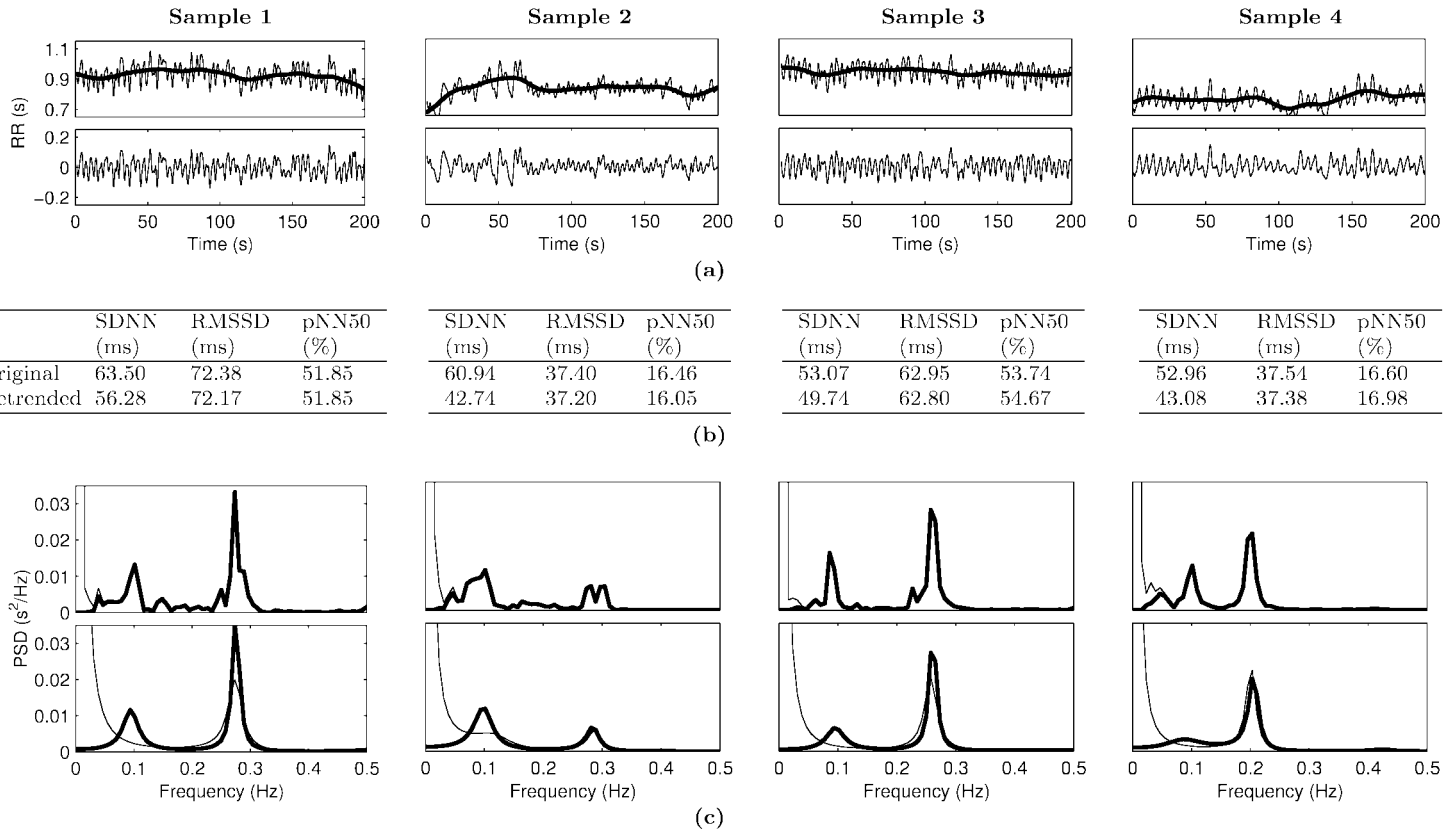

	SDNN (ms)	RMSSD (ms)	pNN50 (%)
Original	63.50	72.38	51.85
Detrended	56.28	72.17	51.85

	SDNN (ms)	RMSSD (ms)	pNN50 (%)
Original	60.94	37.40	16.46
Detrended	42.74	37.20	16.05

	SDNN (ms)	RMSSD (ms)	pNN50 (%)
Original	53.07	62.95	53.74
Detrended	49.74	62.80	54.67

	SDNN (ms)	RMSSD (ms)	pNN50 (%)
Original	52.96	37.54	16.60
Detrended	43.08	37.38	16.98

Figure 7.9: The effect of the detrending method on time- and frequency-domain analysis. (a) Original RR series and fitted trends (above) and detrended RR series (below). The duration of each data segment is 200 seconds. (b) The effect of the detrending on three time-domain parameters (SDNN, RMSSD, and pNN50). c) PSD estimates for original (—) and detrended (**—**) RR series with Welch's periodogram method (above) and by using a 16'th order AR model (below).

Figure 7.10: Sequence technique for estimation of the baroreflex sensitivity.

realistic when compared to the spectra obtained by Welch's method.

7.7 Baroreceptor reflex sensitivity

The arterial baroreceptor reflex or baroreflex has a fundamental role in maintaining blood pressure homeostasis and its impairment may result in exaggerated blood pressure fluctuations and an increased risk of cardiovascular morbid events. Thus, methods for assessing the gain of baroreflex control of heart rate, commonly referred to as *baroreflex sensitivity* (BRS), have been developed. In these methods, BRS is evaluated as the ratio between changes in HR and BP. Traditionally BRS has been evaluated by measuring the RR interval values in response to increase or decrease of systolic pressure induced by intravenous drug injection [136]. Drawbacks of the traditional method are that it has to carried out in laboratory environment and it yields only temporary estimates of BRS. With the modern techniques, on the other hand, BRS can be estimated from the spontaneous HR and BP fluctuations. The most common such techniques are the *sequence method* and the spectral methods. For other kind of approaches, see, e.g., [37, 87, 150].

7.7.1 Sequence method

Perhaps, the most popular modern BRS estimation technique is the so-called sequence method [155]. In this method, spontaneous sequences of three or more heart beats during which systolic BP increases and RR interval lengthens progressively (RR↑/SBP↑ sequences) or, vice versa, SBP decreases and RR interval shortens progressively (RR↓/SBP↓ sequences) are searched for. The changes in RR interval usually appear within one beat delay [156]. In [157], progressive SBP increases or decreases of at least 1 mmHg/beat and RR interval lengthenings or shortenings of at least 5 ms/beat were included. The BRS index is obtained as the slope of the regression line between the SBP and RR values within a sequence as described in Fig. 7.10. Furthermore, by averaging the slopes of several spontaneous sequences a more reliable value for BRS index is obtained [see Fig. 7.11 (a)]. These spontaneous sequences occur rather frequently (approximately 80 per

hour) [135] and, thus, fluctuations of BRS over time can as well be estimated with the sequence method.

However, all the progressive SBP sequences are not, even in healthy subjects, coupled with a progressive change in HR. The presence of such uncoupled SBP sequences might indicate that the baroreflex is not invariably effective. This aspect was considered in [157], where a new index, the *baroreflex effectiveness index* (BEI), was proposed. This index was defined as

$$\mathrm{BEI} = \frac{\text{number of RR/SBP sequences}}{\text{number of SBP sequences}} \tag{7.13}$$

where the number of RR/SBP sequences include both RR↑/SBP↑ and RR↓/SBP↓ sequences, where the RR interval sequence appeared with 0, 1, or 2 beat delay. The observed average BEI in healthy subjects during a 24 hour recording was 0.21. The lowness of the BEI was justified with other strong enough control mechanisms of HR (e.g. central neural influences and respiratory activity) that might partially mask the baroreflex influence of HR.

The sequence technique have been compared to the traditional intravenous drug injection methods in [137, 147] and a significant correlation between the two methods was found in both studies. There are, however, two methodological differences between the two methods that might explain the differences between the BRS estimates. First of all, the vasoactive drugs used in the traditional method can change the mechanical properties of the arterial wall where baroreceptors are located, which may result in a shifted reflex strength [147, 136]. Secondly, the drug injection method usually produces large BP changes, whereas spontaneous BP changes employed in the sequence technique are considerably smaller. Therefore, the sequence technique can only provide a portion of the stimulus-response curve (RR interval as a function of SBP), which in full-range is of sigmoidal shape [137].

7.7.2 Spectral methods

Alternatively, BRS can be assessed through spectral analysis. In spectral methods, SBP values are considered as system input and RR intervals as output and the BRS is obtained from the transfer function gain of the system [34, 161] or, more simply, by using the so-called *α-technique* [130]. In the α-technique, BRS index is estimated as the square root of ratio between RR and SBP powers within LF and HF bands, that is

$$\mathrm{BRS}_{\alpha,\mathrm{LF}} = \sqrt{P_{\mathrm{RR,LF}}/P_{\mathrm{SBP,LF}}} \tag{7.14}$$

$$\mathrm{BRS}_{\alpha,\mathrm{HF}} = \sqrt{P_{\mathrm{RR,HF}}/P_{\mathrm{SBP,HF}}} \tag{7.15}$$

where P_{RR} and P_{SBP} denote the RR interval and SBP powers within the specific frequency bands. The coupling between RR intervals and SBP within the HF band have been suggested to be of non-baroreflex origin [136] and, therefore, the LF band may be preferred for BRS evaluation.

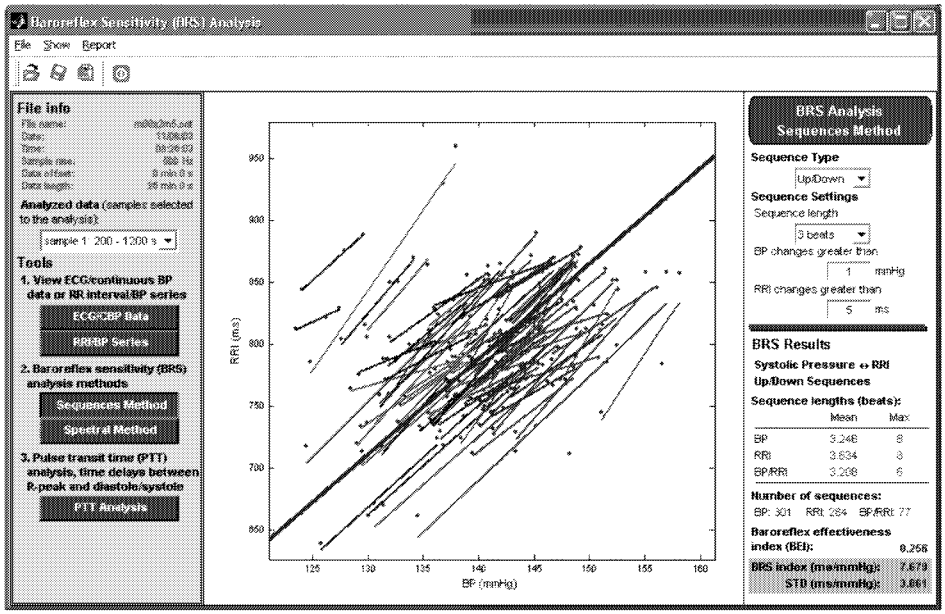

(a)

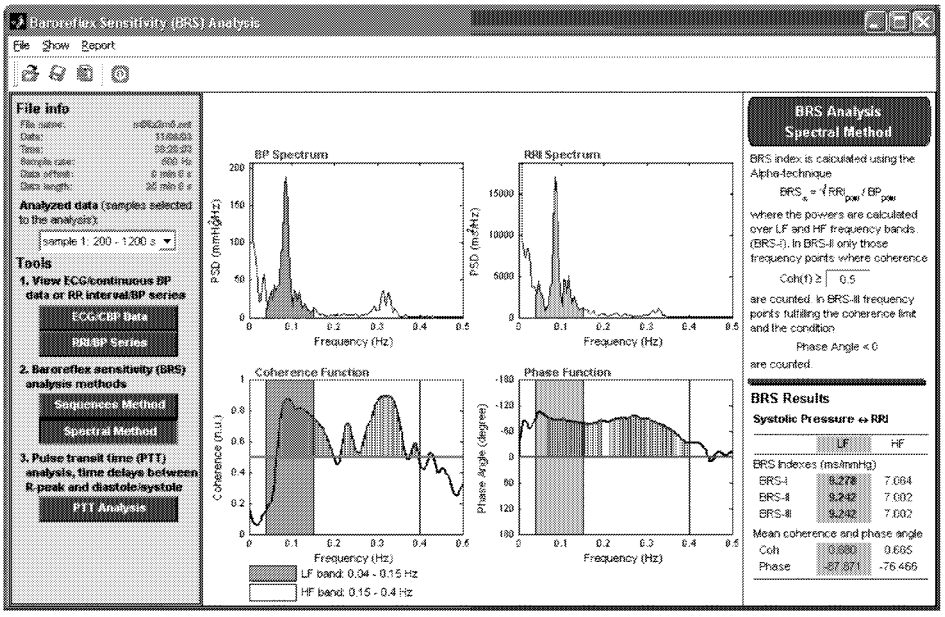

(b)

Figure 7.11: Estimation of the baroreflex sensitivity using (a) sequence technique and (b) frequency-domain α-technique. Snapshots of BRS analysis software, part of the Biosignal analysis software [1].

The transfer function gain is, however, meaningful only when the linear coupling of the input and output signals is strong enough. The linear coupling between two signals in frequency-domain can be expressed in terms of coherence function given in (3.58). Therefore, only those frequencies for which the coherence is sufficiently high (usually over 0.5) should be included in the BRS calculation [see Fig. 7.11 (b)]. The coherence is typically higher within the LF and HF bands and lowest in the frequencies below the LF band. Another factor describing the coupling of SBP and RR interval signals is the phase function given in (3.59). The phase is typically negative for most frequencies indicating that the SBP changes occur before the RR interval changes [34, 79]. Thus, one should also take the phase into account when calculating the BRS index.

The α-technique has been found to correlate with the results obtained from the traditional drug injection method [130, 147, 27]. The advantage of the sequence method compared to spectral methods is that it provides separate assessment of RR$\uparrow$/SBP$\uparrow$ and RR$\downarrow$/SBP$\downarrow$ sequences and, in addition, the effectiveness of baroreflex can be estimated as given by (7.13). In the spectral methods, on the other hand, BRS index is evaluated at specific frequencies and, thus, these methods enable the separate assessment of sympathetic and parasympathetic contributions of baroreflex HR modulation [136].

7.8 Discussion

The aim of this chapter was to give a short introduction to the analysis of cardiovascular signals. The origin and derivation of heart rate and blood pressure variability signals was given. One problematic feature of these signals that has to be considered prior to analysis is that they are non-equidistantly sampled. In this thesis, a cubic spline interpolation was used to overcome this problem. Prior to analysis, cardiovascular variability signals should also always be checked for artifacts. The most common artifact types of these signals were discussed in Section 7.4. The optimal case would be to include only artifact-free regions in the analysis. This is not, however, always possible in which case artifacts need to be corrected in some way before analysis.

Special attention was appointed to the slow trend components that are characteristic to cardiovascular signals. For removing such trend components an advanced detrending method was presented. The method is based on smoothness priors formulation and was originally presented in [176] with application to HRV analysis. The main advantage of the method, compared to methods presented in [149, 101], is its simplicity. The frequency response of the method is adjusted with a single parameter. This smoothing parameter κ should be selected in such a way that the spectral components of interest are not significantly affected by the detrending. Another advantage of the presented method is that the filtering effect is attenuated in the beginning and end of the data and thus the distortion of data end points is avoided.

The effect of detrending on time- and frequency-domain analysis of HRV was demonstrated in Section 7.6. In time-domain, most effect is focused on SDNN,

which describes the amount of overall variance of RR series. Instead only little effect is focused on RMSSD and pNN50 which both describe the differences in successive RR intervals. In frequency-domain, the low frequency trend components increase the power of VLF component. Particularly, it was pointed out that when relatively low order AR models are used in spectrum estimation the strong VLF component can distort other components, especially the LF component, of the spectrum. By using the detrending, on the other hand, the power of the VLF component is significantly reduced and the distortion of higher frequency components avoided.

The presented detrending method can be applied to, e.g., RSA quantification. The RSA component is separated from other frequency components of HRV by adjusting the smoothing parameter κ properly. For other purposes of HRV analysis one should make sure that the detrending does not lose any frequency components which carry useful information. Finally, it should be emphasized that the presented detrending method is not restricted to analysis of cardiovascular variability signals only, but can be applied as well to other biomedical signals, e.g., for detrending of EEG signals in quantitative EEG analysis.

In Section 7.7, two modern methods (sequence method and α-technique) for estimation of the baroreflex control of heart rate were described. Both methods evaluate the BRS index from spontaneous HR and BP fluctuations. Even though these methods are noninvasive and have been found to correlate with the traditional invasive methods, the general opinion is still that they should not be used in clinical practice as an alternative, but rather as complementary to the traditional methods.

Chapter VIII

Conclusions

In this thesis, three rather distinct novel methods for the analysis of biosignals were presented. The novelty within each proposed method lies in the application itself, not in the theoretical framework. The theories behind the proposed methods are well-known from before and they were presented in Chapters 2 4. The three novel applications were presented in Chapters 5 7.

The first proposed method, originally published in [174, 175], was a PCA based method for analyzing the patterning of successive GSR measurements. The theory of PCA is well-known and it was summarized in Section 2.4. PCA has a wide variety of applications in pattern recognition, but it has not been applied to GSRs before. A detailed description of the proposed method is given in Chapter 5. As a specific application the method was applied to GSRs measured from 20 healthy control subjects and 13 psychotic patients. The best obtained discrimination of the two subject groups, presented in Fig. 5.12, yielded the method a sensitivity of 100% and specificity of 70%. Furthermore, by using the binomial distribution it was argued that in 95% probability the sensitivity of the method is 75.3–100% and specificity 45.7–88.1%.

The observed high sensitivity of the method makes it a promising approach to be used as a screening test in clinical practice for specific risk-groups and prodromal patients in future. It should, however, be noted that the number of patients ($N = 13$) included in the study was rather small and, therefore, the method should be further validated with larger material before clinical use. One factor that was not extensively addressed here, but has an essential influence on the results of the method, is the applied classification technique. Here, an unsupervised classification method with a rather simple distance function was used, but also other approaches could be tested in future.

Furthermore, it should be noted that the proposed method is not restricted to GSR measurements, but can be applied to other kind of biosignals as well. For example, in [205], the method was applied for discriminating event-related brain potentials measured in different depths of sedation. With the method a significant discrimination of the awake, moderate sedation, and deep sedation states was obtained.

The second proposed method, originally published in [177, 172, 173], was a

Kalman smoother approach for the estimation of nonstationary EEG signals. The theory behind the Kalman smoother algorithm, presented in Sections 2.9 and 2.10, was proposed already in 1960ies [78, 153], but this is the first time it has been used for EEG signals. As a specific application the method was applied to estimation of event-related changes in occipital alpha rhythm synchronization. Using the Kalman smoother approach even the short-term changes such as the "squeak" effect of alpha rhythm could be observed even from single sample spectrum estimates. Using the traditional spectrum estimation methods such as the spectrogram the "squeak" effect could not be observed from single samples, but only by averaging several consecutive samples. The high time-frequency resolution of the Kalman smoother approach makes it a promising analysis method, e.g., for cognitive ERS/ERD experiments where the transition can not be assumed to recur alike from time to time.

There are two basic decisions in the Kalman smoother approach that have a decisive effect on the results, namely the model order and the adaptation coefficient (i.e. the state noise covariance). The model order selection can usually be based on the stationary case or on prevailing practice. The latter decision, on the other hand, leads to a trade-off between the time resolution and variance of the spectrum estimate. In the future studies, the statistics of the estimates could be further examined and rules for "optimal" adaptation coefficient selection would be desirable. Once the above decisions can be made, the Kalman smoother spectrum estimation method can basically be applied to any other biosignals as well. For example, in Fig. 7.8, it was applied to HRV time series measured during an orthostatic test.

The third proposed method, originally published in [176], was a smoothness priors based detrending method with application to HRV analysis. The theory of smoothness priors regularization was summarized in Section 2.5 and as a novel application it was used for detrending HRV time series in Chapter 7. The details of the proposed method were presented in Section 7.4 and the effect of the detrending on time- and frequency-domain analysis of HRV was considered in Section 7.6. Detrending removes the lowest frequencies from the HRV signal and, therefore, influences measures which are affected by long-term variability such as the SDNN. In addition, detrending was found essential when relatively low order AR models are used in spectrum estimation.

The issue of detrending is an important issue in biosignal analysis in general since the signal of interest is often desired to be stationary. That is, most of the ordinary analysis methods assume stationarity. The proposed detrending method is simple to use since the detrending level can be adjusted with a single parameter. In practice, one should always make sure that the detrending does not remove any useful information from the lower frequencies. That is, one should be aware of the lowest meaningful frequency within the signal and adjust the smoothing parameter accordingly. For example, when the RSA component of the HRV measurement is to be analyzed, the smoothing parameter can be set to remove the frequencies below 0.15 Hz.

In addition to the methodological applications, during the preparation of this

thesis, various analysis tools for the Biosignal analysis software [1] were developed. These include analysis tools for both event-related and spontaneous GSR measurements, quantitative and time-varying analysis tools for EEG measurements, and analysis tools for HRV and BPV measurements including BRS estimation tools (see Figs. 6.3, 7.6, and 7.11). In addition, the developed Biosignal analysis software include analysis tools, e.g., for event-related brain potentials and eye blinks. The whole software has been developed with Matlab® (Mathworks, Inc.). One noteworthy part of the software is the HRV analysis software, a limited version of which has also been compiled to a stand-alone Windows application [124], which has been distributed for free at request for clinicians and researchers worldwide.

REFERENCES

[1] Biosignal analysis software (http://it.uku.fi/biosignal/). Developed at the Department of Applied Physics, University of Kuopio.

[2] V.X. Afonso. ECG QRS detection. In W.J. Tompkins, editor, *Biomedical Digital Signal Processing*, chapter 12, pages 237–264. Prentice Hall, New Jersey, 1993.

[3] H. Akaike. Fitting autoregressive models for prediction. *Annals of the Institute of Statistics and Mathematics*, 21:243–247, 1969.

[4] H. Akaike. A new look at the statistical model identification. *IEEE Trans Automat Contr*, 19:716–723, 1974.

[5] M. Akay, editor. *Time Frequency and Wavelets in Biomedical Signal Processing*. IEEE Press, 1998.

[6] B.D.O. Anderson and J.B. Moore. *Optimal Filtering*. Prentice Hall, 1979.

[7] S. Aramaki, Y. Kira, and Y. Hirasawa. A study of the normal values and habituation phenomenon of sympathetic skin response. *Am J Phys Med Reh*, 76(1):2–7, January 1997.

[8] M. Arnold, H.R. Miltner, H. Witte, R. Bauer, and C. Braun. Adaptive AR modeling of nonstationary time series by means of Kalman filtering. *IEEE Trans Biomed Eng*, 45(5):553–562, May 1998.

[9] M. Baba, Y. Watahiki, M. Matsunaga, and K. Takebe. Sympathetic skin response in healthy man. *Electromyogr Clin Neurophysiol*, 28:277–283, 1988.

[10] J.S. Barlow. Methods of analysis of nonstationary EEGs, with emphasis on segmentation techniques: A comparative review. *Electroencephalogr Clin Neurophysiol*, 2(3):267–304, 1985.

[11] G. Baselli, S. Cerutti, S. Civardi, F. Lombardi, A. Malliani, M. Merri, M. Pagani, and G. Rizzo. Heart rate variability signal processing: a quantitative approach as an aid to diagnosis in cardiovascular pathologies. *Int J Bio-Med Comput*, 20:51–70, 1987.

[12] G.G. Berntson, J.T. Bigger Jr., D.L. Eckberg, P. Grossman, P.G. Kaufmann, M. Malik, H.N. Nagaraja, S.W. Porges, J.P. Saul, P.H. Stone, and M.W. Van Der Molen. Heart rate variability: Origins, methods, and interpretive caveats. *Psychophysiol*, 34:623–648, 1997.

[13] A.M. Bianchi, L. Mainardi, E. Petrucci, M.G. Signorini, M. Mainardi, and S. Cerutti. Time-variant power spectrum analysis for the detection of transient episodes in HRV signal. *IEEE Trans Biomed Eng*, 40(2):136–144, February 1993.

[14] A.M. Bianchi, L.T. Mainardi, C. Meloni, S. Chierchia, and S. Cerutti. Continuous

monitoring of the sympatho-vagal balance through spectral analysis. *IEEE Eng Med Biol Mag*, 16(5):64 73, September/October 1997.

[15] B. Boashash and M. Mesbah. A time-frequency approach for newborn seizure detection. *IEEE Eng Med Biol Mag*, 20(5):54 64, September/October 2001.

[16] J. Boberg. *Cluster Analysis, A Mathematical Approach with Applications to Protein Structures*. PhD thesis, University of Turku, Department of Computer Science, 1999.

[17] T. Bohlin. Analysis of EEG signals with changing spectra using a short-word Kalman estimator. *Math Biosci*, 35:221–259, 1977.

[18] H.-J. Braune and U. Geisenörfer. Measurement of heart rate variations: influencing factors, normal values and diagnostic impact on diabetic autonomic neuropathy. *Diabetes Res Clin Practice*, 29:179–187, 1995.

[19] M. Brennan, M. Palaniswami, and P. Kamen. Do existing measures of Poincaré plot geometry reflect nonlinear features of heart rate variability. *IEEE Trans Biomed Eng*, 48(11):1342–1347, November 2001.

[20] P. Cariga, M. Catley, C.J. Mathias, and P.H. Ellaway. Characteristics of habituation of the sympathetic skin response to repeated electrical stimuli in man. *Clin Neurophysiol*, 112:1875–1880, 2001.

[21] S. Carrasco, M.J. Caitán, R. González, and O. Yánez. Correlation among Poincaré plot indexes and time and frequency domain measures of heart rate variability. *J Med Eng Technol*, 25(6):240–248, November/December 2001.

[22] P. Celka, B. Boashash, and P. Colditz. Preprosessing and time-frequency analysis of newborn EEG seizures. *IEEE Eng Med Biol Mag*, 20(5):30–39, September/October 2001.

[23] J. Chen, W.R. Stewart, and R.W. McCallum. Spectral analysis of episodic rhythmic variations in the cutaneous electrogastrogram. *IEEE Trans Biomed Eng*, 40(2):128–135, February 1993.

[24] B. Choi. *ARMA Model Identification*. Springer-Verlag, 1992.

[25] B. C. Cohen and A. Sances Jr. Stationarity of the human electroencephalogram. *Med Biol Eng Comput*, 15:513–518, 1977.

[26] L. Cohen. Time-frequency distributions - a review. *Proc IEEE*, 77(7):941 981, July 1989.

[27] R. Colombo, G. Mazzuero, G. Spinatonda, P. Lanfranchi, P. Giannuzzi, P. Ponikowski, A.J.S. Coats, and G. Minuco. Comparison between spectral analysis and the phenylephrine method for the assessment of baroreflex sensitivity in chronic heart failure. *Clin Sci*, 97:503–513, 1999.

[28] H.D. Critchley, R. Elliott, C.J. Mathias, and R.J. Dolan. Neural activity relating to generation and representation of galvanic skin conductance responses: a functional magnetic resonance imaging study. *J Neurosci*, 20(8):3033–3040, April 2000.

[29] I. Daskalov and I. Christov. Improvement of resolution in measurement of electrocardiogram RR intervals by interpolation. *Med Eng Phys*, 19(4):375–379, June 1997.

[30] M.E. Dawson, A.M. Schell, and D.L. Filion. The electrodermal system. In J.T. Cacioppo, L.G. Tassinary, and G.G. Berntson, editors, *Handbook of Psychophysiology*, chapter 8, pages 200–223. Cambridge University Press, 2000.

[31] J.F.G. de Freitas, M. Niranjan, and A.H. Gee. Hierarchical Bayesian-Kalman models for regularisation and ARD in sequential learning. Technical report, Department of Engineering, Cambridge University, 1998.

[32] R.W. DeBoer, J.M. Karemaker, and J. Strackee. Comparing spectra of a series of

point events particularly for heart rate variability data. *IEEE Trans Biomed Eng*, 31(4):384–387, April 1984.

[33] R.W. DeBoer, J.M. Karemaker, and J. Strackee. Spectrum of a series of point events, generated by the integral pulse frequency modulation model. *Med Biol Eng Comput*, 23:138–142, March 1985.

[34] R.W. DeBoer, J.M. Karemaker, and J. Strackee. Hemodynamic fluctuations and baroreflex sensitivity in humans: a beat-to-beat model. *Am J Physiol*, 253:680–689, 1987.

[35] T. Deltombe, P. Hanson, J. Jamart, and M. Clérin. The influence of skin temperature on latency and amplitude of the sympathetic skin response in normal subjects. *Muscle & Nerve*, 21:34–39, January 1998.

[36] V.E. Drory and A.D. Korczyn. Sympathetic skin response: age effect. *Neurology*, 43:1818–1820, September 1993.

[37] M. Ducher, C. Cerutti, M.P. Gustin, and C.Z. Paultre. Statistical relationships between systolic blood pressure and heart rate and their functional significance in conscious rats. *Med Biol Eng Comput*, 32:649–655, November 1994.

[38] J. Durbin and S.J. Koopman. *Time Series Analysis by State Space Methods*. Oxford University Press Inc., 2001.

[39] P.J. Durka, D. Ircha, C. Neuper, and G. Pfurtscheller. Time-frequency microstructure of event-related EEG desynchronization and synchronization. *Med Biol Eng Comput*, 39(3):315–321, May 2001.

[40] B. Elie and P. Guiheneuc. Sympathetic skin response: normal results in different experimental conditions. *Electroencephalogr Clin Neurophysiol*, 76:258–267, 1990.

[41] G. Florian and G. Pfurtscheller. Dynamic spectral analysis of event-related EEG data. *Electroencephalogr Clin Neurophysiol*, pages 393–396, 1995.

[42] D.C. Fowles, M.J. Christie, R. Edelberg, W.W. Grings, D.T. Lykken, and P.H. Venables. Publication recommendations for electrodermal measurements. *Psychophysiol*, 18(3):232–239, May 1981.

[43] D.C. Fraser and J.E. Potter. The optimum linear smoother as a combination of two optimum linear filters. *IEEE Trans Automat Contr*, 14:387–390, 1969.

[44] G.M. Friesen, T.C. Jannett, M.A. Jadallah, S.L. Yates, S.R. Quint, and H.T. Nagle. A comparison of the noise sensitivity of nine QRS detection algorithms. *IEEE Trans Biomed Eng*, 37(1):85–98, January 1990.

[45] Y. Fusheng, H. Bo, and T. Qingyu. Approximate entropy and its application in biosignal analysis. In M. Akay, editor, *Nonlinear Biomedical Signal Processing: Dynamic Analysis and Modeling*, volume II, chapter 3, pages 72–91. IEEE Press, New York, 2001.

[46] M.A. García-González and R. Pallás-Areny. A novel robust index to assess beat-to-beat variability in heart rate time-series analysis. *IEEE Trans Biomed Eng*, 48(6):617–621, June 2001.

[47] I. Gath, C. Feuerstein, D.T. Pham, and G. Rondouin. On the tracking of rapid dynamic changes in seizure EEG. *IEEE Trans Biomed Eng*, 39:952–958, 1992.

[48] A. B. Geva and H. Pratt. Unsupervised clustering of evoked potentials by waveform. *Med Biol Eng Comput*, 32:543–550, September 1994.

[49] J. Ginter Jr, K.J. Blinowska, M. Kamiński, and P.J. Durka. Phase and amplitude analysis in time-frequency space—application to voluntary finger movement. *J Neurosci Meth*, 110:113–124, 2001.

[50] S. Goto, M. Nakamura, and K. Uosaki. On-line spectral estimation of nonstationary time series based on AR model parameter estimation and order selection with

a forgetting factor. *IEEE Trans Signal Processing*, 43(6):1519 1522, June 1995.

[51] B. Graimann, J.E. Huggins, S.P. Levine, and G. Pfurtscheller. Visualization of significant ERD/ERS patters in multichannel EEG and ECoG data. *Clin Neurophysiol*, 113:43 47, 2002.

[52] P. Grossman. Breathing rhythms of the heart in a world of no steady state: a comment on Weber, Molenaar, and van der Molen. *Psychophysiol*, 29(1):66–72, January 1992.

[53] F. Gustafsson and H. Hjalmarsson. Twenty-one ML estimators for model selection. *Automatica*, 31:1377–1392, 1995.

[54] J.A. Gutrecht. Sympathetic skin response. *J Clin Neurophysiol*, 11(5):519 524, 1994.

[55] S. Guzzetti, M.G. Signorini, C. Cogliati, S. Mezzetti, A. Porta, S. Cerutti, and A. Malliani. Non-linear dynamics and chaotic indices in heart rate variability of normal subjects and heart-transplanted patients. *Cardiovascular Research*, 31:441 446, 1996.

[56] P.S. Hamilton and W.J. Tompkins. Quantitative investigation of QRS detection rules using the MIT/BIH arrhythmia database. *IEEE Trans Biomed Eng*, 33(12):1157–1165, December 1986.

[57] P.C. Hansen. *Regularization Tools: A Matlab Package for Analysis and Solution of Discrete Ill-Posed Problems*. UNI-C, Technical University of Denmark, 1992.

[58] R. Hari and R. Salmelin. Human cortical oscillations: a neuromagnetic view through the skull. *Trends Neurosci*, 20(1):44 49, 1997.

[59] M. Haseyama and H. Kitajima. An ARMA order selection method with fuzzy reasoning. *Signal Processing*, 81:1331–1335, 2001.

[60] S. Haykin. *Adaptive Filter Theory*. Prentice Hall, 2 edition, 1991.

[61] B. Henry, N. Lovell, and F. Camacho. Nonlinear dynamics time series analysis. In M. Akay, editor, *Nonlinear Biomedical Signal Processing: Dynamic Analysis and Modeling*, volume II, chapter 1, pages 1 39. IEEE Press, New York, 2001.

[62] J.K. Hiltunen. Estimation of the dynamics of event-related desynchronization. Phil. Lic. thesis, University of Kuopio, Department of Applied Physics, August 1999.

[63] F. Hlawatsch and G.F. Boudreaux-Bartels. Linear and quadratic time-frequency signal representations. *IEEE Signal Processing Mag*, pages 21–67, April 1992.

[64] H. Hotelling. Analysis of a complex of statistical variables into principal components. *J Educ Psych*, 24:498–520, 1933.

[65] H.V. Huikuri, T.H. Mäkikallio, P. Raatikainen, J. Perkiömäki, A. Castellanos, and R.J. Myerburg. Prediction of sudden cardiac death: appraisal of the studies and methods assessing the risk of sudden arrhythmic death. *Circulation*, 108(1):110–115, July 2003.

[66] A. Isaksson and A. Wennberg. An EEG simulator - a means of objective clinical interpretation of EEG. *Electroencephalogr Clin Neurophysiol*, 39:313–320, 1975.

[67] A. Isaksson and A. Wennberg. Spectral properties of nonstationary EEG signals, evaluated by means of Kalman filtering: Application examples from a vigilance test. In P. Kellaway and I. Petersen, editors, *Quantitative Analytic Studies in Epilepsy*, pages 389–402. Raven Press, 1976.

[68] A. Isaksson, A. Wennberg, and L.H. Zetterberg. Computer analysis of EEG signals with parametric models. *Proc IEEE*, 69:451–461, 1981.

[69] B. Jansen. Quantitative analysis of electroencephalograms: Is there chaos in the future? *Int J Bio-Med Comput*, 27:95 123, 1991.

[70] A.H. Jazwinski. Adaptive filtering. *Automatica*, 5:475–485, July 1969.

[71] E.R. John, D.S. Ruchkin, and J. Villegas. Experimental background: signal analysis and behavioral correlates of evoked potential configurations in cats. *Ann N Y Acad Sci*, 112:362–420, 1964.

[72] S.J. Johnsen and N Andersen. On power estimation in maximum entropy spectral analysis. *Geophysics*, 43:681–690, June 1978.

[73] I.T. Jolliffe. *Principal Component Analysis*. Springer-Verlag, 1986.

[74] S. Kadambe, R. Murray, and G.F. Boudreaux-Bartels. Wavelet transform-based QRS complex detector. *IEEE Trans Biomed Eng*, 46(7):838–848, July 1999.

[75] J.P. Kaipio. *Simulation and Estimation of Nonstationary EEG*. PhD thesis, University of Kuopio, 1996. Available: http://venda.uku.fi/research/IP/.

[76] J.P. Kaipio and P.A. Karjalainen. Simulation of nonstationary EEG. *Biol Cybern*, 76:349–356, 1997.

[77] J. Kalcher and G. Pfurtscheller. Discrimination between phase-locked and non-phase-locked event-related EEG activity. *Electroencephalogr Clin Neurophysiol*, 94:381–384, 1995.

[78] R.E. Kalman. A new approach to linear filtering and prediction problems. *Trans ASME J Basic Eng*, 82:35–45, 1960.

[79] J.M. Karemaker. Analysis of blood pressure and heart rate variability: theoretical considerations and clinical applicability. In P.A. Low, editor, *Clinical Autonomic Disorders*, pages 315–328. Mayo Foundation, Rochester, 1993.

[80] K. Karhunen. Zur spektraltheorie stochastischer prozesse. *Ann Acad Sci Fennicae*, 34, 1946.

[81] P.A. Karjalainen. Estimation theoretical background of root tracking algorithms with application to EEG. Phil. Lic. thesis, University of Kuopio, Department of Applied Physics, 1996. Available: http://it.uku.fi/biosignal.

[82] P.A. Karjalainen. *Regularization and Bayesian Methods for Evoked Potential Estimation*. PhD thesis, University of Kuopio, Department of Applied Phsics, 1997. Available: http://it.uku.fi/biosignal.

[83] N. Kawabata. A nonstationary analysis of the electroencephalogram. *IEEE Trans Biomed Eng*, 20:444–452, 1973.

[84] S.M. Kay. *Modern Spectral Estimation: Theory and Applications*. Prentice-Hall, 1988.

[85] L. Keselbrener and S. Akselrod. Artefacts in standard and time-dependent spectral analysis of arterial blood pressure signals obtained by Finapres: importance and correction. *Clin Auton Res*, 5(5):295–301, October 1995.

[86] L. Keselbrener and S. Akselrod. Selective discrete Fourier transform algorithm for time-frequency analysis: method and application on simulated and cardiovascular signals. *IEEE Trans Biomed Eng*, 43(8):789–802, August 1996.

[87] S.Y. Kim and D.E. Euler. Baroreflex sensitivity assessed by complex demodulation of cardiovascular variability. *Hypertension*, 29(5):1119–1125, May 1997.

[88] G. Kitagawa and W. Gersch. *Smoothness Priors Analysis of Time Series*. Springer-Verlag, 1996.

[89] G.H. Klem, H.O. Lüders, H.H. Jasper, and C. Elger. The ten-twenty electrode system of the international federation. In G. Deuschl and A. Eisen, editors, *Recommendations for the Practice of Clinical Neurophysiology: Guidelines of the International Federation of Clinical Neurophysiology*, pages 3–6. Elsevier, 1999.

[90] W. Klimesch. EEG alpha and theta oscillations reflect cognitive and memory performance: a review and analysis. *Brain Research Reviews*, 29:169–195, 1999.

[91] W. Knezevic and S. Bajada. Peripheral autonomic surface potential: a quantitative technique for recording sympathetic skin conduction in man. *J Neur Sci*, 67:239 251, 1985.

[92] I. Korhonen. *Methods for the Analysis of Short-Term Variability of Heart Rate and Blood Pressure in Frequency Domain.* PhD thesis, Technical Research Center of Finland, VTT, 1997.

[93] I. Korhonen, L. Mainardi, G. Baselli, A. Bianchi, P. Loula, and G. Carrault. Linear multivariate models for physiological signal analysis: applications. *Comput Meth Programs Biomed*, 51:121–130, 1996.

[94] I. Korhonen, L. Mainardi, P. Loula, G. Carrault, G. Baselli, and A. Bianchi. Linear multivariate models for physiological signal analysis: theory. *Comput Meth Programs Biomed*, 51:85–94, 1996.

[95] C.L. Lawson and R.J. Hanson. *Solving Least Squares Problems.* SIAM, 1995.

[96] D.M. Levy, G. Reid, D.A. Rowley, and R.R. Abraham. Quantitative measurements of sympathetic skin response in diabetes: relation to sudomotor and neurological function. *J Neurol Neurosurg Psychiatr*, 55:902 908, 1992.

[97] R. Liguori, V. Donadio, E. Foschini, V. Di Stasi, G. Plazzi, E. Lugaresi, and P. Montagna. Sleep stage-related changes in sympathetic sudomotor and vasomotor skin responses in man. *Clin Neurophysiol*, 111:434 439, 2000.

[98] C.L. Lim, C. Rennie, R.J. Barry, H. Bahramali, I. Lazarro, B. Manor, and E. Gordon. Decomposing skin conductance into tonic and phasic components. *Int J Psychophysiol*, 25:97 109, 1997.

[99] N. Lippman, K.M. Stein, and B.B. Lerman. Nonlinear predictive interpolation: a new method for the correction of ectopic beats for heart rate variability analysis. *J Electrocardiol*, 26:S14 S19, 1993.

[100] N. Lippman, K.M. Stein, and B.B. Lerman. Comparison of methods for removal of ectopy in measurement of heart rate variability. *Am J Physiol*, 267(1):H411–H418, July 1994.

[101] D.A. Litvack, T.F. Oberlander, L.H. Carney, and J.P. Saul. Time and frequency domain methods for heart rate variability analysis: a methodological comparison. *Psychophysiol*, 32:492 504, 1995.

[102] L. Ljung and S. Gunnarsson. Adaptation and tracking in system identification – a survey. *Automatica*, 26:7–21, 1990.

[103] M. Loéve. Fonctions alćatoires du second ordre. In P. Lévy, editor, *Processus Stochastiques et Mouvement Brownien*, page 299. Gauthier - Villars, Paris, 1948.

[104] F. Lombardi, T.H. Mäkikallio, R.J. Myerburg, and H. Huikuri. Sudden cardiac death: role of heart rate variability to identify patients at risk. *Cardiovasc Res*, 50:210–217, 2001.

[105] L.T. Mainardi, A.M. Bianchi, G. Baselli, and S. Cerutti. Pole-tracking algorithms for the extraction of time-variant heart rate variability spectral parameters. *IEEE Trans Biomed Eng*, 42(3):250–259, March 1995.

[106] S. Makeig, M. Westerfield, T.P. Jung, S. Enghoff, J. Townsend, E. Courchesne, and T.J. Sejnowski. Dynamic brain sources of visual evoked responses. *Science*, 295:690–694, January 2000.

[107] A. Malliani, M. Pagani, F. Lombardi, and S. Cerutti. Cardiovascular neural regulation explored in the frequency domain. *Circulation*, 84(2):482 492, August 1991.

[108] J. Malmivuo and R. Plonsey. *Bioelectromagnetism: Principles and Applications of Bioelectric and Biomagnetic Fields.* Oxford University Press (Web Edition), 1995.

[109] O.M. Markand. Alpha rhythms. *J Clin Neurophysiol*, 7:163 189, 1990.

[110] S.L. Marple. *Digital Spectral Analysis with Applications.* Prentice-Hall, 1987.

[111] J. Mateo and P. Laguna. Improved heart rate variability signal analysis from the beat occurrence times according to the IPFM model. *IEEE Trans Biomed Eng*, 47(8):985–996, August 2000.

[112] J. Mateo and P. Laguna. Analysis of heart rate variability in the presence of ectopic beats using the heart timing signal. *IEEE Trans Biomed Eng*, 50(3):334–343, March 2003.

[113] J.L. Melsa and D.L. Cohn. *Decision and Estimation Theory.* McGraw-Hill, 1978.

[114] M. Merri, D.C. Farden, J.G. Mottley, and E.L. Titlebaum. Sampling frequency of the electrocardiogram for spectral analysis of the heart rate variability. *IEEE Trans Biomed Eng*, 37(1):99–106, January 1990.

[115] I.P. Mitov. A method for assessment and processing of biomedical signals containing trend and periodic components. *Med Eng Phys*, 20(9):660–668, November-December 1998.

[116] J. Möcks. The influence of latency jitter in principal component analysis of event-related potentials. *Psychophysiol*, 23:480–484, 1986.

[117] N.H. Morgan and A.S. Gevins. Wigner distributions of human event-related brain potentials. *IEEE Trans Biomed Eng*, 33(1):66–70, January 1986.

[118] R.E. Mortensen. *Random Signals and Systems.* Wiley, 1987.

[119] L.J.M. Mulder. *Assessment of Cardiovascular Reactivity by Means of Spectral Analysis.* PhD thesis, University of Groningen, 1988.

[120] J. Muthuswamy and N.V. Thakor. Spectral analysis methods for neurological signals. *J Neurosci Meth*, 83:1–14, 1998.

[121] M.R. Neuman. Biopotential electrodes. In J.G. Webster, editor, *Medical Instrumentation: Application and Design*, chapter 5, pages 227–287. Wiley, 1995.

[122] E. Niedermeyer. Alpha rhythms as physiological and abnormal phenomena. *Int J Psychophysiol*, 26:31–49, 1997.

[123] E. Niedermeyer and F.L. da Silva, editors. *Electroencephalography: Basic Principles, Clinical Applications, and Related Fields.* Williams & Wilkins, Baltimore, 4th edition, 1999.

[124] J-P. Niskanen, M.P. Tarvainen, P.O. Ranta-aho, and P.A. Karjalainen. Software for advanced HRV analysis. *Comput Meth Programs Biomed*, In Press.

[125] P. Novak and V. Novak. Time/frequency mapping of heart rate, blood pressure and respiratory signals. *Med Biol Eng Comput*, 31:103–110, March 1993.

[126] M.R. Nuwer. Quantitative EEG: I. techniques and problems of frequency analysis and topographic mapping. *J Clin Neurophysiol*, 5(1):1–43, 1988.

[127] M.R. Nuwer. Quantitative EEG: II. frequency analysis and topographic mapping in clinical settings. *J Clin Neurophysiol*, 5(1):45–85, 1988.

[128] E. Oja. *Subspace Methods in Pattern Recognition.* Wiley, 1983.

[129] M. Pagani. Heart rate variability and autonomic diabetic neuropathy. *Diabetes Nutrition & Metabolism*, 13(6):341–346, 2000.

[130] M. Pagani, V. Somers, R. Furlan, S. Dell'Orto, J. Conway, G. Baselli, S. Cerutti, P. Sleight, and A. Malliani. Changes in autonomic regulation induced by physical training in mild hypertension. *Hypertension*, 12(6):600–610, 1988.

[131] O. Pahlm and L. Sörnmo. Software QRS detection in ambulatory monitoring – a review. *Med Biol Eng Comput*, 22:289–297, July 1984.

[132] J. Pan and W.J. Tompkins. A real-time QRS detection algorithm. *IEEE Trans Biomed Eng*, 32(3):230–236, March 1985.

[133] A. Papoulis. *Probability, Random Variables, and Stochastic Processes.* McGraw-

Hill, 1984.

[134] A. Papoulis. *Signal Analysis*. McGraw-Hill, 1984.

[135] G. Parati, M. Di Rienzo, G. Bertinieri, G. Pomidossi, R. Casadei, A. Groppelli, A. Pedotti, A. Zanchetti, and G. Mancia. Evaluation of the baroreceptor-heart rate reflex by a 24-hour intra-arterial blood pressure monitoring in humans. *Hypertension*, 12(2):214–222, 1988.

[136] G. Parati, M. Di Rienzo, and G. Mancia. How to measure baroreflex sensitivity: from the cardiovascular laboratory to daily life. *J Hypertension*, 18(1):7 19, 2000.

[137] J. Parlow, J.-P. Viale, G. Annat, R. Hughson, and L. Quintin. Spontaneous cardiac baroreflex in humans - comparison with drug-induced responses. *Hypertension*, 25(5):1058 1068, May 1995.

[138] K. Pearson. On lines and planes of closest fit to systems of points in space. *Phil Mag*, 2(6):559 572, 1901.

[139] J. Peñáz. *Patentova Listina, CISLO 133 205*. 1969.

[140] J. Peñáz. Photoelectric measurement of blood pressure, volume and flow in the finger. In *Digest 10th Int Conf Med Biol Eng*, page 104, Dresden, 1973.

[141] C.-K. Peng, S. Havlin, H.E. Stanley, and A.L. Goldberger. Quantification of scaling exponents and crossover phenomena in nonstationary heartbeat time series. *Chaos*, 5:82 87, 1995.

[142] T. Penzel, J.W. Kantelhardt, L. Grote, J.-H. Peter, and A. Bunde. Comparison of detrended fluctuation analysis and spectral analysis for heart rate variability in sleep and sleep apnea. *IEEE Trans Biomed Eng*, 50(10):1143 1151, October 2003.

[143] G. Pfurtscheller. Event–related synchronization (ERS): an electrophysiological correlate of cortical areas at rest. *Electroencephalogr Clin Neurophysiol*, 83:62–69, 1992.

[144] G. Pfurtscheller and F.H. Lopes da Silva. Event-related EEG/MEG synchronization and desynchronization: basic principles. *Clin Neurophysiol*, 110:1842–1857, 1999.

[145] G. Pfurtscheller, C. Neuper, and W. Mohl. Event-related desynchronization (ERD) during visual processing. *Int J Psychophysiol*, 16:147–153, 1994.

[146] G.D. Pinna, R. Maestri, A. Di Cesare, R. Colombo, and G. Minuco. The accuracy of power-spectrum analysis of heart-rate variability from annotated RR lists generated by Holter systems. *Physiol Meas*, 15:163–179, 1994.

[147] M.V. Pitzalis, F. Mastropasqua, A. Passantino, F. Massari, L. Ligurgo, C. Forleo, C. Balducci, F. Lombardi, and P. Rizzon. Comparison between noninvasive indices of baroreceptor sensitivity and the phenylephrine method in post-myocardial infarction patients. *Circulation*, 97(14):1362 1367, April 1998.

[148] R.T. Pivik, R.J. Broughton, R. Coppola, R.J. Davidson, N. Fox, and M.R. Nuwer. Guidelines for the recording and quantitative analysis of electroencephalographic activity in research contexts. *Psychophysiol*, 30:547 558, 1993.

[149] S.W. Porges and R.E. Bohrer. The analysis of periodic processes in psychophysiological research. In J.T. Cacioppo and L.G. Tassinary, editors, *Principles of Psychophysiology: Physical Social and Inferential Elements*, pages 708 753. Cambridge University Press, 1990.

[150] A. Porta, G. Baselli, O. Rimoldi, A. Malliani, and M. Pagani. Assessing baroreflex gain from spontaneous variability in conscious dogs: role of causality and respiration. *Am J Physiol*, 279(5):H2558–H2567, November 2000.

[151] M.B. Priestley. *Spectral Analysis and Time Series*. Academic Press, 1981.

[152] R.K.A. Radhakrishna, D.N. Kutt, and V.K. Yeragani. Nonlinear measures of heart

rate time series: influence of posture and controlled breathing. *Auton Neurosci-Basic Clin*, 83:148–158, 2000.

[153] H.E. Rauch, F. Tung, and C.T. Striebel. Maximum likelihood estimates of linear dynamic systems. *AIAA Journal*, 3:1445–1450, 1965.

[154] J.A. Richman and J.R. Moorman. Physiological time-series analysis using approximate entropy and sample entropy. *Am J Physiol*, 278:H2039–H2049, 2000.

[155] M. Di Rienzo, G. Bertinieri, G. Mancia, and A. Pedotti. A new method for evaluating the baroreflex role by a joint pattern analysis of pulse interval and systolic blood pressure series. *Med Biol Eng Comput*, 23(suppl. I):313–314, 1985.

[156] M. Di Rienzo, P. Castiglioni, G. Mancia, A. Pedotti, and G. Parati. Advancements in estimating baroreflex function. *IEEE Eng Med Biol Mag*, 20(2):25–32, March/April 2001.

[157] M. Di Rienzo, G. Parati, P. Castiglioni R. Tordi, , G. Mancia, and A. Pedotti. Baroreflex effectiveness index: an additional measure of baroreflex control of heart rate in daily life. *Am J Physiol*, 280:R744–R751, 2001.

[158] O. Rioul and P. Flandrin. Time-scale energy distributions: a general class extending wavelet transforms. *IEEE Trans Signal Processing*, 40(7):1746–1757, July 1992.

[159] O. Rioul and M. Vetterli. Wavelets and signal processing. *IEEE Signal Processing Mag*, pages 14–38, October 1991.

[160] J. Rissanen. A universal prior for the integers and estimation by minimum description length. *Ann Statist*, 11:417–431, 1983.

[161] H.W.J. Robbe, L.J.M. Mulder, H. Rüddel, W.A. Langewitz, J.B.P. Veldman, and G. Mulder. Assessment of baroreceptor reflex sensitivity by means of spectral analysis. *Hypertension*, 10(5):538–543, November 1987.

[162] O. Rompelman. Rhythms and analysis techniques. In J. Strackee and N. Westerhof, editors, *The Physics of Heart and Circulation*, pages 101–120. Institute of Physics Publishing, Bristol, 1993.

[163] W.T. Roth, K.H. Dorato, and B.S. Kopell. Intensity and task effects on evoked physiological responses to noise bursts. *Psychophysiol*, 21(4):466–481, July 1984.

[164] A. Van Rotterdam. Limitation and difficulties in signal processing by means of the principal-components analysis. *IEEE Trans Biomed Eng*, 17:268–269, 1970.

[165] D. Samson-Dollfus, G. Delapierre, C. Do Marcoline, and C. Blondeau. Normal and pathological changes in alpha rhythms. *Int J Psychophysiol*, 26:395–409, 1997.

[166] S.J. Schiff, J.G. Milton, J. Heller, and S.L. Weinstein. Wavelet transforms and surrogate data for electroencephalographic spike and seizure localization. *Opt Eng*, 33(7):2162–2169, 1994.

[167] A. Schlögl. *The Electroencephalogram and the Adaptive Autoregressive Model: Theory and Applications*. PhD thesis, Technischen Universität Graz, 2000.

[168] B.T. Shahani, J.J. Halperin, P. Boulu, and J.Y. Cohen. Sympathetic skin response—a method of assessing unmyelinated axon dysfunction in peripheral neuropathies. *J Neurol Neurosurg Psychiatr*, 47:536–542, 1984.

[169] H.W. Sorenson. *Parameter Estimation: Principles and Problems*. Marcel Dekker, 1980.

[170] H.W. Sorenson, editor. *Kalman Filtering: Theory and Applications*. IEEE Press, 1985.

[171] P. Strobach. *Linear Prediction Theory*. Springer-Verlag, 1990.

[172] M.P. Tarvainen, J.K. Hiltunen, P.O. Ranta-aho, and P.A. Karjalainen. Tracking of nonstationary EEG with Kalman smoother approach: an application to event-

related synchronization of alpha waves. In *Proceedings of 24th Annual Conference of IEEE/EMBS*, Houston, Texas, Oct. 23-26 2002.

[173] M.P. Tarvainen, J.K. Hiltunen, P.O. Ranta-aho, and P.A. Karjalainen. Estimation of nonstationary EEG with Kalman smoother approach: an application to event-related synchronization (ERS). *IEEE Trans Biomed Eng*, 51(3):516 524, March 2004.

[174] M.P. Tarvainen, P.A. Karjalainen, A.S. Koistinen, and M. Valkonen-Korhonen. Principal component analysis of galvanic skin responses. In *Proceedings of 22nd Annual Conference of IEEE/EMBS*, Chicago, July 2000.

[175] M.P. Tarvainen, A.S. Koistinen, M. Valkonen-Korhonen, J. Partanen, and P.A. Karjalainen. Analysis of galvanic skin responses with principal components and clustering techniques. *IEEE Trans Biomed Eng*, 48(10):1071–1079, October 2001.

[176] M.P. Tarvainen, P.O. Ranta-aho, and P.A. Karjalainen. An advanced detrending method with application to HRV analysis. *IEEE Trans Biomed Eng*, 49(2):172 175, February 2001.

[177] M.P. Tarvainen, P.O. Ranta-aho, and P.A. Karjalainen. Tracking of nonstationary EEG with Kalman smoother approach. In *Proceedings of 23rd Annual Conference of IEEE/EMBS*, Istanbul, Turkey, Oct. 25-28 2001.

[178] Task force of the European society of cardiology and the North American society of pacing and electrophysiology. Heart rate variability – standards of measurement, physiological interpretation, and clinical use. *Circulation*, 93(5):1043–1065, March 1996.

[179] N.V. Thakor, X.R. Guo, Y.C. Sun, and D.F. Hanley. Multiresolution wavelet analysis of evoked potentials. *IEEE Trans Biomed Eng*, 40(11):1085–1094, 1993.

[180] N.V. Thakor, J.G. Webster, and W.J. Tompkins. Optimal QRS detector. *Med Biol Eng Comput*, 21:343–350, May 1983.

[181] A.N. Tikhonov. Solution of incorrectly formulated problems and the regularization method. *Soviet. Math. Dokl.*, 4:1035 1038, 1963.

[182] P. Tikkanen. *Characterization and Application of Analysis Methods for ECG and Time Interval Variability Data.* PhD thesis, University of Oulu, Department of Physical Sciences, Division of Biophysics, 1999.

[183] M. Toyokura. Waveform and habituation of sympathetic skin response. *Electroencephalogr Clin Neurophysiol*, 109:178–183, 1998.

[184] M. Toyokura. Waveform variation and size of sympathetic skin response: regional difference between the sole and palm recordings. *Clin Neurophysiol*, 110:765–771, 1999.

[185] M. Toyokura. Influence of stimulus intensity on waveform of sympathetic skin response evoked by magnetic stimulation. *Clin Neurophysiol*, 114:1423–1430, 2003.

[186] L.L. Trulla, A. Giuliani, J.P. Zbilut, and C.L. Webber Jr. Recurrence quantification analysis of the logistic equation with transients. *Phys Lett A*, 223(4):255 260, 1996.

[187] A. Uncini, S.L. Pullman, R.E. Lovelace, and D. Gambi. The sympathetic skin response: normal values, elucidation of afferent components, and application limits. *J Neur Sci*, 87:299 306, 1988.

[188] M. Unser and A. Aldroubi. A review of wavelets in biomedical applications. *Proc IEEE*, 84(4):626–638, April 1996.

[189] M. Valkonen-Korhonen, A. Koistinen, P. Karjalainen, J. Lehtonen, and J. Karhu. Loss of time-organized sympathetic skin responses in acute psychosis. *J Nerv Ment Disease*, 198(8):552–556, 2001.

[190] R. Vertugno, R. Liguori, P. Cortelli, and P. Montagna. Sympathetic skin response:

basic mechanisms and clinical applications. *Clin Auton Res*, 13:256–270, 2003.

[191] M. Vetterli and C. Herley. Wavelets and filter banks: theory and design. *IEEE Trans Signal Processing*, 40(9):2207–2232, September 1992.

[192] J. Vila, F. Palacios, J. Presedo, M. Fernández-Delgado, P. Felix, and S. Barro. Time-frequency analysis of heart-rate variability. *IEEE Eng Med Biol Mag*, 16(5):119–126, September/October 1997.

[193] S.R. Vrana. Emotional modulation of the skin conductance and eyeblink responses to a startle probe. *Psychophysiol*, 32:351–357, 1995.

[194] C.L. Webber Jr. and J.P. Zbilut. Dynamical assessment of physiological systems and states using recurrence plot strategies. *J Appl Physiol*, 76:965–973, 1994.

[195] E.J.M. Weber, C.M. Molenaar, and M.W. van der Molen. A nonstationarity test for the spectral analysis of physiological time series with an application to respiratory sinus arrhythmia. *Psychophysiol*, 29(1):55–65, January 1992.

[196] A. Wennberg and A. Isaksson. Simulation of nonstationary EEG signals as a means of objective clinical interpretation of EEG. In *Quantitative Analytical Studies in Epilepsy*, pages 493–509. Raven Press, 1976.

[197] B.F. Westmoreland and D.W. Klass. Unusual EEG patterns. *J Clin Neurophysiol*, 7(2):209–228, 1990.

[198] E.T. Whittaker. On a new method of graduation. *Proc Edinborough Math Assoc*, 78:81–89, 1923.

[199] P. Whittle. *Prediction and Regulation by Linear Least Squares Methods*. Princeton, 1963.

[200] B. Widrow and M. Hoff. Adaptive switching circuits. *IRE Wescon Conv. Rec.*, Part 4:96–104, 1960.

[201] U. Wiklund, M. Akay, and U. Niklasson. Short-term analysis of heart-rate variability by adapted wavelet transforms. *IEEE Eng Med Biol Mag*, 16(5):113–118, September/October 1997.

[202] W.J. Williams. Biological applications and interpretations of time-frequency signal analysis. In M. Akay, editor, *Time Frequency and Wavelets in Biomedical Signal Processing*, pages 45–72. IEEE Press, 1998.

[203] Q. Xue, Y.H. Hu, and W.J. Tompkins. Neural-network-based adaptive matched filtering for QRS detection. *IEEE Trans Biomed Eng*, 39(4):317–329, April 1992.

[204] Y. Yamamoto and H. Isshiki. Instrument for controlling drowsiness using galvanic skin reflex. *Med Biol Eng Comput*, 30:562–564, September 1992.

[205] H. Yppärilä, I. Korhonen, M. Tarvainen, T. Musialowicz, S. Jacob, and J. Partanen. Discrimination of sedation levels based on event-related potentials and electroencephalogram. *J Clin Monit Comp*, In Press.

[206] H.P. Zaveri, W.J. Williams, L.D. Iasemidis, and J.C. Sackellares. Time-frequency representation of electrocorticograms in temporal lobe epilepsy. *IEEE Trans Biomed Eng*, 39(5):502–509, May 1992.

[207] J.P. Zbilut, N. Thomasson, and C.L. Webber. Recurrence quantification analysis as a tool for the nonlinear exploration of nonstationary cardiac signals. *Med Eng Phys*, 24:53–60, 2002.

[208] L. Zetterberg. Estimation of parameters for a linear difference equation with application to EEG analysis. *Math Biosci*, 5:227–275, 1969.